Variability of the ice-ocean system in the Pacific sector of the Southern Ocean

Numerical Model Studies

Dissertation
zur
Erlangung des Grades eines
Doktors der Naturwissenschaften
-Dr. rer. nat.-

Dem Fachbereich Physik/Elektrotechnik
der
Universität Bremen
vorgelegt von

Karen Aßmann

Dezember 2003

Alfred-Wegener-Institut für Polar- und Meeresforschung, Bremerhaven

1. Gutachter: Prof. Dr. Dirk Olbers
2. Gutachter: Prof. Dr. Peter Lemke

It was created in beauty. One [autumn] day the temperature drops thirty degrees in four hours, and the sea grows as motionless as a mirror. It's waiting to reflect a wonder of creation. The clouds and the sea now glide together in a curtain of heavy grey silk. The water grows viscous and tinged with pink, like a liqueur of wild berries. A blue fog of frost smoke detaches itself from the surface of the water and drifts across the mirror. Then the water solidifies. Out of the dark sea the cold now pulls up a rose garden, a white blanket of ice blossoms formed from salt and frozen drops of water.

(...)

Then frazil ice is formed, grease ice, and pancake ice, whose plates freeze together into floes. The ice separates out the salt, the seawater freezes from below. The ice breaks; packing, precipitation, and increased cold give it an undulating surface. Eventually the ice is forced adrift.

(...)

You can try and live with the ice. You can't fight it or change it or live instead of it.

Miss Smilla's Feeling For Snow
Peter Høeg

Abstract

In the framework of BRIOS (*Bremerhaven Ice Ocean Simulations*) a coupled ice-ocean model of the Southern Ocean was adapted to investigate the variability of the ice-ocean system in the Pacific sector of the Southern Ocean with a particular focus on the factors affecting dense water formation on the Ross Sea continental shelf. The model's ocean component is based on the *S-coordinate Primitive Equation Model* (SPEM) which is coupled to a dynamic-thermodynamic sea ice model. Also included is the ice-ocean interaction in major ice shelf cavities. Extensive validation with the available data base shows that the model BRIOS2.2 is able to provide a highly reasonable representation of ocean and ice conditions in the Pacific sector of the Southern Ocean.

The sea ice regimes in the western and eastern Ross Sea were shown to be decoupled from each other with sea ice characteristics in the western Ross Sea determined predominantly by the local atmospheric conditions and those in the eastern Ross Sea by ice import from the Amundsen Sea. The resulting strong gradient in sea ice formation provides the thermohaline driving force for the shelf circulation. The cooling, salt input and subsequent deep convection during the seasonal cycle modifies the waters of the shelf inflow so that their density is sufficient participate in Antarctic Bottom Water formation.

Model results show that the region around Ross Island and McMurdo Sound has a key role in controlling the exchange between the ice shelf cavity and the open ocean in the Ross Sea. Freshwater outflow from McMurdo Sound shapes the dome structure in the salinity distribution along the ice shelf edge. Drainage of High Salinity Shelf Water through McMurdo Sound into the cavity in winter prevents brine accumulation and thus lowers High Salinity Shelf Water salinities to the range observed. This also affects the balance of Ice Shelf Water and High Salinity Shelf Water, the two parent water masses for the formation of Antarctic Bottom Water in the Ross Sea.

The interannual variability of dense water characteristics is, however, predominantly controlled by variations in the shelf inflow through a sub-surface salinity and a deep temperature signal whose origin can be traced into the Amundsen and Bellingshausen Seas. The temperature anomalies are induced in the western Bellingshausen Sea where the meridional transport of Circumpolar Deep Water causes temperature anomalies at the continental shelf break.

Zusammenfassung

Im Rahmen von BRIOS (*Bremerhaven Ice Ocean Simulations*) wurde ein gekoppeltes Meereis-Ozean Modell des Südpolarmeeres modifiziert, um das Eis-Ozean-Systems im Pazifischen Sektor und die Faktoren, die die Bildung dichter Wassermassen auf dem Rossmeer-Kontinentalschelf beeinflussen, zu untersuchen. Das Modell setzt sich aus dem *S-coordinate Primitive Equation Model* (SPEM) und einem dynamisch-thermodynamischen Meereismodell zusammen. Es beinhaltet ausserdem die Eis-Ozean Wechselwirkung in den grossen Schelfeiskavernen. Gründliche Validierung mit den vorhandenen Beobachtungen zeigt, dass BRIOS2.2 eine sehr gute Darstellung der Ozean- und Eisbedingungen im Pazifischen Sektor des Südpolarmeeres liefert.

Es konnte gezeigt werden, dass die Meereisregime im westlichen und östlichen Rossmeer voneinander unabhängig sind, wobei sie im westlichen Rossmeer hauptsächlich von den lokalen atmosphärischen Bedingungen abhängen und im östlichen vom Meereisimport aus dem Amundsenmeer. Der daraus entstehende starke Gradient im Meereiswachstum stellt den themohalinen Antrieb für die Schelfzirkulation dar. Die saisonale Abkühlung, der Salzeintrag und die darauf folgende tiefe Konvektion modifizieren die Wassermassen des Schelfeinstroms derart, daß ihre Dichte ausreicht um an der Bildung von Antarktischem Bodenwasser teilzunehmen.

Modellergebnisse zeigen, dass die Region um Ross Island und McMurdo Sound eine Schlüsselrolle für den Austausch zwischen Schelfeiskaverne und offenem Ozean spielen. Ein Süßwasserausstrom durch McMurdo Sound formt die Domstruktur in der Salzgehaltsverteilung entlang der Schelfeiskante. Der Abfluss von hochsalinem Schelfwasser in die Kaverne verhindert eine starke Salzanreicherung und hält die Salzgehalte so bei den beobachteten Werten. Dieses beeinflusst auch die Balance zwischen Schelfeiswasser und hochsalinem Schelfwasser, die beide Quellwassermassen des Antarktischen Bodenwassers im Rossmeer sind.

Die zwischenjährliche Variabilität der Eigenschaften des dichten Wassers wird allerdings hauptsächlich durch Veränderungen des Schelfeinstroms bestimmt, insbesondere durch ein oberflächennahes Salzgehaltssignal und ein tiefes Temperatursignal, deren Ursprung ins Amundsen- und Bellingshausenmeer zurückverfolgt werden kann. Die Temperaturanomalien entstehen im westlichen Bellingshausenmeer, wo der meridionalen Transport von Zirkumpolarem Tiefenwasser Temperaturanomalien nahe der kontinentalen Schelfkante verursacht.

Contents

Chapter 1

Introduction

Antarctica rather disappointed the expectations humankind set in it. Far from being the fertile, densely populated, blooming *terra australis* of the Greeks it turned out to be a cold barren desert. During the early period of modern exploration the continent itself could not even be reached in most attempts because of the surrounding sea ice, so that maps of the region South of 50°S were almost devoid of land showing only the expedition tracks. Yet not so barren were the oceans surrounding Antarctica, despite being hostile to shipping and seemingly also to life. After the early explorers brought back news of the vast number of seals, exploitation drove this species almost to extinction around 1820. In the quest to find untouched populations of seals James Weddell reached the furthest south hitherto in the future Weddell Sea. Another disappointment - he did not find the seals he had come to look for. His journey marked the first real progress south since James Cook reaching 71.1°S in the Bellingshausen Sea in 1774 - quite an achievement as modern research has shown (Gurney 1997).

James Clark Ross set out to determine the location of the Magnetic South Pole on two voyages between 1839-43. While he successfully completed this task, his attempts to actually reach the Magnetic South Pole failed and only lead to extensive exploration of the Ross Sea continental shelf, discovery of the Ross Ice Shelf, reaching the furthest south possible by ship and detailed cartography of the Victoria Land coast - another Antarctic disappointment. Ross's voyages were remarkable as they constitute one of the first examples of dedicated scientific exploration of Antarctica and its surrounding ocean. Along with biological and geological observations Ross collected detailed hydrographic, meteorological and ice observations, which reflect conditions in the Ross Sea quite accurately (Ross

1847). Following Balleny's information that between 170°E and 180° existed a way through the sea ice that would lead to higher latitudes, Ross discovered that passage that was to become the explorer's and scientist's "highway" south to the Antarctic continent, also used by R.F. Scott's *Terra Nova* and R. Amundsen's *Fram* (Gurney 1997).

Early Antarctic exploration was strongly driven by the desire to claim new national territory and to harvest the economic benefits. More immaterial gains like the personal and national glory also played a major role. Scientific exploration was more a byproduct of these aims. Only in the last few decades has the importance of Antarctica, and more crucially, that of the surrounding oceans for the global climate system been realised.

Stratification of the lower- and mid-latitude oceans is highly stable with warmer, and hence lighter, surface waters overlying a large volume of colder, denser deep and bottom waters. Exchange between these regimes and replenishment of the deep and bottom waters occurs in the polar oceans where atmospheric cooling and brine release associated with sea ice formation result in the formation of cold, dense water. Sinking of these cold, dense waters down the Antarctic continental slope into the deep ocean forms one of the "engines" of the global thermohaline circulation that was described by the simplified image of a global "conveyor belt" by Gordon (1986) and Broecker (1991).

Faced with the thick multi-year ice pack of the Amundsen Sea that forced him to turn north after reaching a furthest south at 71° 10' S in 1774 James Cook understandibly, but mistakenly, concluded that there had to be a southern continent as the origin of all this ice (Gurney 1997). Today we know that ice of two types interacts with the ocean in the Antarctic marginal seas. Sea ice is formed through freezing of surface waters, while the floating ice shelves represent the interface between the meteoric ice of the Antarctic ice shield and the ocean. Both ice types play important roles in the climate system of the Southern Ocean.

The sea ice cover of the Southern Ocean is subject to a strong seasonal cycle of freezing and melting that changes the area it covers by a factor of 5 from $\sim$ 20 x 10^6 km^2 in winter to $\sim$ 4 x 10^6 km^2 in summer (e.g. Zwally et al. 2002). Sea ice strongly affects the interaction between atmosphere and ocean. Its high albedo reduces the absorption of short-wave radiation, contributing to the negative radiation balance of the high latitudes, while even a thin sea ice cover acts as an effective insulator and prevents further loss of oceanic heat to the atmosphere in winter (Semtner 1976). Melting of the ice pack in spring and

summer is accelerated by the opening of leads which reduces the total albedo and allows for quicker warming of the ocean surface. Both effects represent positive feedback mechanisms that might lead to larger changes in the context of climate change. Furthermore, a compact ice pack acts as a momentum sink for wind acting as a driving force on the ocean surface.

Sea ice formation leads to the input of salt into the upper ocean, since salt crystals are not incorporated into the ice crystal lattice. To a small extent salt is trapped in brine pockets (5 ‰ on average). Sea ice is a source of fresh water when it melts. These two processes hardly ever happen at the same site though, since strong winds can move the sea ice over distances of several hundred kilometers during a winter season. The resulting fresh-water flux represents an important factor in surface buoyancy forcing of the weakly stratified Southern Ocean.

The Antarctic Ice Sheet contains $\sim$ 90 % of the Earth's fresh water. From its central part with thicknesses reaching up to 4 km the ice sheet spreads slowly seawards under the influence of gravity. The fast flowing ice streams merge into floating ice shelves at their grounding line where the ice has thinned to hydrostatic equilibrium with the underlying ocean. These ice shelves cover 40 % of the sea surface south of the Antarctic continental shelf break. Ice shelves with thicknesses ranging from 100 - 2000 m surround much of the Antarctic continent, be it as a narrow fringe ($\sim$ 50-100 km) or filling large embayments and reaching sizes of $\sim$ 500 000 km^2 like the Ross or Filchner-Ronne ice shelves.

Accumulation of snow on the continental ice sheet and its compaction to ice forms the source term in the ice sheet's mass balance. Mass loss occurs at its edges through iceberg calving and basal melting of the floating ice shelves. The latter is thought to contribute 15 - 35% to the total mass loss (Jacobs et al. 1992). In addition to representing a significant term in the Antarctic ice sheet's mass balance, ice shelf basal melting also forms an important source of freshwater in the Antarctic marginal seas. Opposed to the other two fresh-water sources, i.e. sea ice melting and freezing and precipitation, it is not added at the ocean surface but lower in the water column where it affects water column stability.

Antarctic Bottom Water is the densest water mass in the global ocean which can be traced up to 40°N at the bottom of the Atlantic Ocean (Emery & Meincke 1986). Formation sites of Antarctic Bottom Water are located in the Weddell Sea, the Ross Sea, Prydz Bay and the Adelie Land coast. Around 15 % of the total volume of Antarctic Bottom Water originate in the Ross Sea and the Adelie Land coast, respectively, while the Weddell Sea is the main contributor

with 60 % (Orsi et al. 1999). The Ross Sea is the main source of bottom water in the Pacific Ocean, however, its northward spreading is slow since impeded by the Pacific Antarctic Ridge (Fig. 1.1) and the extreme southward course of the Antarctic Circumpolar Current (ACC) in the Pacific sector of the Southern Ocean (Whitworth et al. 1998).

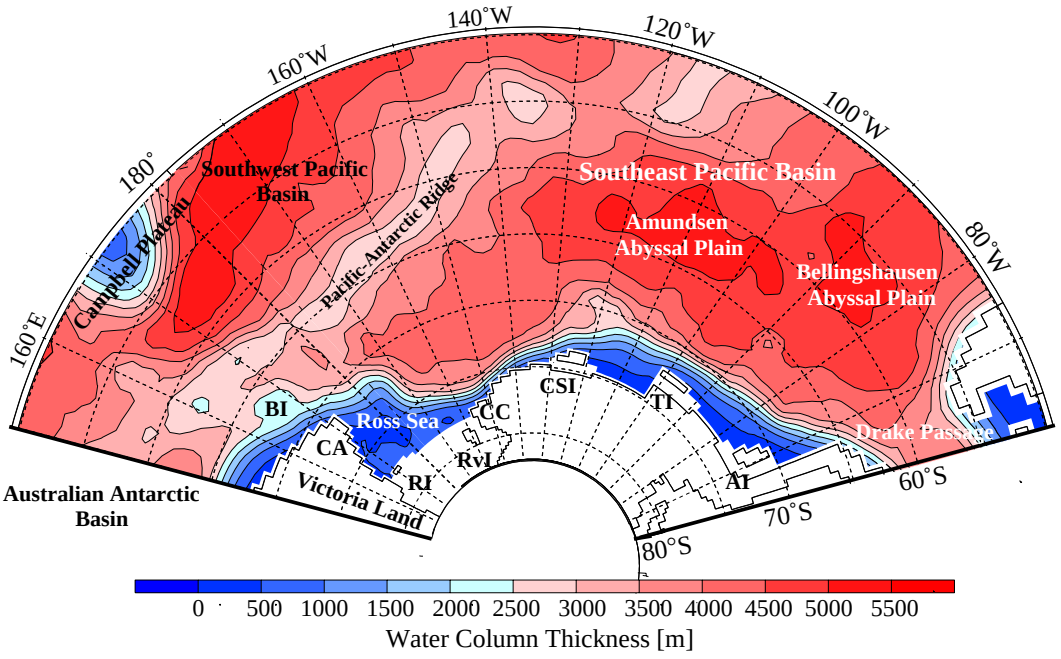

Figure 1.1: Water depth for the Southeast Pacific sector taken from Smith & Sandwell (1997) and ETOPO5 (south of 72°S). CA = Cape Adare, CC = Cape Colbeck, AI = Alexander Island, BI = Balleny Islands, CSI = Carney & Siple Islands, RI = Ross Island, RvI = Roosevelt Island, TI = Thurston Island.

Winter sea surface processes play an important role in the formation of cold, saline shelf waters which evolve into Antarctic Bottom Water after mixing with modified forms of Circumpolar Deep Water during their descent down the continental slope (Foster & Carmack 1976). Vigorous sea ice formation occurs in so-called polynyas, areas which are kept ice free by consistently strong offshore winds descending from the continental plateau. The associated brine release leads to instability of the weakly stratified water column and hence to deep convection and vertical mixing. On the shallow continental shelf this process results in a significant salt accumulation and deep reaching cooling of the water column and consequently to shelf waters dense enough to descend into the deep ocean even after mixing with Circumpolar Deep Water. Accumulation of dense waters occurs

on the wide continental shelf areas of the Weddell (Foster & Carmack 1976) and Ross seas (Jacobs et al. 1970) and in a depression on the Adelie Land continental shelf within the Mertz Glacier polynya (Rintoul 1998).

A second process that leads to the formation of Antarctic Bottom Water is the mixing of modified Circumpolar Deep Water with Ice Shelf Water which leaves the large ice shelf cavities with potential temperatures below the surface freezing point. This so-called *in situ* supercooled state can be attained through interaction of shelf water masses with the ice shelf base, since the freezing point of sea water is a function of its salinity and the *in situ* pressure. In the Weddell Sea this process has been observed in the Filchner Trough by Foldvik et al. (1985), while Jacobs et al. (1985) describe a similar mechanism for the Ice Shelf Water core leaving the central Ross ice shelf cavity.

Other than the Weddell Sea the Ross Sea continental shelf is generally ice-free during the summer months (Gloersen et al. 1992). This makes it a useful and convenient site to observe the shelf processes, or at least their summer remnant, that result in the formation of waters that have the right characteristics to participate in bottom water formation. Persistent, strong southerly winds descending from the Transantarctic Mountains of Victoria Land drive sea ice northward in the western Ross Sea (Jacobs & Comiso 1989). During autumn and winter this results in vigorous brine release and allows for the formation of High Salinity Shelf Water (HSSW), the densest water mass found anywhere on the Antarctic continental shelf. In spring the continuing northward drift results in the opening of the Ross Sea polynya as increased short-wave radiation reverses the direction of the surface heat flux (Zwally et al. 1985). The southern part of the Ross Sea is covered by the Ross Ice Shelf, which is similar in size to the Filchner-Ronne Ice Shelf (FRIS) in the Weddell Sea with 500,000 km^2 (Fox & Cooper 1994). Ross Ice Shelf thickness only reaches up to $\sim$ 700 m, however, and the Ice Shelf Water that exits the cavity in the central Ross Sea does not reach temperatures as low as those of the plume leaving the FRIS cavity in the Filchner Trough (Jacobs et al. 1985). While the Ross Sea continental shelf counts among the most densely sampled regions around Antarctica, very few data are available representing conditions in winter and underneath the Ross Ice Shelf, i.e. at the times and locations during which water mass formation takes place that results in products which have the potential to form Antarctic Bottom Water.

Similar to the Weddell Sea the basin north of the Ross Sea continental shelf is occupied by a large cyclonic gyre. In contrast to the Weddell Gyre its transport

and structure are largely unknown except for a few estimates (e.g. Locarnini 1994, Gouretski 1999). Since, however, its southern branch, which follows the coastal easterly winds, forms the main inflow to the Ross Sea continental shelf, detailed knowledge of ocean circulation and properties of the upstream region, i.e. the Amundsen and Bellingshausen Seas, would be desirable.

Analogously to the ocean circulation, sea ice from the Amundsen Sea is transported westward into the eastern Ross Sea (Jacobs & Comiso 1989, Drinkwater et al. 1999), thus possibly affecting sea ice and dense water formation on the continental shelf. However, as James Cook found out himself, the sea ice cover of the Amundsen and Bellingshausen Seas has long been considered impenetrable (Heap 1964), preventing early and severely limiting modern ship-based observation of the continental shelf of the southeastern Pacific Ocean. For the Southern Ocean, the hydrographic conditions in the Amundsen and Bellingshausen Seas are unique. The ACC approaches the continental shelf much more closely than in the Weddell Sea. Orsi et al. (1995) place the southern boundary of the ACC north of 60°S in the Weddell Sea, while in the Amundsen and Bellingshausen Seas it practically touches the continental shelf with a location around 70°S. As a result almost unmodified Circumpolar Deep Water penetrates as far south as the fronts of major glaciers draining the West Antarctic Ice Sheet (Hellmer et al. 1998). As the river run-off on the Arctic continental shelf, the resulting fresh-water flux stabilizes the water column preventing deep convection, the accumulation of dense shelf waters, and deep and bottom water formation (Baines & Condie 1998) and allowing the aforementioned perennial sea ice cover to exist. Oceanic forcing has been implied as one of the driving mechanisms in a well-documented recent and rapid retreat of the ice shelf cover of West Antarctica (Vaughan & Doake 1996, Rignot 1998), placing great importance on an improved understanding of the ocean circulation in this region.

Lately, the focus of research has started to shift towards investigating the variability of the Antarctic ice-ocean system as longer time series of observations have become available. Satellite data has made the identification of oscillatory patterns and trends in the atmosphere, sea ice, and ocean surface possible. White and Peterson (1996) linked anomalies in surface pressure, meridional wind strength, sea ice extent, and sea surface temperature in their description of the Antarctic Circumpolar Wave (ACW). Further investigations have refined the description of this phenomenon describing a frequency and wave number modulation over time (Connolley 2003, Venegas 2003). Other work linked its origin to lower latitude

phenomena like the El Niño-Southern Oscillation (ENSO) (e.g. Cai & Baines 2001), with the Amundsen, Bellingshausen and Ross Seas being identified as regions where the lower-latitude signal enters the Southern Ocean (Ledley & Huang 1997, Yuan & Martinson 2000).

Since observations of the deep ocean require an amount of logistical effort that prevents closely spaced continuous monitoring, work on the interannual variability of subsurface processes is sparse. With observations mostly confined to the summer season, very little is even known about changes occurring during the seasonal cycle. Work usually aims at the identification of long-term trends rather than oscillatory behaviour like the ACW/ENSO related work. For the Weddell Sea Schröder et al. (2002) and Robertson et al. (2002) studied the variability of outflow characteristics into the Scotia Sea identifying a possible warming trend. Comiso & Gordon (1998) tried to link sea ice and bottom water variability in the Weddell Sea, but could not establish a connection conclusively due to the limitations of the hydrographic data set. Jacobs & Giulivi (1998) and Jacobs et al. (2002) made use of the, for Southern Ocean hydrographic standards, extensive data set that spans almost 40 years to investigate interannual variability of the ice-ocean system of the Ross Sea continental shelf and discovered a freshening of the shelf waters.

Numerical models hence form an essential part of research into the interannual variability of the Antarctic ice-ocean system. Previous modelling efforts of the Ross Sea concentrated either on the cavity (e.g., Hellmer & Jacobs 1995, Holland et al. 2003) or on reproducing the regional shelf circulation over short time periods (e.g., Commodari & Pierini 1999, Bergamasco et al. 1999, Dinniman et al. 2003). None include both the sea ice-ocean and the ice shelf-ocean interaction. Modelling work that deals with the circulation and water masses of the South East Pacific Basin is as sparse as the observational cover and confined to inverse modelling approaches (Grotov et al. 1998) or the analysis of the Southern Ocean in global ocean models with relatively coarse resolution (e.g. Fichefet & Goosse 1999). Model studies of the entire Southern Ocean tend to focus either on the ACC and its dynamics (e.g. Olbers & Wübber 1991, Rintoul et al. 2001), on the large scale sea ice distribution (e.g. Häkkinen 1995, Goose & Fichefet 1999, Marsland & Wolff 2001) or on the Weddell Sea (Beckmann et al. 1999, Timmermann et al. 2002 b).

The model used in this study was developed in the framework of the BRIOS (Bremerhaven Ice Ocean Simulations) project. It was designed as a coupled

ice-ocean model that includes the ice shelf-ocean interaction. Thus, it removes the need to force a cavity model with external, and therefore likely inconsistent, fluxes across its northern boundary. Interannual and seasonal variability of the surface fluxes is imposed through use of daily varying reanalysis products as atmospheric forcing data. The model domain that covers an area from almost the southern end of the large ice shelf cavities to well north of the maximum sea ice extent and the northern boundary of the cyclonic gyres allows research into exchange processes between the continental shelf and the deep ocean domain. The model resolution is intermediate to that of most global and more regional models and, since enhanced in the continental shelf regions, sufficient to represent the processes on the continental shelf.

The work presented in this thesis places particular emphasis on processes on the Ross Sea continental shelf and their variability on seasonal to interannual time scales. Supplementing the model results with observations allows for careful validation of the model, but also solves questions left unanswered by the observations, like the exchange processes between the sea ice and ocean regimes of different marginal seas and their interannual variability. Since dense shelf waters are an important ingredient of the bottom water formation, particular attention will be paid to the factors crucial to their formation and to the causes of interannual variability in their characteristics.

Chapter 2 introduces the components of the model BRIOS2.2. It contains detailed descriptions of ocean and sea-ice model components, of their coupling mechanism, and of the ice shelf-ocean interaction. The last part of the chapter provides an introduction to the model domain and grid, forcing data sets and the initial and boundary conditions used in this study.

An introduction to sea ice conditions in the Ross, Amundsen and Bellingshausen Seas is given in Chapter 3. This will serve as background for the investigation of ocean properties, since these are intimately linked to the sea ice regimes in the various marginal seas. Model results are compared to observations wherever possible and validated quantitatively.

Chapter 4 starts with a description of water mass characteristics and circulation in the Pacific sector of the Southern Ocean with a particular focus on the Ross Sea continental shelf. A review of the existing literature is complimented with model results and their validation against observations. This is followed by a detailed analysis of the effect of the seasonal cycle on the Ross Sea continental shelf on water mass distribution, circulation, and ice shelf basal mass flux. A

fresh-water budget for the Ross Sea continental shelf is drawn up. Finally, the effect of McMurdo Sound topography on water mass exchange across the Ross Ice Shelf front is investigated with a focus on dense water drainage into the cavity and the outflow of modified water masses from it.

Chapter 5 deals with sea ice variability in the Pacific sector of the Southern Ocean. A comparison of model results to drift observations from the first sea ice drift buoys deployed in the Amundsen Sea allows conclusions to be drawn about the driving forces of sea ice, its main regimes, and short-term drift variability as well as providing another point of model validation. An analysis of sea ice transports between the different marginal seas of the Pacific sector sets the scene for investigations into the interannual and larger scale variability of the sea ice system. Areas of focus include the recent sea ice retreat in the Bellingshausen Sea and its causes, a sea ice budget for the Amundsen Sea and finally the possible impact of sea ice transported from the Amundsen Sea onto the Ross Sea continental shelf.

In Chapter 6 a study of the interannual variability of dense water volume and properties on the Ross Sea continental shelf is presented. Sensitivity studies identify the atmospheric influence and the importance of both local and external sources. The influence of atmospheric forcing on the interannual variability of the local fresh water fluxes is analysed. The inflow variability to the Ross Sea continental shelf is evaluated as an external source for the interannual variability of shelf water characteristics. The chapter closes with an investigation of the processes in the Amundsen and Bellingshausen Seas that determine the inflow characteristics.

Chapter 7 summarizes the results obtained in this study and gives an outlook onto scope for future work.

Chapter 2

Model description

The coupled sea ice-ice shelf-ocean model BRIOS2.2 employed here has been developed and successfully applied to the Southern Ocean in the framework of the BRIOS (Bremerhaven Regional Ice Ocean Simulations) group (Timmermann et al. 2002 a, b, Assmann et al. 2003). It consists of a hydrostatic ocean circulation model and a dynamic-thermodynamic sea ice model the thermodynamic part of which is also used to describe the ocean interaction with the ice shelf base.

2.1 Ocean model

2.1.1 Model basics

The ocean component is based on the S-coordinate Primitive Equation Model SPEM (Haidvogel et al. 1991). Circulation models with a vertical coordinate system that follows the bottom topography, so-called S- or σ-coordinates, have been shown to be well-suited to describe the ocean properties in regions which encompass deep ocean basins and shallow continental shelves as well as possessing a relatively weak stratification (Haidvogel & Beckmann 1999).

The state of the ocean is described by four prognostic model variables - the horizontal components of velocity u and v, potential temperature Θ, and salinity S - and three diagnostic ones - the local *in situ* density ρ, pressure p and vertical velocity w. To compute their temporal and spatial evolution a system of an equal number of equations is used.

It consists of the equations of motion, deduced from the principle of conservation of momentum,

$$\frac{\partial u}{\partial t} + \vec{u} \cdot \nabla u - fv = -\frac{\partial \Phi}{\partial x} + F^u + D^u \quad (2.1)$$

$$\frac{\partial v}{\partial t} + \vec{u} \cdot \nabla v + fu = -\frac{\partial \Phi}{\partial y} + F^v + D^v \quad (2.2)$$

$$0 = -\frac{\partial \Phi}{\partial z} - \frac{\rho g}{\rho_0} \quad (2.3)$$

the equation of continuity, ensuring conservation of mass,

$$\frac{\partial u}{\partial x} + \frac{\partial v}{\partial y} + \frac{\partial w}{\partial z} = 0, \quad (2.4)$$

the balance equations for potential temperature and salinity

$$\frac{\partial \Theta}{\partial t} + \vec{u} \cdot \nabla \Theta = F^\Theta + D^\Theta \quad (2.5)$$

$$\frac{\partial S}{\partial t} + \vec{u} \cdot \nabla S = F^S + D^S, \quad (2.6)$$

and the non-linear equation of state as introduced by UNESCO (1981) and modified by Jackett & McDougall (1995) -

$$\rho = \rho(\Theta, S, z). \quad (2.7)$$

Variables and constants are defined as follows:

f	Coriolis parameter $f = 4\pi/86400 \cdot \sin\phi$ where ϕ is the geographical latitude,
g	acceleration due to gravity,
ρ_0	mean density of (sea)water, ρ_0= 1000 kg m^{-3},
Φ	dynamical pressure, $\Phi = p/\rho_0$,
D^χ	divergence of turbulent fluxes, where χ can stand for any of Θ, S, u or v,
F^χ	forcing terms, where χ can stand for any of Θ, S, u or v.

The following approximations were made to bring the equations into their so called primitive form shown above:
Spherical approximation: It is assumed that geopotential surfaces are spherical and that gravity only applies to the vertical, the z-component, $\vec{g} = (0, 0, g)$.
Traditional approximation: The vertical velocity component is generally much

smaller than the horizontal ones ($W/U = 10^{-3}$). Therefore the vertical component of the Coriolis force can be neglected in comparison to gravity.

Hydrostatic approximation: Since the vertical velocity component is assumed to be small, the vertical momentum balance reduces to the hydrostatic equation (2.3). The vertical velocity component w is diagnosed from the equation of continuity (2.4).

Boussinesq approximation: It is assumed that the fluid density, ρ, does not depart much from a mean value, ρ_0. Hence we can write ρ as $\rho = \rho_0 + \rho'$ whereby the perturbation ρ', caused by stratification and/or fluid motion, is much smaller than the reference density. It is therefore possible to reduce the continuity equation to the form (2.4), representing conservation of volume rather than of mass.

The time-dependent surface forcing terms F^u, F^v, F^θ and F^S are calculated from the coupled sea ice model and are described in more detail in Section 2.3. As time-independent boundary conditions of Equations (2.1) - (2.7) serves the requirement of no flux into the ocean floor or the coast lines which is accomplished by setting the gradients of Θ and S perpendicular to the boundaries to zero. Further, to eliminate fast-travelling gravity waves and to be able to use a larger time step, the so-called *rigid lid* approximation, i.e. $w = 0$ at the surface, is used. Since the current integrated over the entire water column, (U, V), is hence free of horizontal divergence, it can be described by a prognostic stream function Ψ with

$$U = -\frac{\partial \Psi}{\partial y}, \qquad V = \frac{\partial \Psi}{\partial x}. \tag{2.8}$$

The temporal evolution of Ψ can be computed using a vorticity equation in the form of an elliptical differential equation which is solved with the help of a multi-grid solver (Adams 1989) and the capacitance matrix method (Wilkin et al. 1995).

2.1.2 Parametrization of subscale processes

Both the lateral and vertical components of the viscous and diffusive terms D^χ in the equations of motion and conservation of heat and salt are calculated by using a harmonical mixing approach

$$D^\chi = \nabla(\nu^\chi \nabla \chi) \tag{2.9}$$

where χ can represent any of the prognostic variables u, v, Θ and S.

Lateral mixing

Since the size of the model grid boxes varies considerably throughout the model domain, the horizontal exchange coefficients vary depending on the spatial resolution. The viscosity is defined as

$$\nu^{u,v} = 5 \cdot 10^{-6} s^{-1} \Delta_{\vec{x}}^2 \tag{2.10}$$

where $\Delta_{\vec{x}}$ represents the horizontal size of the grid box in metres. The diffusivity $\nu^{\Theta,S}$ is parametrized as a function of the Reynolds-number $Re = \frac{UL}{\nu^{\vec{u}}}$. It hence depends linearly on the resolution and the local velocity. Lateral mixing occurs along geopotential surfaces to prevent implicit vertical diffusion along the σ-surfaces (Beckmann & Haidvogel 1997). In the ocean surface layer not covered by ice shelves and in the bottom layer a background diffusivity of

$$\nu_{bg}^{\Theta,S} = 2 \cdot 10^{-2} m s^{-1} \Delta_{\vec{x}} \tag{2.11}$$

is added in order to represent the effect of mixing due to wind and turbulent mixing in the bottom boundary layer.

Vertical mixing

Because of the weak stratification of the Southern Ocean, treatment of the vertical mixing processes is of crucial importance. Brine release during sea ice formation leads to static instability and deep convection. Timmermann et al. (2002a) identified a modified version of the approach by Pacanowski and Philander (1981) as a suitable parametrization of this sub-grid scale process. In this scheme, vertical viscosity and diffusivity are calculated according to

$$\nu^{u,v} = \frac{\nu_0}{(1 + \alpha Ri)^n} + \nu_b^{u,v} \tag{2.12}$$

$$\nu^{\Theta,S} = \frac{\nu^{u,v}}{1 + \alpha Ri} + \nu_b^{\Theta,S} \tag{2.13}$$

where

$$\nu_0 = 0.01 \text{ m}^2 \text{ s}^{-1} \text{ ; } \nu_b^{u,v} = 10^{-4} \text{ m}^2 \text{ s}^{-1} \text{ ; } \nu_b^{\Theta,S} = 10^{-5} \text{ m}^2 \text{ s}^{-1} \text{ ;}$$
$$n = 2 \text{ ; } \alpha = 5$$

as a function of the Richardson number:

$$Ri = \frac{N^2}{(\frac{\partial u}{\partial z})^2 + (\frac{\partial v}{\partial z})^2} \tag{2.14}$$

They hence depend on the vertical shear and the stability of the water column which is described by the Brunt-Väisälä frequency.

$$N^2 = -\frac{g}{\rho_0}\frac{\partial \rho}{\partial z} \tag{2.15}$$

For stable stratification and weak vertical shear, i.e., for large Richardson numbers, both vertical viscosity and diffusivity are determined by the values of $\nu_b^{u,v}$ and $\nu_b^{\Theta,S}$. Therefore, to ensure the vertical momentum transport typical for the Ekman layer, vertical viscosity and diffusivity are given a lower limit of $\nu_{min}^{u,v,\Theta,S} = 10^{-3}$ m^2 s^{-1} in the top three model layers.
Similarly, an upper limit of $\nu_{max}^{u,v,\Theta,S} = 10^{-2}$ m^2 s^{-1} is imposed on viscosity and diffusivity preventing the destruction of a realistic water mass structure in the presence of large vertical exchange coefficients. The latter applies when the Richardson number becomes very small or even negative during weakly stable or unstable stratification and large vertical shear. The upper limit may seem small considering that exchange coefficients of 1 m^2 s^{-1} have been observed in convection cells (Schott & Leaman 1991, Send & Käse 1998). However, these cells only have diameters of the order of 1km and are hence much smaller than a model grid box. The maximum value chosen reflects the presence of a number of convection cells within a grid box together with less active areas.

Bottom friction

Friction at the ocean floor is parameterized by the linear relationship

$$\tau_b^{(u,v)} = \rho_0 \cdot r^b \cdot (u,v)_b \tag{2.16}$$

where $(u,v)_b$ is the horizontal velocity in the model bottom layer and $r^b = 5 \cdot 10^{-4}$ m s^{-1}.

2.2 Sea ice model

The sea ice component is based on a dynamic-thermodynamic sea ice model with a viscous-plastic rheology (Hibler 1979). The Parkinson & Washington (1979) thermodynamics are employed using the Semtner (1976) zero-layer approach for heat conduction. The inclusion of a prognostic snow layer (Owens & Lemke 1990) accounts for the effect of flooding (Leppäranta 1983; Fischer 1995).
To describe the temporal evolution of the ice pack the model uses five prognostic variables:

h, defined as the mean sea ice thickness over the entire grid box representing the ice volume per grid box area. To obtain the actual sea ice thickness in the ice covered part of the grid box, h has to be divided by the sea ice concentration A.

h_s, the mean snow thickness, is defined analogously.

A, the dimensionless sea ice concentration, as the fraction of a grid box covered by sea ice.

$\vec{u}_i = (u_i, v_i)$, the drift velocity, quantifying the motion of the ice pack which is described as a two-dimensional continuum. While it of course consists of separate ice floes, this assumption is permissible at the scales relevant to this work.

The ice drift velocity is calculated from a momentum balance according to Hibler (1979) which is described in more detail in Section 2.2.2. However, sea ice advection is described by the modified upstream-scheme of Smolarkiewicz (1983) making the use of explicit diffusion redundant. The temporal evolution of the other three prognostic variables is described by the following balance equations

$$\frac{\partial h}{\partial t} + \nabla \cdot (\vec{u}_i h) = S_h \tag{2.17}$$

$$\frac{\partial h_s}{\partial t} + \nabla \cdot (\vec{u}_i h_s) = S_s \tag{2.18}$$

$$\frac{\partial A}{\partial t} + \nabla \cdot (\vec{u}_i A) = S_A \tag{2.19}$$

where the first term on the left-hand side describes the local, temporal change, the second the effect of advection and the source terms on the right-hand side the thermodynamic changes detailed in the next section.

2.2.1 Thermodynamics

Energy balance

Following Parkinson & Washington (1979) the energy balance of sea ice and snow layer is described by

$$Q_{ai} + Q_{oi} + \rho_i L_i \left(\frac{\partial h}{\partial t} + \frac{\rho_{sn}}{\rho_i} \cdot \frac{\partial h_s}{\partial t} \right) = 0 \tag{2.20}$$

neglecting heat storage within the sea ice. Q_{ai} and Q_{oi} denote the heat fluxes between sea ice, and atmosphere and ocean, respectively, $\rho_i = 910$ kg m^{-3} and $\rho_{sn} = 290$ kg m^{-3} the densities of ice and snow and $L_i = 3.34 \cdot 10^5$ J kg^{-1} the latent heat of fusion. Q_{ai} and Q_{oi}, positive for heat fluxes into the ice, are the sum of the short- and longwave radiation fluxes Q_{SW} and Q_{LW}, and latent and sensible heat fluxes Q_l and Q_s

$$Q_{ai,ao} = Q_{SW}^{\downarrow} + Q_{SW}^{\uparrow} + Q_{LW}^{\downarrow} + Q_{LW}^{\uparrow} + Q_s + Q_l \tag{2.21}$$

whereby arrows $\downarrow$ and $\uparrow$ denote downward and upward fluxes. Incoming short wave solar radiation $Q_{SW}^{\downarrow}$ is computed using the empirical formula by Zillman (1972) with a correction for cloud cover by Laevastu (1960). Outgoing short wave radiation is described by

$$Q_{SW}^{\uparrow} = \alpha \, Q_{SW}^{\downarrow}, \tag{2.22}$$

whereby albedoes α for each surface type are defined according to Fischer (1995). Longwave radiation fluxes Q_{LW} are calculated using

$$Q_{LW}^{\downarrow} = \epsilon_a \, \sigma \, T_a^4 \tag{2.23}$$

$$Q_{LW}^{\uparrow} = \epsilon_s \, \sigma \, T_s^4 \tag{2.24}$$

where T_a is the 2-m air temperature, T_s the surface temperature of sea ice or ocean and $\sigma = 5.67 \cdot 10^{-8}$ W m^{-2} K^{-4} the Stefan-Boltzmann constant. The atmosphere's emissivity in the infrared band ϵ_a is defined as a function of cloud cover (König-Langlo & Augstein, 1994), and that of sea ice and water set constant to $\epsilon_s = 0.97$.

The turbulent fluxes of sensible and latent heat, Q_s and Q_l, are calculated analogously from

$$Q_s = \rho_a \, c_p \, C_s \, |\vec{u_{10}}| \, (T_a - T_s) \tag{2.25}$$

$$Q_l = \rho_a \, L \, C_l \, |\vec{u_{10}}| \, (q_a - q_s), \tag{2.26}$$

where $\rho_a = 1.3$ kg m^{-3} is the surface density of air, $c_p = 1004$ J kg^{-1} K^{-1} its specific heat capacity, and $L = 2.5 \cdot 10^6$ J kg^{-1} and $2.834 \cdot 10^6$ J kg^{-1} the latent heat of vapourisation and fusion of water, respectively. The heat transfer coefficients for sensible and latent heat, C_s and C_l, were chosen as $1.75 \cdot 10^{-3}$ (Maykut 1977, Parkinson & Washington 1979). The 10-m wind velocity $\vec{u}_{10}$, the 2-m temperature T_a, and specific humidity q_a of air are taken from the forcing data as time-dependent boundary conditions.

Following Semtner (1976) the boundary conditions of the sea ice energy balance are

$$Q_{ai} + Q_c + \rho_i L_i \left(\frac{\partial h}{\partial t}\right)_a = 0 \tag{2.27}$$

at the atmosphere-sea ice interface and

$$Q_{oi} - Q_c + \rho_i L_i \left(\frac{\partial h}{\partial t}\right)_o = 0 \tag{2.28}$$

at the sea ice-ocean boundary. The conductive heat flux Q_c is calculated from the upper and lower interface boundary conditions of the sea ice energy balance using the so-called zero layer model (Semtner 1976). This approach assumes that the ice does not possess a heat capacity, and that hence the conductive heat flux is constant vertically throughout the ice. Therefore, Q_c has the same magnitude at the upper and lower boundaries, but is used with opposite sign. This leads to a linear temperature profile with different gradients for ice and snow due to the different heat conductivities, κ_i and κ_s, respectively. The conductive heat flux can be expressed as

$$Q_c = \frac{\kappa_i (T_b - T_s)}{h_i^*}, \tag{2.29}$$

whereby

$$h_i^* = h_i + h_{sn} \frac{\kappa_i}{\kappa_s} \tag{2.30}$$

with heat conductivities

$$\begin{aligned} \kappa_i &= 2.17\,\mathrm{W\ m^{-1}\ K^{-1}} \\ \kappa_s &= 0.31\,\mathrm{W\ m^{-1}\ K^{-1}} \end{aligned}$$

includes the insulation due to the snow layer as the effective thermodynamic ice thickness. $h_i = h/A$ and $h_{sn} = h_s/A$ denote the actual ice and snow thicknesses in the ice covered part of the grid box, T_b is the temperature at the sea ice base, here set to the freezing temperature T_f as defined in section (2.3.1), and T_s the surface temperature, calculated diagnostically as described below.

The heat flux Q_{oi} at the sea ice-ocean interface is computed from the thermodynamic interaction between sea ice and ocean described in section (2.3.1).

Sea ice growth and lead formation

The thermodynamic sea ice growth rate is calculated as an area weighted mean over the sea ice covered and open water part of the grid cell.

$$S_h = A \cdot \left(\frac{\partial h}{\partial t}\right)_a + A \cdot \left(\frac{\partial h}{\partial t}\right)_o + (1 - A) \cdot \left(\frac{\partial h}{\partial t}\right)_{ow} \tag{2.31}$$

whereby right-hand terms represent the growth rate at the atmosphere-ice interface (only melt and occasionally snow-ice conversion), at the sea ice base, and in the open water part of the grid cell, respectively.
The growth rates of ice and snow at the sea ice surface are described by

$$\frac{\partial h_s}{\partial t} = -\frac{Q_{ai} + Q_c}{\rho_{sn} L_i} \tag{2.32}$$

$$\left(\frac{\partial h}{\partial t}\right)_a = -\frac{Q_{ai} + Q_c}{\rho_i L_i} - \frac{\partial h_s}{\partial t} \tag{2.33}$$

whereby it is assumed that the entire snow layer has to melt before a change in sea ice thickness occurs due to an atmospheric heat flux. The conductive heat flux Q_c and the surface temperature T_s are calculated by iteration from equations (2.27), (2.21), and (2.29) with the conditions that T_s cannot exceed 0°C, i.e., the freezing point temperature of fresh water, and that the sea ice surface only melts, but does not produce additional ice. To account for the presence of ice floes of different thickness in each model grid box a separation of sea ice thickness into seven thickness classes between 0 and $2h_i^*$ is assumed, computing the growth rate for each of them separately and averaging in the end (Hibler 1984).
Analogously to Equation(2.33) the sea ice growth rate at the base follows from the balance of the heat fluxes at the sea ice-ocean interface.

$$\left(\frac{\partial h}{\partial t}\right)_o = -\frac{Q_{oi} - Q_c}{\rho_i L_i} \tag{2.34}$$

Once the ocean surface temperature - in the model the temperature of the top horizontal layer is used - reaches the freezing point temperature T_f, equilibration of the energy balance is achieved through gain of latent heat from sea ice production. This leads to a thermodynamic growth rate of

$$\left(\frac{\partial h}{\partial t}\right)_{ow} = -\frac{Q_{ao}}{\rho_i L_i}. \tag{2.35}$$

in the ice-free part of the grid box.
The change in sea ice concentration A associated with thermodynamic sea ice growth is calculated using the following empirical relationships (Hibler 1979). During freezing the growth rate of sea ice covered area S_A is proportional to the percentage of open water $(1 - A)$

$$S_A = \frac{1 - A}{h_o} \left(\frac{\partial h}{\partial t} \right)_{ow,\, freeze} + S_A^{sh}, \tag{2.36}$$

whereby h_0, the so-called lead closing parameter, which determines the rate at which the sea ice cover closes, is chosen to be $h_0 = 1.0$ m (Timmermann 2000). This ensures a realistic representation of sea ice volume and water mass properties. S_A^{sh} is the area of leads formed by shear deformation. During melting the sea ice covered area decreases proportionally to the decrease in sea ice volume

$$S_A = \frac{A}{2h} \left(\frac{\partial h}{\partial t} \right)_{melt} + S_A^{sh}, \tag{2.37}$$

whereby the factor $\frac{A}{2h}$ arises from the assumption of an even distribution of sea ice thickness between 0 and $\frac{2h}{A}$. The formation of leads through shear forces is parameterized by

$$S_A^{sh} = -0.5 \left(\Delta - |\nabla \cdot \vec{u}_i| \right) \mathrm{e}^{-C(1-A)} \tag{2.38}$$

where Δ is a measure of the rate of deformation and C is defined as in section 2.2.2.

2.2.2 Momentum balance

Sea ice and snow are advected with drift velocity $\vec{u}_i$, which is calculated using the momentum balance equation

$$m \left\{ \frac{\partial \vec{u}_i}{\partial t} + \vec{u}_i \cdot \nabla \vec{u}_i \right\} = \vec{\tau}_{ai} - \vec{\tau}_{io} - mf\vec{k} \times \vec{u}_i - mg\nabla\eta + \vec{F} \tag{2.39}$$

as introduced by Hibler (1979). It describes the local temporal change and the effect of advection on the left-hand side, as well as on the right-hand side the surface stresses due to wind

$$\vec{\tau}_{ai} = \rho_a c_{d,ai} \left| \vec{u}_{10} \right| \vec{u}_{10}, \tag{2.40}$$

with the atmospheric stress coefficient $c_{d,ai} = 1.32 \cdot 10^{-3}$, and due to ocean currents $\vec{\tau}_{io}$ as described in section 2.3.2, the Coriolis force, the force due to gravity on the

tilted ocean surface and the internal forces $\vec{F}$. The variable $m = \rho_i h$ denotes the ice mass per unit area, $\vec{k} = (0, 0, 1)$ the unit vector perpendicular to the surface and η the sea surface elevation above a constant geopotential, the geoid, which is deduced from the barotropic stream function as part of the sea ice-ocean coupling scheme.
The formulation of the internal forces (Hibler 1979) describes the sea ice as a viscous-plastic medium. At small rates of deformation the sea ice will behave as a viscous compressible fluid, while as the rate of deformation increases the sea ice will deform plastically, i.e., will break beyond a critical value.
Observations have shown that there are no significant internal forces for divergent drift, while sea ice strongly resists shear and convergence (Arctic Ice Dynamics Joint Experiments AIDJEX). Hibler (1979) describes the maximum internal stress as a function of the mean sea ice thickness h and concentration A:

$$P = P^* h \, \mathrm{e}^{-C(1-A)}. \tag{2.41}$$

Since the large-scale forces are a statistical mean of numerous subgrid scale processes, the parameters P^*, C, e and Δ_{min} relevant to the description of the rheology and internal forces are purely model parameters whose values were chosen as

$$\begin{aligned} P^* &= 20000\mathrm{N\ m}^{-2} \\ C &= 20 \\ e &= 2 \\ \Delta_{min} &= 2 \cdot 10^{-9} s^{-1} \end{aligned}$$

(Hibler 1979; Fischer 1995; Harder 1996; Timmermann 2000). The viscous-plastic sea ice model has been determined from a hierarchy of models to be the optimal description of sea ice in climate models (Lemke et al. 1997, Kreyscher et al. 2000).

2.2.3 Snow

The source term S_s in the balance equation (2.18) includes the following contributions to the temporal evolution of the snow layer (Owens & Lemke 1990): Precipitation at air temperatures $T_a < 0°$ C accumulates as snow in the ice covered part of the grid cell. At $T_a > 0°$ C it is assumed that the snow cover will

melt entirely before melting of the sea ice surface starts. Since snow ice formation due to flooding produces a significant part of the ice volume (Eicken et al. 1994), this effect is parameterized following Leppäranta (1983). When enough snow accumulates on the sea ice to submerge the snow-ice interface, calculated by using Archimede's principle, and water enters the normally porous snow layer, this part of the snow is converted to meteoric ice.
Thus, the thermodynamic part of the sea ice model takes into account the damping effect of snow on thermodynamic sea ice growth due to its low heat conductance and on melting of the sea ice surface due to its high albedo.

2.3 Sea ice-ocean coupling

The coupling mechanism between ocean and sea ice model is used as developed by Timmermann et al. (2002a).

2.3.1 Heat flux

The heat flux between ocean and sea ice base is parametrized as

$$Q_{oi} = \rho_w c_{p,w} c_{h,io} u_* (T_o - T_f) \tag{2.42}$$

according to Morison et al. (1987). ρ_w and $c_{p,w}$ denote seawater density and specific heat capacity at constant pressure, respectively and the transfer coefficient is $c_{h,io} = 1.2 \times 10^{-2}$. The relative velocity between sea ice and ocean is used to calculate the friction velocity u_*:

$$u_* = \sqrt{c_{d,io}} \mid \vec{u}_w - \vec{u}_i \mid \tag{2.43}$$

where $\vec{u}_w$ and $\vec{u}_i$ are the velocities of the uppermost ocean layer and the sea ice, respectively, and $c_{d,io} = 3 \times 10^{-3}$ is the oceanic drag coefficient. T_o is the temperature in the uppermost ocean model grid box, and a nonlinear equation (UNESCO 1978) is used to calculate the ocean surface freezing temperature T_f as a function of salinity and pressure.
The surface heat flux in the open water part of each grid cell Q_{ow} is calculated using the balance of Parkinson and Washington (1979). Once the ocean reaches its surface freezing temperature, additional heat loss results in sea ice formation.

The total ocean surface heat flux Q_o is calculated as an area weighted mean of the contributions described above.

$$Q_o = (1 - A)Q_{ow} - AQ_{oi} \tag{2.44}$$

2.3.2 Salt flux

The total salinity flux $\mathcal{F}^S$ is described as the sum of the fluxes originating from melting and freezing of ice and snow, $\mathcal{F}_i^S$, and from the difference between precipitation $\mathcal{P}$ and evaporation $\mathcal{E}$, $\mathcal{F}_{ow}^S$.

$$\mathcal{F}^S = \mathcal{F}_i^S + \mathcal{F}_{ow}^S \tag{2.45}$$

The salt flux related to freezing and melting of ice and snow is calculated as

$$\mathcal{F}_i^S = (S_o - S_i)\frac{\rho_i}{\rho_w}\left(\frac{\partial h_i}{\partial t}\right)_t + S_o\frac{\rho_{sn}}{\rho_w}\left(\frac{\partial h_{sn}}{\partial t}\right)_t \tag{2.46}$$

where h_i and h_{sn}, $\rho_i = 910$ kg m^{-3} and $\rho_{sn} = 290$ kg m^{-3} are sea ice and snow thicknesses and densities, respectively. The subscript t indicates that only thermodynamic changes of ice and snow volume are considered. The salinity of snow is set to zero, that of sea ice S_i to 5 psu, and S_o is the salinity of the uppermost ocean model layer.
$\mathcal{P} - \mathcal{E}$ falls as rain and completely runs off the ice floes into the ocean for air temperatures greater than the surface freezing point. For $T_a < 0°C$, it accumulates as snow in the ice-covered part of the grid cell, but still provides a freshwater flux for the ice-free ocean:

$$\mathcal{F}_{ow}^S = S_o \begin{cases} \mathcal{P} - \mathcal{E}, T_a \geq 0°C \\ (1 - A)(\mathcal{P} - \mathcal{E}), T_a < 0°C \end{cases} \tag{2.47}$$

2.3.3 Momentum flux

The surface stress at the ice-ocean interface is calculated using the bulk formula

$$\tau_{io} = \rho_w c_{d,io} \mid \vec{u}_i - \vec{u}_w \mid [(\vec{u}_i - \vec{u}_w)\cos\theta + \vec{k} \times (\vec{u}_i - \vec{u}_w)\sin\theta] \tag{2.48}$$

with the turning angle $\theta = 10°$ (Timmermann et al. 2002a) and the velocity at the uppermost ocean model grid point $\vec{u}_w$. Analogously to the stress at the sea ice surface τ_{ai} in equation (2.40), that at the ice-free ocean surface is defined as

$$\tau_{ao} = \rho_a c_{d,ao} \mid \vec{u}_{10} \mid \vec{u}_{10} \tag{2.49}$$

with $c_{d,ao} = 1.0 \times 10^{-3}$. This equation assumes that the ice drift and ocean surface velocities are negligible compared to the 10-m wind speed $\vec{u}_{10}$ (Hibler 1979), i.e. that the relative velocity of wind and ice or ocean surface is essentially the wind velocity, and that surface stress and $\vec{u}_{10}$ are parallel.
The total ocean surface stress is calculated as an area-weighted average:

$$\tau_o = A \cdot \tau_{io} + (1 - A) \cdot \tau_{ao} \tag{2.50}$$

2.4 Ice shelf-ocean interaction

An important modification of water masses on the continental shelf occurs at deep ice shelf bases. Melting and freezing here initiate additional heat and fresh water fluxes. These are caused by a vertical sub-ice shelf circulation pattern known as the "ice pump" (Lewis & Perkin 1986), driven by the pressure dependence of the *in situ* freezing point of sea water. At the base of an ice shelf, i.e., several 100 meters below sea level, this is considerably lower than at the surface. Hence, even shelf water at the sea surface freezing temperature represents a heat reservoir for basal melting. The melt water input cools the parent water mass, but also reduces its density suffiently to rise along the inclined ice shelf base toward shallower regions. Here, the water can become *in situ* supercooled, i.e. it is colder than the *in situ* freezing point at this shallower depth. This leads to the formation of ice crystals in the water column and accumulation at the ice shelf base. For a sufficient density increase, the water sinks and joins the deep inflow forming part of a closed circulation. Water that exits the ice shelf cavity at temperatures below the surface freezing point is known as Ice Shelf Water (ISW).
In the model, the interaction between ice shelf base and ocean is described by the same formalism as the one between sea ice and ocean. The freezing point temperature is calculated as a function of pressure and salinity for the whole model domain. For sea ice, the inclusion of the pressure dependence has no significant effect, but under the ice shelf it enables the model to reproduce the process described above. Ice shelf extent and thickness are prescribed as constant over time, and velocities are set to zero (Timmermann et al. 2002a) reducing the sea ice model to its thermodynamic part.
Outside the cavity, wind is the main driving force of near surface currents. Evidently, inside the cavity wind is not present, friction at the ice shelf base serves as a momentum sink and tidal currents gain importance (Pereira et al. 2002).

However, these currents are not included in the model due to its rigid lid approximation. In the cavity, the velocity dependent parametrization of the heat flux between ice and ocean in equation (2.42) is replaced by

$$Q_{oi} = \rho_w c_{p,w} \gamma_T (T_o - T_f) \tag{2.51}$$

with $\gamma_T = 10^{-4}$ m s^{-1} (Hellmer und Olbers 1989, Timmermann et al. 2002a) to prevent a systematic underestimation of heat and fresh water fluxes. The value of γ_T is equivalent to a relative velocity of 15 cm s^{-1}. Model studies have shown tidally induced current speeds to be around 10 cm s^{-1} beneath Ross Ice Shelf (Padman et al. 2003) and 30 cm s^{-1} beneath Filcher-Ronne Ice Shelf (Pereira et al. 2002).

2.5 Model configuration and forcing

2.5.1 Model area, grid, and bathymetry

The model BRIOS2.2 is run on a circumpolar, periodic channel with zonal boundaries at 50°S and 82°S. Horizontally, the resolution is isotropic at 1.5° zonally and 1.5° cos(ϕ) meridionally for the whole circumpolar domain. This mesh width corresponds to 30 km at the Ross Ice Shelf edge (79°S) and 100km at the northern boundary (Fig. 2.1). The equations of the ocean model were transformed onto a curvilinear, spherical coordinate system horizontally (Hedström 1994), discretised on an Arakawa-C-Grid (Arakawa & Lamb 1977). At the model resolution this grid type provides a better representation of wave propagation than the Arakawa-B-Grid used for the sea ice model (Haidvogel & Beckmann 1999).[1] Use of the Arakawa-B-grid for the sea ice model, however, allows for easier implementation of the sea ice rheology. Vertically, a terrain (and ice shelf base) following coordinate system is employed. The use of S- or σ-coordinates avoids the step-like topography typical of models with geopotential vertical coordinates, e.g., the GFDL Modular Ocean Model (MOM) (Pacanowski 1996). This allows for a better representation of downslope flow and increased vertical resolution in shallow areas (Fig. 2.2). BRIOS2.2 has 24 vertical levels with increasing resolution near surface and bottom.

The bottom topography was prescribed from Smith & Sandwell (1997) north of 72°S with ETOPO5 data used between 72°S and 82°S. Ice shelf and water column

[1] For grid structures see Appendix A.

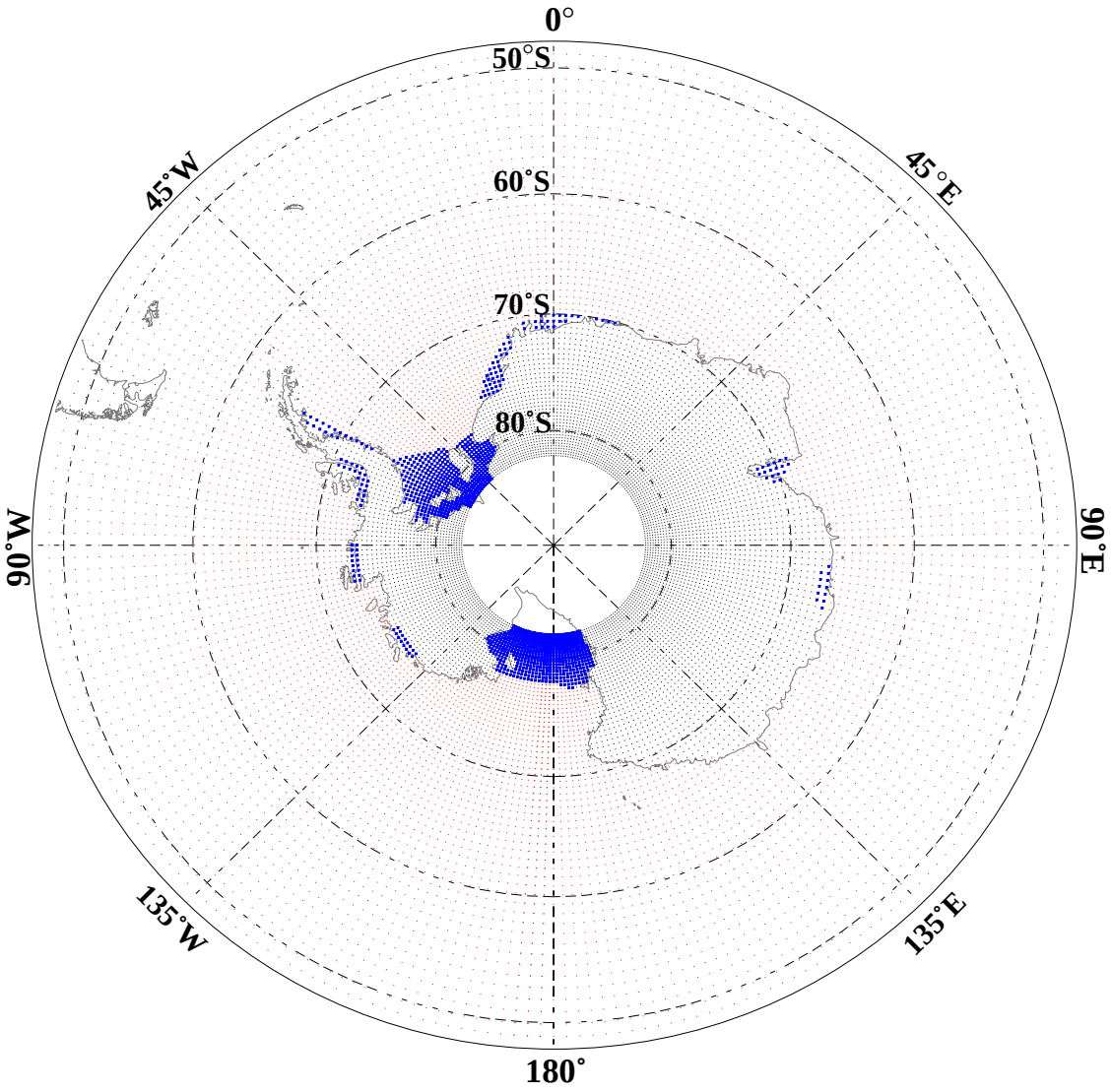

Figure 2.1: Horizontal model grid for scalar quantities superimposed on a map of Antarctica's coastline. Grid points representing the open ocean are marked red, those representing the sub-ice shelf cavities marked blue.

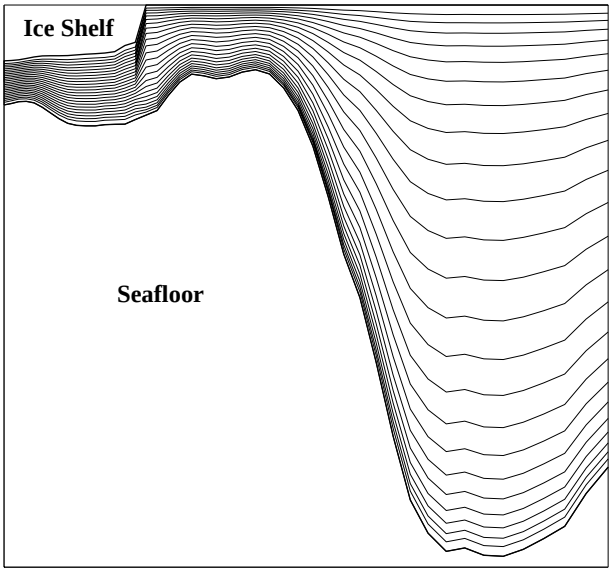

Figure 2.2: Vertical distribution of model layers on a section along 180°. Layer thicknesses at the minimum model water column thickness of 200 m are equidistant at ~ 8 m. At the maximum water column thickness within the model domain (5500 m) layer thicknesses are ~ 400 m in the middle of the water column, and 60 to 80 m near surface and bottom.

thickness data for the big ice shelf cavities were taken from Greischar et al. (1992) (Ross) and Johnson & Smith (1997) (Filchner-Ronne). All other ice shelves were given a thickness of 200 m (Fig. 2.3). The topographical data was interpolated bilinearly onto the model grid and smoothed by a nine-point operator. A lower limit of 200 m is imposed on water column thickness in the shallow regions, i.e., close to the coast and near the grounding lines in the ice shelf cavities. Since the southern model boundary is located at 82°S, only 80 % of the Ross Ice Shelf area is represented in the model. However, because much of the area south of 82°S has water column thicknesses less than 200 m (Greischar & Bentley 1980), inclusion of this area would have led to artefacts in circulation and melt rate.

2.5.2 Model initialisation and boundary conditions

Hydrographic data (Θ and S) for initialisation and open northern boundary restoring were taken from the WOCE Hydrographic Programme Special Analysis Centre (Gouretski et al. 1999) and interpolated trilinearly onto the model grid. Due to the lack of data in the ice shelf cavities, Θ and S are initiated as linear profiles increasing with depth (Beckmann et al. 1999). There is no sea ice cover

present initially and sea ice and ocean velocities are set to zero.
Along the northern model boundary temperature and salinity are nudged towards the WOCE Hydrographic Programme Special Analysis Centre climatology (Gouretski et al. 1999) over a strip five grid cells wide using a linear damping term with decreasing time scale towards the boundary. No other flux corrections or restoring to observed distributions are used.

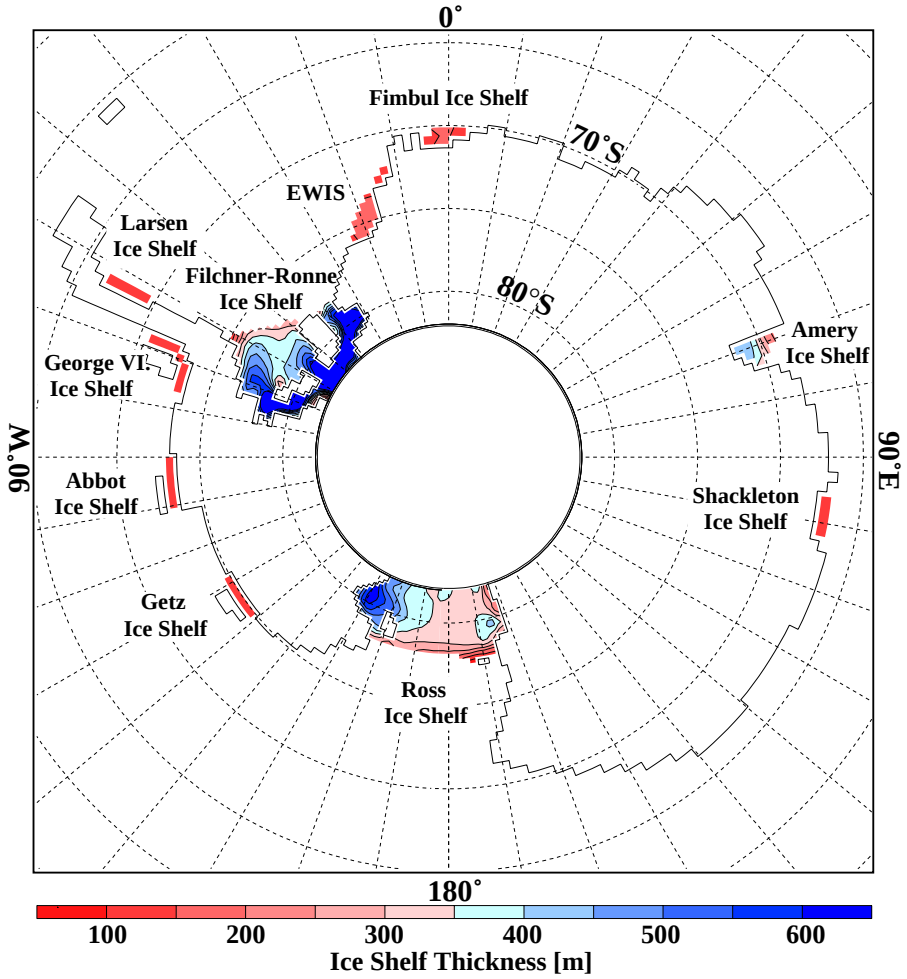

Figure 2.3: Location of ice shelves included in BRIOS2.2 and their thickness. EWIS = Eastern Weddell Ice Shelves.

Since the Antarctic Circumpolar Current is not fully included in the model domain, assumptions have to be made about its course at 50°S. As in Timmermann et al. (2002a) and Beckmann et al. (1999), transport through Drake Passage is set to 130 Sv (Whitworth & Peterson 1985). Half of this is extracted from the model domain between the east coast of South America and 30°W, and reintro-

duced between 120°E and 180° in the Indian Sector.

2.5.3 Atmospheric forcing

For atmospheric forcing, daily NCEP Reanalyses data for 10-m wind speed, 2-m air temperature, specific humidity, cloudiness, and net precipitation ($\mathcal{P} - \mathcal{E}$) were used for the period from 1948 to 2001. The period from 1948 to 1957 was used as spin-up time for the model while the years 1958 to 2001 were used for analysis. In some cases only data after 1978 was used since prior to this year the NCEP Reanalyses do not include satellite data and are, therefore, believed to be less accurate. See Appendix B for validation of NCEP winds in the Amundsen Sea.

Chapter 3

Sea ice conditions in the Pacific sector of the Southern Ocean

As described in the introduction, sea ice conditions in the Pacific sector of the Southern Ocean vary widely and are an important factor in explaining the properties of the ocean beneath. To facilitate understanding of the oceanic conditions described in the next chapter, in this chapter an overview of sea ice conditions in the Bellingshausen, Amundsen and Ross Seas will be given. Results of the model BRIOS2.2 will be presented, comparing them to observational data wherever available as model validation. A 24-year quasi-climatological mean annual cycle from 1978-2001 will be used since most observations are available during this time period.

3.1 Sea ice concentration and extent

Sea ice concentration is the prognostic variable of the sea ice model most straightforward to validate. Satellite remote sensing data, obtained from the SSM/I data using the bootstrap algorithm (Comiso, 1999), provide an extensive data base of both spatial and temporal coverage. SSM/I satellite observations are available between October 1978 and September 2001. The accuracy of SSMI/I bootstrap sea ice concentrations is taken to be about 5-10 % in winter and 15-20 % in summer (Comiso et al. 1997, Cavalieri et al. 1999).
The most striking feature about Antarctic sea ice is its large seasonal cycle. The area it covers increases by a factor of five from summer to winter. While at maximum sea ice extent (September) most of the area South of 60°S is covered

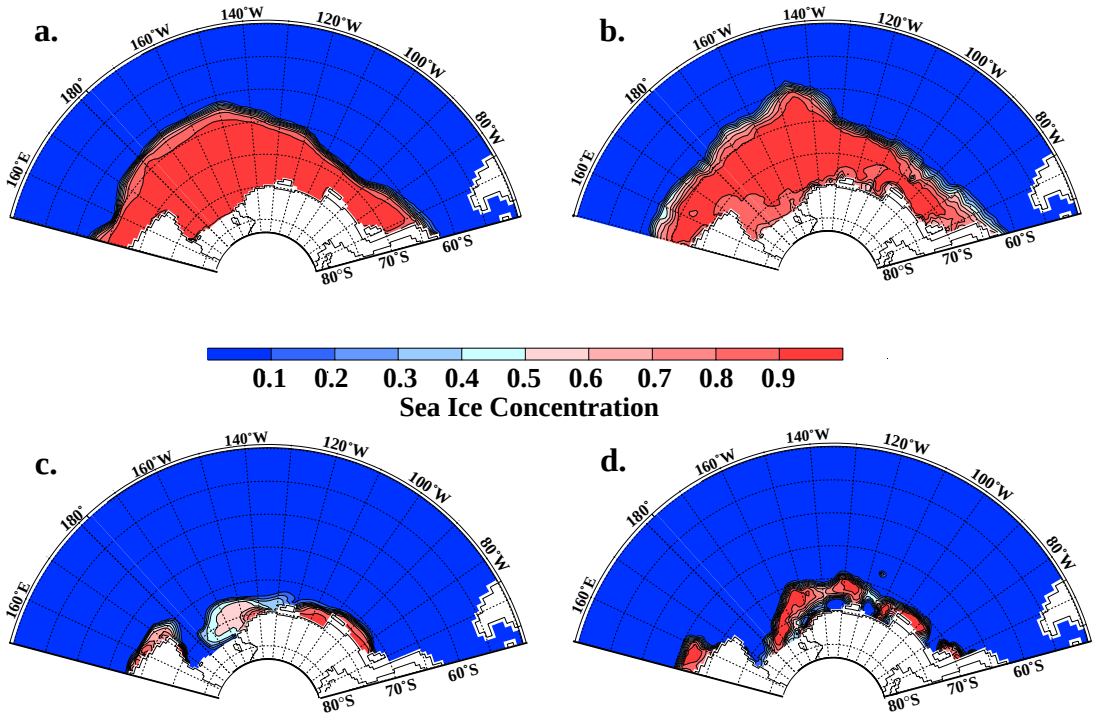

Figure 3.1: Monthly mean distribution of sea concentration in the Pacific sector of the Southern Ocean for February 1998, a) model and b) SSM/I data, and for September 1998, c) model and d) SSM/I data representing conditions at sea ice minimum and maximum, respectively.

by sea ice, at minimum extent (February) the Amundsen, Bellingshausen and eastern Ross Seas are the only areas with significant sea ice cover apart from the southwestern Weddell Sea. The most commonly used measure of sea ice coverage is the sea ice extent which includes the area of every grid box containing sea ice concentrations $> 15\%$. The inherent error in the SSM/I data will not affect the sea ice extent strongly neither in winter nor in summer, since concentrations are generally well above the threshold value except for a narrow band along the sea ice edge (Fig. 3.1).

Simulated September sea ice extent agrees well with SSM/I data within the error margin for the entire Southeast Pacific Sector and the Amundsen and Ross Seas (Fig. 3.2). For the Bellingshausen Sea the underestimation is slightly larger than the error margin with 12 %. An overestimation of the westerly wind speeds in the NCEP reanalyses in the Bellingshausen Sea (N. van Lipzig, personal com-

munication) might lead to sea ice being driven east up to the western coast of the Antarctic Peninsula and not northward to its tip as observed (Fig. 3.1a & b). This may also be the reason for a September maximum in sea extent, rather than the more symmetrical seasonal cycle with an August maximum observed as characteristic for this area (Jacobs & Comiso 1997).

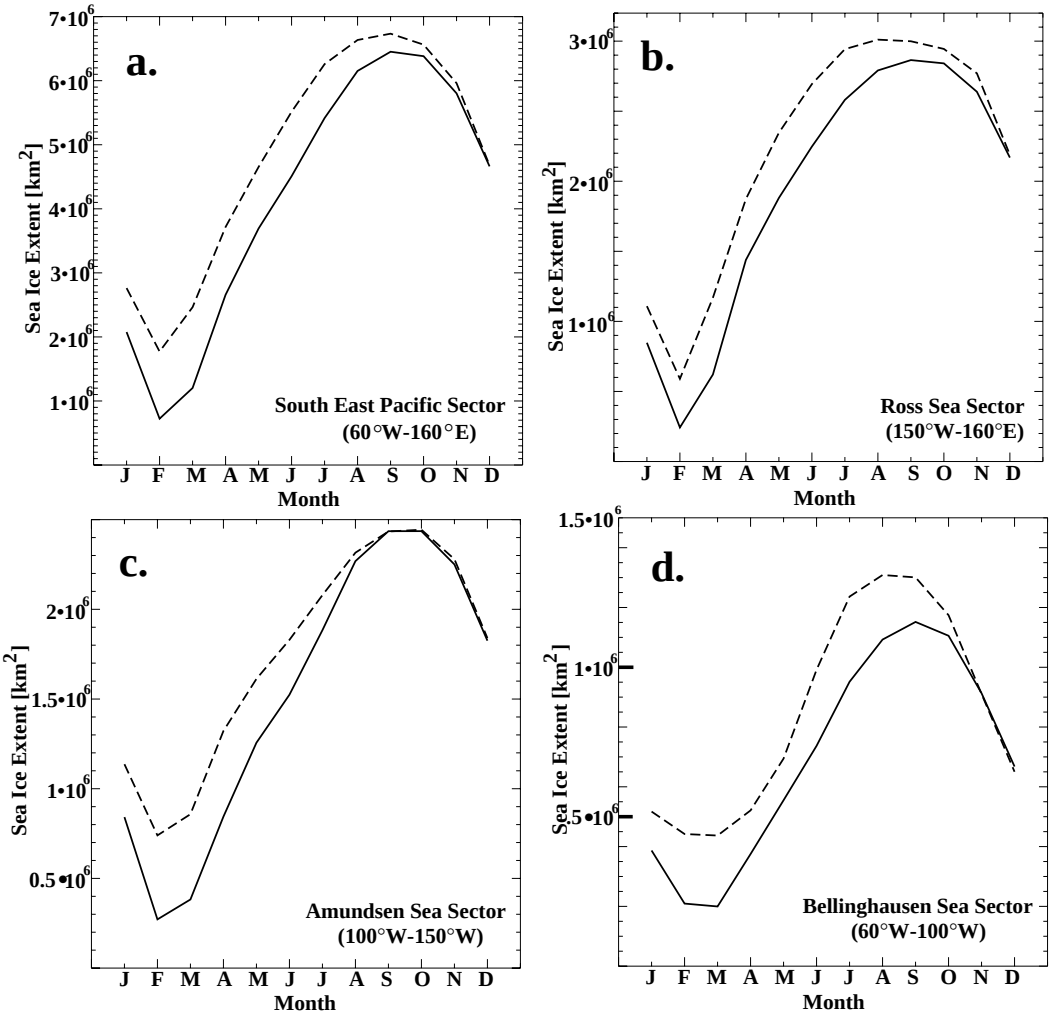

Figure 3.2: Mean annual cycle (1979-2000) of simulated (solid lines) and SSM/I (dashed lines) sea ice extent for the South East Pacific sector and its subsectors as marked on each panel. Sea ice extent is defined as the area over which sea ice concentration exceeds 15%. SSM/I data were only available from October 1978 - September 2001 (Comiso, 1999), hence the mean only incorporates the years 1979 to 2000.

In summer, the model sea ice coverage is too small with February ice extent underestimated by 60 %, i.e., well beyond the error margin of the SSM/I data (Fig. 3.2). Specifically, the tongue of high sea ice concentration that survives summer in the eastern Ross Sea and the patch of sea ice north of George VI Ice Shelf are not reproduced in the model (Fig. 3.1 c & d). This misrepresentation may be due to the high sensitivity of the summer sea ice cover to errors in ocean surface temperatures and currents and the atmospheric radiation balance (Timmermann 2000). Another explanation related to model resolution is discussed in more detail in the next section.

3.2 Sea ice thickness

The second quantity that characterizes sea ice in the model is its thickness (Section 2.2). Since one focus of this thesis will lie on sea ice volume and transport, which depend on a reasonable representation of sea ice thickness, this section provides some validation of the modelled thicknesses. However, as yet no technique has been devised to provide distribution maps of continuous spatial and temporal coverage. Hence, validation will necessarily be confined to isolated patches in time and space.

The simulated spatial distribution of sea ice thickness at maximum extent shows several features not obvious from the modelled distribution of sea ice concentrations. The Ross Sea polynya is a well-described feature in the sea ice characteristics of the Ross Sea (Zwally et al. 1985). Although simulated sea ice concentrations only show a polynya in November (spring), modelled mean sea ice thickness for September (winter) is reduced (< 0.7 m) in the southwestern Ross Sea (Fig. 3.3) where the polynya has been consistently observed (Jacobs & Comiso 1989). A tongue of thick sea ice (> 1.5 m) extends into the eastern Ross Sea from the Amundsen Sea, in agreement with observations by Jacobs & Comiso (1989). Both Amundsen and Bellingshausen Seas show large areas of thick sea ice along the coast extending north to 70°S. Here, sea ice thicknesses up to 3 m are produced by the model.

In January 1999 sea ice thicknesses were measured along two meridional transects through the ice pack along 135°W and 150°W (T. Tin and M. Jeffries, personal communication, 2002). These data are compared to the modelled January means for 1999, 2000 and 2001, and to a 24-year January mean from 1978-2001 (Fig. 3.4). The observed data are essentially snapshots over an area of approximately 1km^2

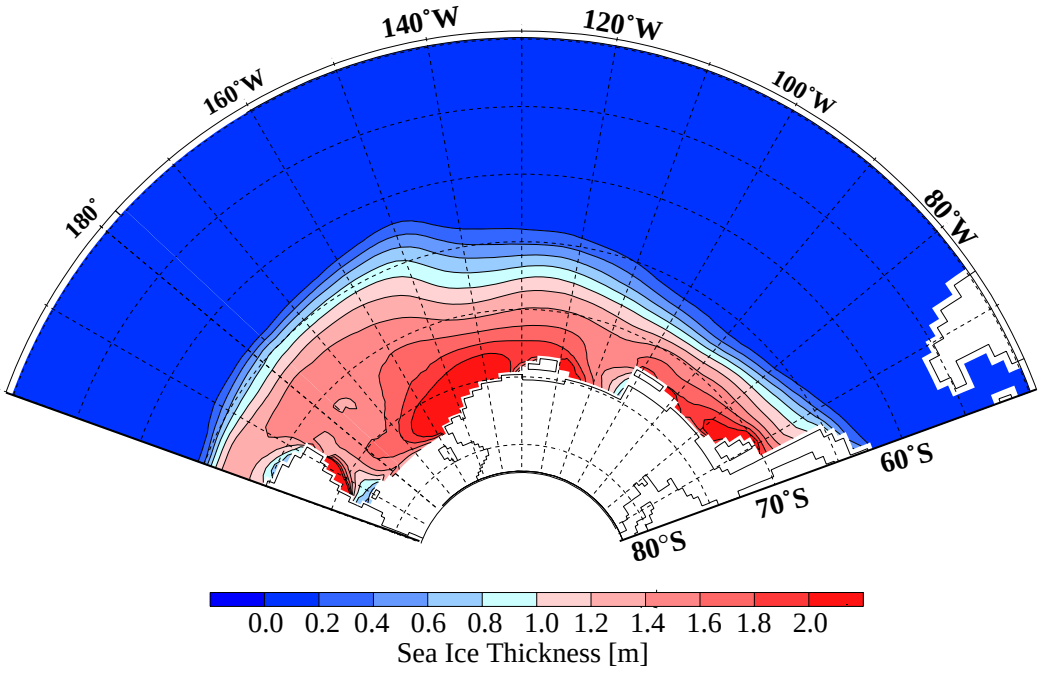

Figure 3.3: Simulated sea ice thickness distribution for September. Shown is a 24-year mean (1978-2001).

(Worby & Allison 1999) every 16km of the ship's track. They were smoothed with a three-point running mean to make their scale of variation comparable to the 50×50km model resolution. In the case of in situ samples like ice cores a bias will exist, since only floes with a thickness and size sufficient to carry the observers safely can be used. In areas of thin sea ice this will lead to an overestimation of thickness. For ship based observations an underestimation of sea ice thicknesses exists in areas with heavy sea ice cover, since the ship will necessarily follow leads and areas of thin ice. The thickness of massive floes can only be estimated and is hence highly observer-dependent.

The spatial variability in the observations is higher than that of the model results even after smoothing due to different data set footprints. However, there is a reasonable general agreement between model and observations over both sections for 1999, but with observations showing greater sea ice thicknesses especially toward the South. Sea ice deformation by onshore winds is included in the model, but smaller scale processes, like ridging and rafting, while parametrized in the model, are caused by spatial and temporal atmospheric variability that occurs faster or on smaller spatial scales than the resolution of the NCEP data can

capture. Areas like the Bellingshausen, Amundsen and Eastern Ross Seas are strongly affected by these processes (Tin et al. 2003) and heavily deformed multiyear ice is common. The underestimation of the simulated thickness of this near-coast ice (Fig. 3.4) may help to account for the underestimation of sea ice concentration in summer, since thinner ice is more prone to melting completely in summer. The amount of multiyear ice that is still present the following winter in the model is reduced and the observed sea ice thicknesses are not reached. As an example, above-average sea ice thicknesses in January 2001 (Fig. 3.4) led to a sea ice extent in close agreement with satellite observations during the subsequent summer. Comparison with the long-term mean shows that 1999 can be regarded as a typical year, while results for 2000 and 2001 demonstrate a considerable range of variability (Fig. 3.4).

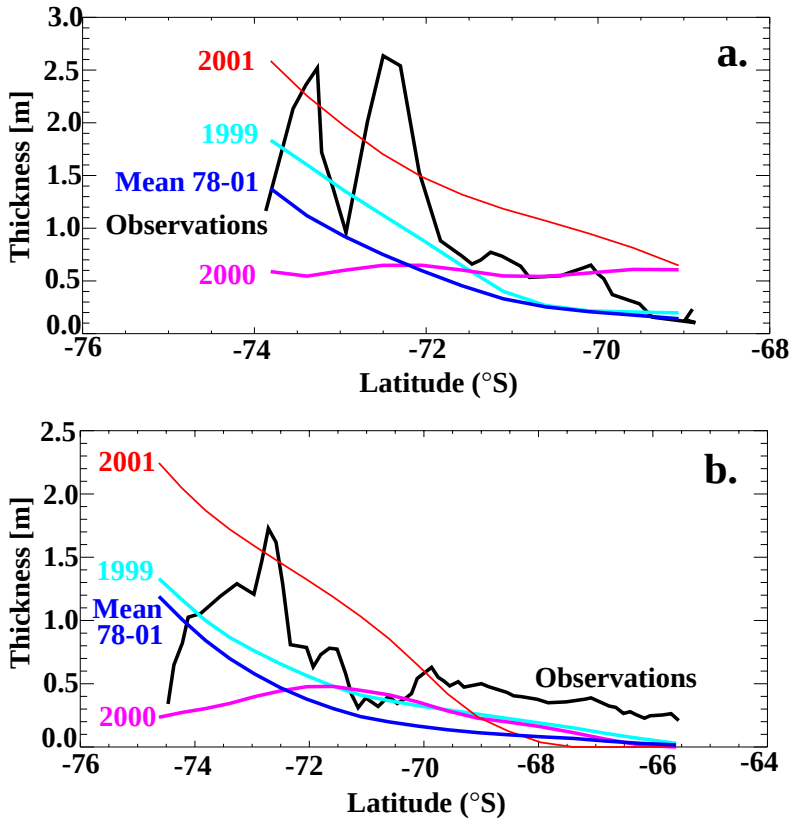

Figure 3.4: Sections of sea ice thickness in January along 135°W (a) and 150°W (b). The observed data, measured in 1999, essentially snapshots over an area of approximately 1km^2 (Worby & Allison 1999) every 16km of track, were smoothed with a three-point running mean to make its scale of variation comparable to the 50×50km model resolution.

Winter sea ice thicknesses were compared to data from two cruises: the first one in August and September 1993 covering the Amundsen and Bellingshausen Seas between 70°W and 110°W (Worby et al. 1996) and the second one in September and October 1994 covering the Amundsen and eastern Ross Seas between 110°W and 170°W (Jeffries et al. 1998). Both cruises covered latitudes only from 66°S to 71°S, since the heavy ice pack precluded access further South.
The first cruise in the Bellingshausen Sea yielded two values for mean sea ice thickness: 0.90 ± 0.64 m, obtained from a set of in situ drilling measurements, and 1.29 m from synoptic, ship-based estimates. For the same months over the same area the model shows values of 0.79 ± 0.60 m for 1993 and 0.90 ± 0.57 m as a long-term mean. Both of these are well within the observation's standard deviation and standard deviations of a similar magnitude for both model and observations indicate that the simulated sea ice thickness distribution is reasonable. During the second cruise in the Amundsen and eastern Ross Seas the observations yield a mean ice thickness of 0.84 ± 0.46 m, while model results for the same time and area are 0.97 ± 0.37 m, i.e. higher by 13%, but well within the observation's standard deviation. The 24-year mean model sea ice thickness for September and October from 1978-2001 of 1.12 ± 0.40 m indicates that in the model 1994 was a year with a relatively thin sea ice cover in this area. The good agreement of modelled and observed sea ice thicknesses and their standard deviations provides confidence in the following values for sea ice transport and volume calculated from model results.

3.3 Sea ice drift - large scale pattern

This section will give an overview of the characteristics of the modelled sea ice drift in Bellingshausen (60°W - 100°W), Amundsen (100°W - 150°W), and Ross Seas (150°W - 160°E). Validation and an investigation of the driving forces of sea ice drift are provided in Chapter 5.
The modelled sea ice drift pattern in the Ross Sea agrees well with that deduced from satellite observations by Drinkwater et al. (1999). Sea ice drift in the western Ross Sea is directed to the north with velocities up to 15 cm s^{-1} (Fig. 3.5) due to strong, predominantly southerly winds (Fig. 3.6). At Cape Adare, the sea ice either joins the west wind drift of the ACC region, or continues westward along the Adelie Land coast driven by the katabatic winds blowing from the Antarctic Plateau.

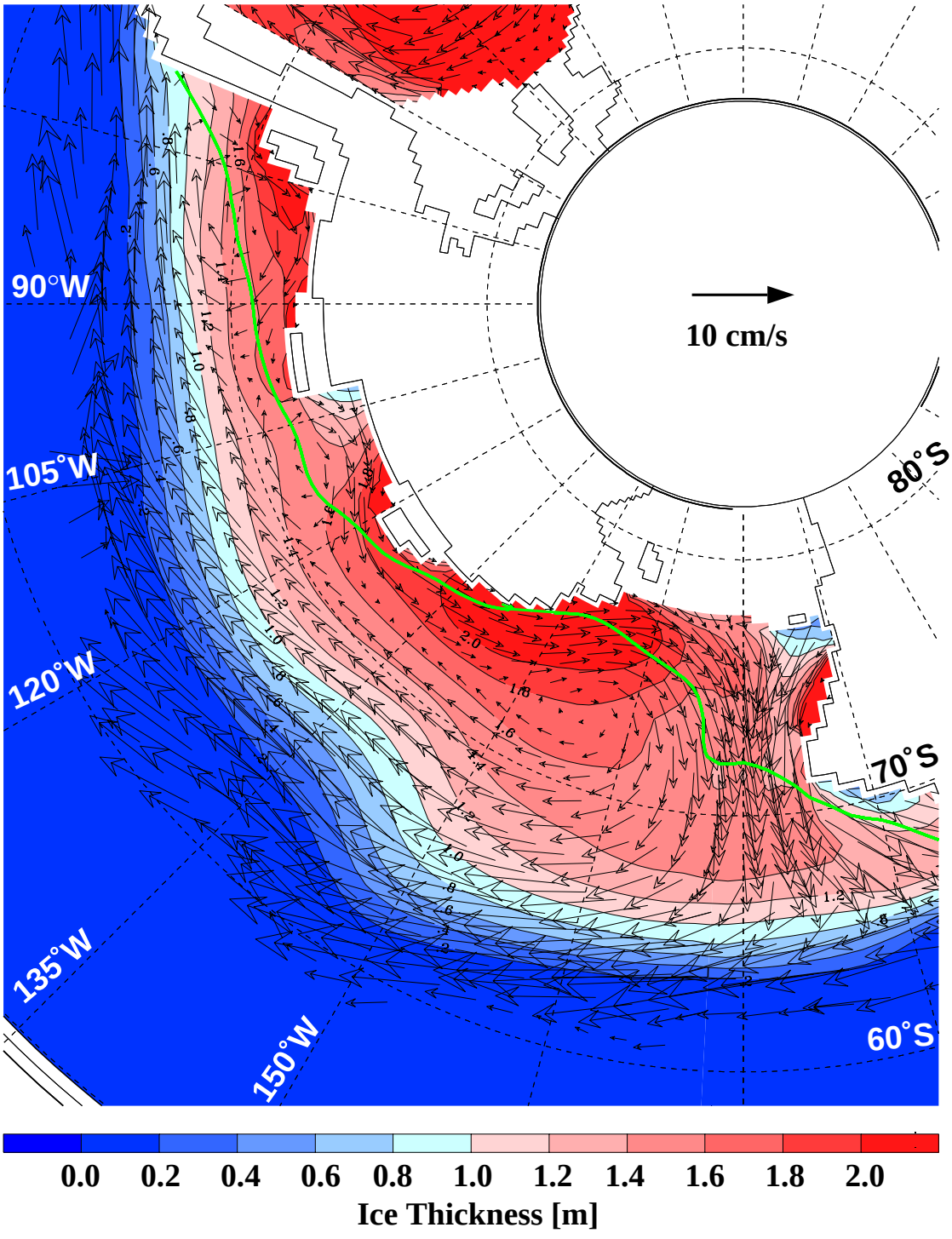

Figure 3.5: September mean (1978-2001) modelled sea ice drift velocities (vectors) and thickness (colour coded). For better visibility only every second vector is plotted. The continental shelf break as represented in the model is marked by the green line.

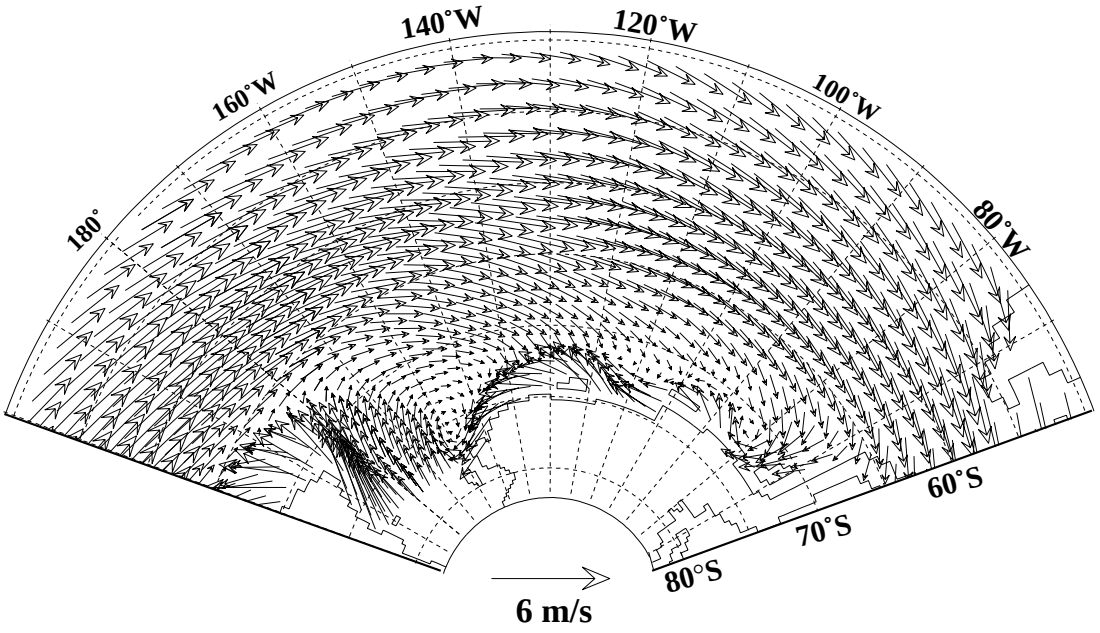

Figure 3.6: September mean (1978-2001) NCEP 10-m wind velocities. For better visibility only every second vector is plotted.

Sea ice generated in the southern Amundsen Sea drifts westward into the Ross Sea. In the eastern Ross Sea wind velocities are considerably lower than in the west and form a quasi-cyclonic feature (Fig. 3.6, see also Jacobs & Comiso 1989). Consequently, this leads to the tongue of thick sea ice extending into the eastern Ross Sea mentioned in the previous section.

In the Amundsen and Bellingshausen Seas the most prominent features are a 5-7 cm s^{-1} westward drift within 100-300 km of the coastline and a larger zone of eastward drift extending northward to the sea ice margin (Fig. 3.5), where speeds are $\geq$ 15 cm s^{-1}. These regimes are separated by a transition zone of low velocities (1-2 cm s^{-1}) and variable direction that runs roughly along the continental shelf break from the Antarctic Peninsula to $\sim$ 120°W. Westward up to 160°W, the continental shelf narrows, but the transition zone remains near 72°S into the eastern Ross Sea, as a result of the meridional extension of the easterly winds (Fig. 3.6).

Most sea ice produced in the Bellingshausen Sea is exported north into the eastward flowing ACC toward Drake Passage forming a cyclonic drift pattern. Regions of almost stagnant sea ice drift between Amundsen and Bellingshausen Seas (95°W-100°W) coincide with some of the more persistent areas of summer ice both in the model and observations (Gloersen et al. 1992). Strong easter-

lies drive sea ice westward from Pine Island Bay resulting there in low sea ice thicknesses (Fig. 3.5) and high growth rates (see below).

3.4 Sea ice growth

The melting and freezing of sea ice constitutes a major source and sink of fresh water in the Southern Ocean (Timmermann et al. 2001). In liquid sea water impurities such as Na^+ and CL^- ions, the constituents of salt, and H_20 molecules form clusters due to their strong polarity. Despite having a lower molecular packing density, the rigid structure of the tetrahedral ice crystal lattice prevents these ions to be incorporated during sea ice formation (Eicken 2003). This process is known as brine release and can either be interpreted as an addition of salt to or as an extraction of freshwater from the ocean surface. Similarly and obviously, the melting of sea ice represents a source of fresh water with sea ice bulk salinities between 3 and 6 psu versus surface water salinities around 34 psu.
In the previous section it was pointed out that the ice pack undergoes considerable drift - a speed of 10 cm s^{-1} corresponds to a distance of 1500 km covered during the 6 month winter season. Together with regional differences in the energy balance this leads to areas where sea ice is predominantly formed or melted throughout the year. The distribution of these areas is illustrated by the net sea ice growth rate which is the local balance of melting and freezing over one seasonal cycle (Fig. 3.7).
As expected, predominant areas of freezing occur near the coast and of melting near the northern edge of the ice pack. The continental shelf only experiences 3 months (December to February) of melting per year, while near the northern ice edge, where sea surface temperatures exceed the freezing point all year round, a broad band of melting is present even in winter. Sea ice in this region is only present due to advection and not due to local thermodynamic growth. Patches of net sea ice melting on the Amundsen and Bellingshausen continental shelves are due to the early onset of strong melting in December (Bellingshausen) and January (Amundsen), a feature imprinted by the NCEP forcing data.
Mean net annual growth rates for the area south of 70°S are 1.50 ± 0.24 m a^{-1}, 0.54 ± 0.30 m a^{-1}, 0.81 ± 0.39 m a^{-1} in the Ross (Cape Adare to 150°W), Amundsen (150°W to 100°W) and Bellingshausen Seas (100°W to 60°W), respectively. The Ross Sea is the main formation site of sea ice in the southeast Pacific sector. This is especially true west of 180° with a net growth rate of 2.57

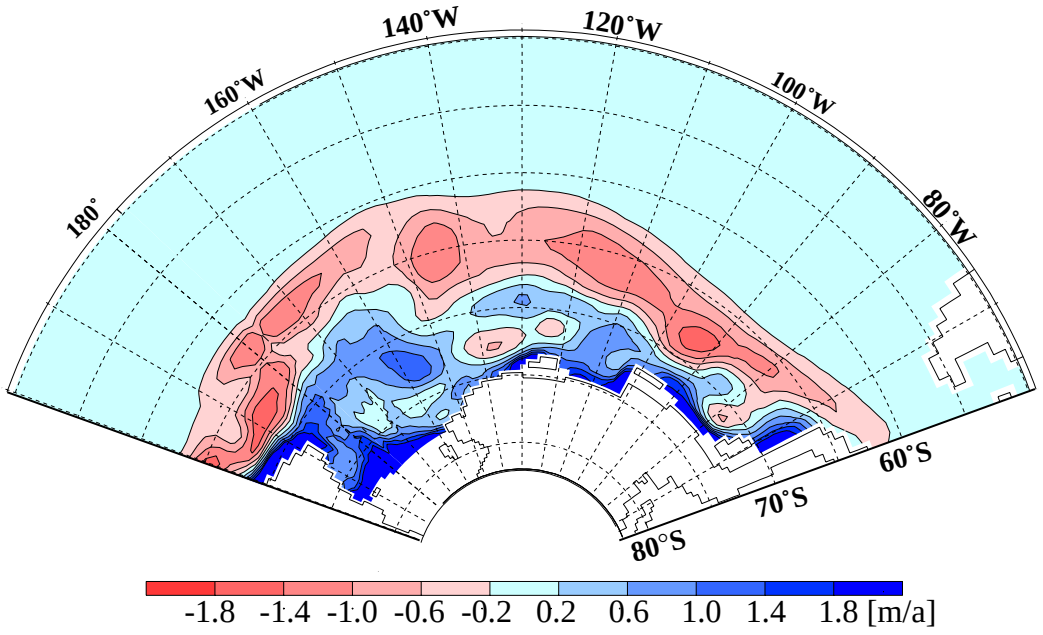

Figure 3.7: Net sea ice freezing in the Southeast Pacific sector as a mean for the years 1978-2001. Negative freezing rates denote melting.

$\pm$ 0.37 m a^{-1}. East of this line the net growth rate is 1.03 $\pm$ 0.24 m a^{-1} and high sea ice growth rates are mainly found along the Ross Ice Shelf edge.
In addition, high production sites are located in Pine Island Bay, off Adelie Land, and along several other stretches of coast. In most cases these regions correspond to areas of reduced sea ice concentration and thickness (Fig. 3.3). Katabatic winds, directed offshore and transporting very cold continental air masses especially in winter, cause coastal polynyas which are only several kilometres wide and hence sub-grid scale. However, the model reproduces the alternation between convergent and divergent ice drift due to the passage of low pressure systems and hence the areas of reduced ice concentration with high growth rates.
The largest of these coastal polynyas is the Ross Sea polynya. Strong, persistent off-shore winds in combination with a thermally homogenized water column in this area suggest that it can be characterized as a latent heat polynya. Located on a broad continental shelf, the polynya has a strong oceanic influence, since it allows for the formation of highly saline shelf waters. Along the Ross Ice Shelf edge the monthly mean sea ice growth rate exceeds 3 cm d^{-1} between March and September reaching a maximum of 5.42 cm d^{-1} in April and a minimum in December at -1.31 cm d^{-1} in phase with the general seasonal cycle of sea

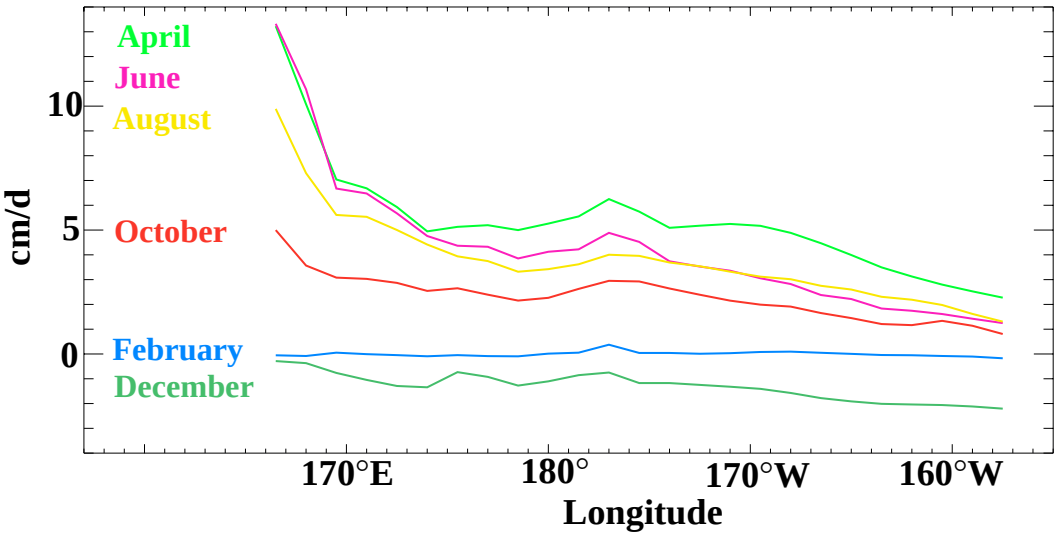

Figure 3.8: Zonal section of the 24-year (1978-2001) mean of sea ice growth rates along the Ross Ice Shelf edge. Shown are monthly mean values of the first grid box north of the ice shelf edge. Months are colour-coded.

ice growth. There is a strong gradient between the eastern and western part (Fig. 3.8). To the east, sea ice formation stays fairly constant around 1 and 2 cm d^{-1} between March and September; to the west, sea ice growth rates vary between 8 and 13 cm d^{-1} reaching a maximum between April and June. The origin of this gradient lies in the presence of separate wind and sea ice regimes in the eastern and western Ross Sea as described in more detail in the sections on sea ice drift (3.3) and transports (5.2). This difference is also reflected in an equally strong westward gradient in shelf water salinities, as shown in section 4.3.

3.5 Summary

This section has provided a background on sea ice conditions in the Pacific sector of the Southern Ocean and validation of model results. Sea ice conditions in the western Ross Sea are determined by steady and strong southerly winds that drive the sea ice northwards along the Victoria Land coast. This leads to high growth rates, relatively thin sea ice, the existence of the Ross Sea polynya, one of the most regular spring polynyas around Antarctica, and a continental shelf that is generally ice-free in summer. Both Amundsen and Bellingshausen Seas contain large volumes of thick multiyear ice along the coast which extend into the eastern Ross Sea and are associated with low sea ice formation. Sea ice drift is mainly

directed zonally in these regions with the only area of clearly northward drift being the western Ross Sea.

About 50% of Ross Sea ice are formed west of 180°, in an area that represents roughly one quarter of the Ross Sea. The corresponding net growth rates are consistent with the east-west salinity gradient along the Ross Ice Shelf edge (Jacobs & Giulivi 1998). Killworth (1974) proposed, however, that upwelling of denser subsurface water masses at the western end of the shelf is necessary to sustain the observed density gradient. The high sea ice formation rates and their eastward decrease would perhaps lessen the need for this process or enhance its effect.

Chapter 4

Ocean properties and circulation

4.1 Water mass characteristics and distribution

> *"This morning we had a very light breeze from the N.E., and towards noon it fell properly calm, with the surface of the ocean beautifully smooth; thus affording a most favourable opportunity of trying its temperature at great depth. A new line had been prepared for the purpose, and thermometers were attached to it at intervals of one hundred and fifty fathoms: we had no soundings with eleven hundred fathoms, and beyond this I did not venture to send the thermometers."*[1]

Thus describes James Clark Ross the apparatus he and his crew used to obtain the first oceanographic measurements in the Ross Sea and environs. These observations of ocean properties certainly count among the earliest in the Southern Ocean. Part of one of the first dedicated programmes of scientific investigation in this region they are of great fascination and value. On the 2 January 1842, during his second expedition to the Ross Sea, Ross states the following:

> *"...and to-day at noon our latitude was 66° 34'S., and longitude 156° 22'W. The temperature of the sea was found to be 39.6° at one thousand and fifty fathoms, whilst at the surface it was only 28°. It was also tried at intermediate depths, at intervals of one hundred and fifty fathoms, and found progressively to increase from the surface to the greatest depth."* [2]

[1] Ross (1847). 1 fathom = 6 ft $\sim$ 1.80 m

[2] 1050 fathoms correspond to $\sim$ 1920 m, 39.6F to $\sim$ 4.2°C and 28F are $\sim$ -2.2°C. The latter

Ross describes the characteristic temperature profile found in the Southern Ocean seasonal ice zone with a thin layer of cold, fresh water overlying the warm salty bulk of the Circumpolar Deep Water (CDW). This water mass fills most of the deep ocean at S > 34.68 and T > 1.0°C (Trumbore et al. 1991). Its deep maximum in salinity (34.75 at 1.7°C) can clearly be identified in the model (Fig. 4.1 a) and observations (Fig. 4.1 b) and results from North Atlantic Deep Water (NADW) as the source for this water mass. CDW is the only external-origin water mass that approaches the Antarctic continental shelf. All other water masses present are derived from it by mixing and cooling and by the input of freshwater, i.e. meltwater, precipitation or brine.

Overlying the CDW, which takes up most of the water column, is Antarctic Surface Water (AASW). This relatively fresh (S < 34.3) layer shows a wide range of temperatures from the surface freezing point up to a few degrees above zero in the model (Fig. 4.1). The wide temperature range is due to warming and freshening during the summer decay of the sea ice cover and cooling and convective mixing due to winter sea ice production. On the Ross Sea continental shelf much of AASW is transformed into shelf water as deep convection occurs due to sea ice formation. Shallowing of the mixed layer in summer leaves a core of cold Winter Water (WW) around 100 - 200 m as a remanent of previous winter mixing. The model overestimates sea ice melting in spring and summer. Consequently, modelled summer AASW salinities are too low due to the overestimated fresh water flux in the seasonal sea ice zone, while increased radiative heating of the sea surface results in an overestimation of simulated AASW temperatures (Fig. 4.1 a & b).

The Antarctic Circumpolar Current (ACC) aproaches the continent more closely in the South East Pacific sector than e.g. in the Atlantic sector (Orsi et al. 1995). Consequently, the water masses here are warmer than in the Weddell Sea. Along the Amundsen and Bellingshausen Sea coast CDW even enters the narrow continental shelf leading to high basal melt rates of the fringing ice shelves and glaciers (Hellmer et al. 1998). In the model the Getz and George VI ice shelf cavities contain waters with temperatures up to 0.5°C and salinities > 34.0

suggests a large uncertainty on the measurements since this value is well below the surface freezing temperature of seawater at -1.85°C. The temperatures given by Ross are probably *in situ* values rather than potential temperatures, a measure which is used more commonly nowadays. Since this does not change the line of argument to be followed with these quotations, temperatures were not converted.

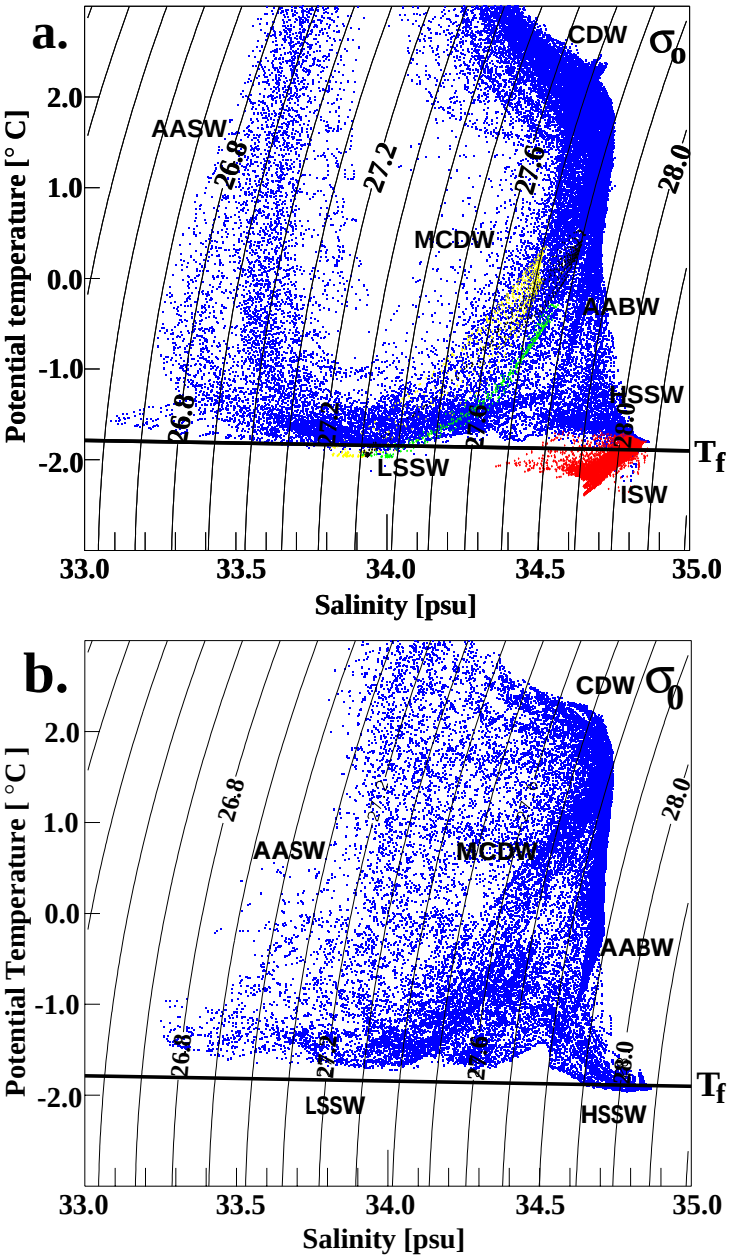

Figure 4.1: Θ/S characteristics for the South East Pacific Sector (130°E to 65°W, South of 55°S). **a.** Model results. 24-year (1978-2001) quasi-climatological mean. **b.** Observations taken from the WOCE Hydrographic Programme Special Analysis Centre data set. Grid points in the open ocean are marked blue, those in the cavities of Ross Ice Shelf red, George VI Ice Shelf yellow, Abbot Ice Shelf green, and Getz Ice Shelf black. The diagram is supplemented by isopycnals (σ_0) and surface freezing temperature (T_f). HSSW = High Salinity Shelf Water, LSSW = Low Salinity Shelf Water, ISW = Ice Shelf Water, MCDW = Modified Circumpolar Deep Water, AASW = Antarctic Surface Water, CDW = Circumpolar Deep Water, AABW = Antarctic Bottom Water. Water mass definitions according to Gouretski (1999) and Trumbore et al. (1991).

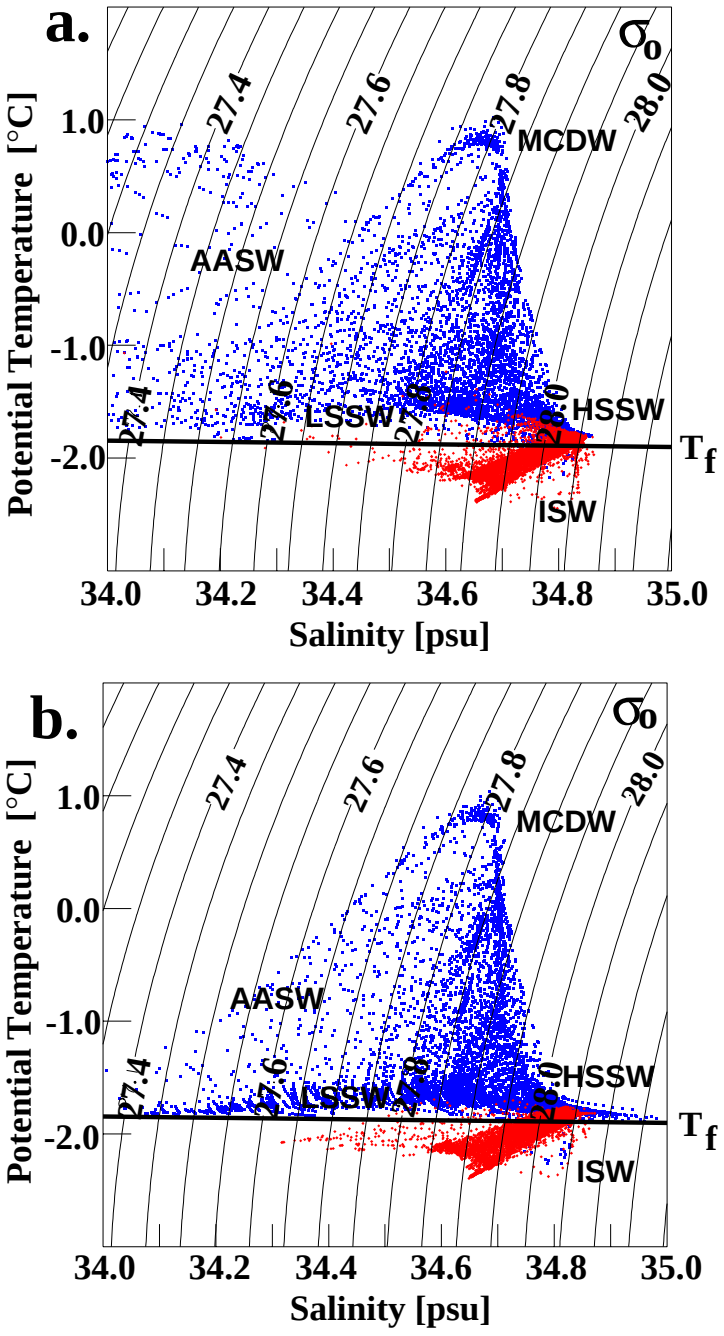

Figure 4.2: Modelled θ/S characteristics for the Ross Sea continental shelf (bottom depth $\leq$ 1000m). Grid points in the open ocean are marked blue, those in the ice shelf cavity red: **a.** Summer. February 24-year (1978-2001) mean. **b.** Winter. September 24-year (1978-2001) mean. The diagram is supplemented by isopycnals (σ_0) and freezing temperature (T_f) relative to sea surface pressure. HSSW = High Salinity Shelf Water, LSSW = Low Salinity Shelf Water, ISW = Ice Shelf Water, MCDW = Modified Circumpolar Deep Water, AASW = Antarctic Surface Water. Water mass definitions according to Trumbore et al. 1991.

(Fig. 4.1 a). In contrast, Warm Deep Water, the water mass that approaches the continental shelf in the Weddell Sea, is lower in temperature and salinity than its CDW parent, since it is cooled and freshened as it is exposed to cold and fresh continental margin waters as it circulates within the eastern cell of the Weddell Gyre (Deacon 1979). Oceanic deep water penetrating on to the Ross Sea continental shelf is converted to Modified Circumpolar Deep Water (MCDW) mainly by cooling. Its characteristic salinity at just over 34.7 is well-preserved in the model (Fig. 4.2), as the modelled temperature maximum at 0.9°C agrees well with observations (Jacobs & Giulivi 1998).

The vigorous and persistent sea ice formation in the Ross Sea polynya results in the Ross Sea continental shelf containing the densest water masses in the Southern Ocean. Potential densities $\sigma_0 > 28.0$ and salinities up to 35.0 mark the High Salinity Shelf Water (HSSW) formed on the southwestern continental shelf within the polynya area. Comparing the modelled mean θ/S characteristics on the Ross Sea continental shelf for February (summer) and September (winter), the peak salinity of the High Salinity Shelf Water (HSSW) clearly shows the strong brine input to the water column due to sea ice formation by rising from 34.85 in February to 35.0 in September (Fig. 4.2). The summer value lies within the range observed over a 33-year period in the vicinity of Ross Island (Jacobs & Giulivi 1998). A seasonal signal can also be seen in the minimum temperature of the Low Salinity Shelf Water (LSSW) formed on the eastern Ross Sea continental shelf. While this is near the surface freezing point at -1.85°C in September (Fig. 4.2 b) it rises to -1.6°C in February (Fig. 4.2 a) when most of the sea ice has melted and surface waters are heated by increased solar radiation.

From the southwestern continental shelf a large part of HSSW drains southward into the Ross Ice Shelf cavity, while the rest flows north along the Victoria Land coast towards the continental shelf break. Ice Shelf Water (ISW) found on the continental shelf has salinities around 34.7, i.e. is clearly formed through the interaction of HSSW with the ice shelf base, and minimum temperatures reach down to -2.2°C (Fig. 4.2a & b), values which agree well with the observations (Jacobs & Giulivi 1998, Gouretski 1999). Waters in the cavity cluster around the melting line determined by the characteristics of the source water and the pressure dependence of the freezing point for seawater at the ice shelf base. Some warm Antarctic Surface Water enters the cavity near the surface. After it is cooled and freshened by contact with the ice shelf base, mixing with water in the cavity derived from HSSW leads to linear features subparallel to the surface

freezing point line apparent in the September θ/S diagram.
Both HSSW and ISW formed on the Ross Sea continental shelf participate in the formation of Antarctic Bottom Water (AABW), the freshly ventilated water mass occupying the bottom layer in the circum-antarctic deep basins (Carmack 1977, Orsi et al. 1999). AABW found in the South East Pacific Basin is warmer and saltier than its counterpart in the Weddell Sea, which is generally accepted to be the main contributor to the production of AABW. This difference is due to the highly saline parent shelf water masses and the intrusion of warm salty CDW as newly formed bottom water sinks down along the continental slope (Carmack & Foster 1975, Foldvik et al. 1985, Grosfeld et al. 2001). As HSSW descends the continental shelf break in the north-western Ross Sea, it mixes with CDW and forms High Salinity Bottom Water (HSBW) with salinities $\geq$ 34.7 (Jacobs et al. 1970, Gouretski 1999). A significant part of HSBW flows westward along the coast into the Australian Antarctic Basin, while the rest continues northward in the South-East Pacific Basin. A core of ISW extends to the continental shelf break in the central and eastern Ross Sea and forms the parent for Low Salinity Bottom Water (LSBW) which is the bottom water type that mainly fills the abyss of the South-East Pacific Basin (Jacobs et al. 1985, Gouretski 1999).
In the model, AABW temperatures do not reach far below 0° and salinities fall slightly short of 34.7. Since water masses on the continental shelf do reach realistic salinities and temperatures, this shortcoming is due to a misrepresentation of mixing processes at the continental shelf break. Recent research indicates that HSSW decends down the continental slope as small-scale, high velocity plumes (A. Gordon, personal communication). Since these processes are non-hydrostatic and sub-grid scale to the model, they cannot be represented realistically by BRIOS2.2 which instead overestimates mixing between HSSW and CDW at the continental shelf break.

4.2 Circulation pattern

4.2.1 The Ross Gyre

Similar to the Weddell Sea a cyclonic gyre known as the Ross Gyre occupies the deep basin off the Ross Sea continental shelf (Fig. 4.3). In BRIOS2.2 the Ross Gyre also shows a double-cell structure like the Weddell Gyre (Beckmann et al. 1999). However, rather than having two cells of approximately equal transport,

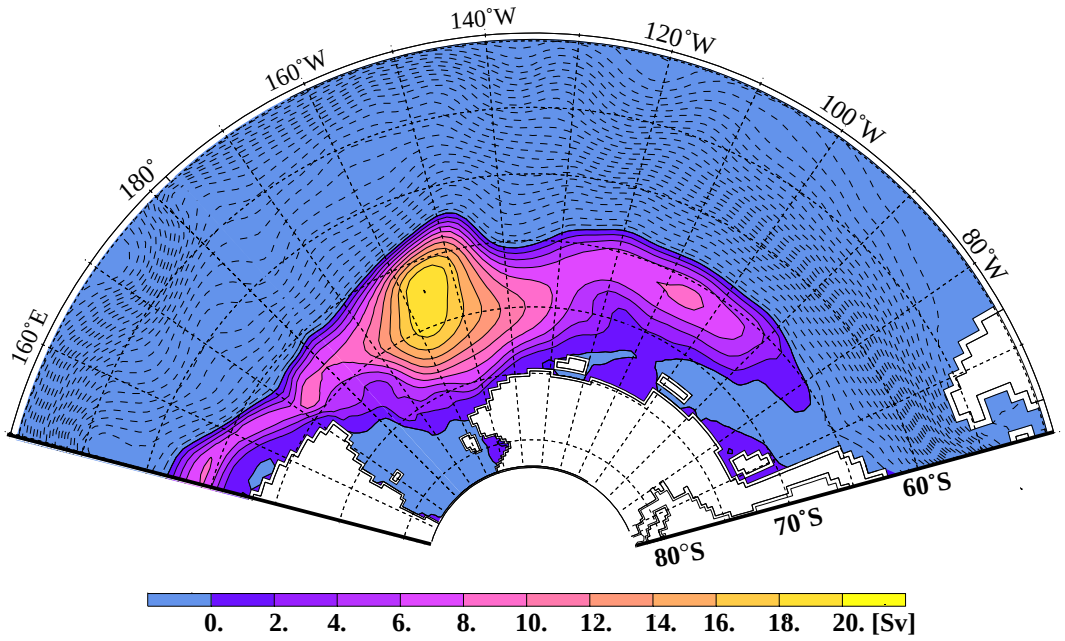

Figure 4.3: Vertically integrated transport from BRIOS2.2 in the Pacific sector of the Southern Ocean. 24-year mean of the barotropic stream function ψ. Isolines for negative values are dashed with a contour interval of 5 Sv, solid ones for positive values have a contour interval of 2 Sv and are colour-coded.

the western cell of the Ross Gyre with a maximum of ∼20 Sv is twice as strong as its eastern counterpart (9 Sv). Comparison to the bottom topography (Fig. 1.1) shows that both gyres are subject to strong topographic steering (Whitworth et al. 1998). In the Atlantic sector the America-Antarctic and Southwest Indian Ridges prevent the ACC from turning southwards and shelter the eastern cell of the Weddell Gyre (Whitworth et al. 1998). In the Pacific sector, however, no such topographic protection exists east of 140°W where the ACC is steered southward through fracture zones in the Pacific-Antarctic Ridge which forms the northwestern boundary of the gyre. As described in the previous section, this intrusion leads to the presence of relatively warm CDW much further south in the Southeast Pacific than in the Weddell Sea and to the asymmetry in transport strength of the gyre's cells. Henceforth, the western cell will be referred to as the Ross Gyre and the eastern as the Ross Gyre extension.

While the western end of the gyre is clearly defined by the Balleny Island plateau at 170°E (Botnikov 1989, Gouretski 1999), opinions about the location of the eastern boundary vary ranging from 125°W (Reid 1986, Botnikov 1989) to 140°W

(Locarnini 1994, Gouretski 1999). The model identifies 130°W as the eastern boundary for the main, western cell in the model, while strictly the Antarctic Peninsula would have to be regarded as the gyre's eastern boundary in agreement with inferences from observations by Locarnini (1994).
Geostrophic volume transports published for the Ross Gyre are 8.5 Sv along 150°W (Gouretski 1998) and 5-9 Sv along 170°W (Locarnini 1994). Neither of these sections cuts through the centre of the main gyre cell shown by the model at 154°W, 67.5°S, a location which agrees with that suggested by Gouretski (1999). The modelled maximum gyre transport is ∼20 Sv, a value which includes both the baroclinic and barotropic parts of the transport. Together with the values for the baroclinic transport calculated from observed density distributions given above this indicates that about half of the gyre transport is wind-driven and barotropic.
Seasonal variability of the Ross Gyre transport in phase with the wind speed (Fig. 4.4) confirms the existence of a substantial wind-driven component of the gyre circulation. Both transport and wind strength show a bimodal distribution with maxima in autumn (March and April) and winter (August). While the wind peaks are of equal strength, the winter peak in the transport is reduced due to the damping effect of the sea ice cover. The bimodal seasonal wind cycle is due to the meridional shift of the circumpolar air pressure trough associated with the semi-annual oscillation (van Loon, 1967).

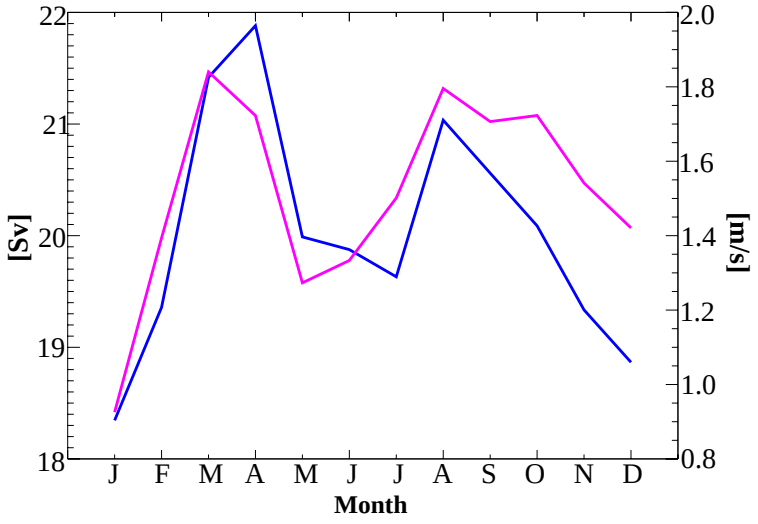

Figure 4.4: Mean annual cycle of the Ross Gyre transport (blue line) and of the mean wind speed over the western cell from NCEP reanalyses (magenta line).

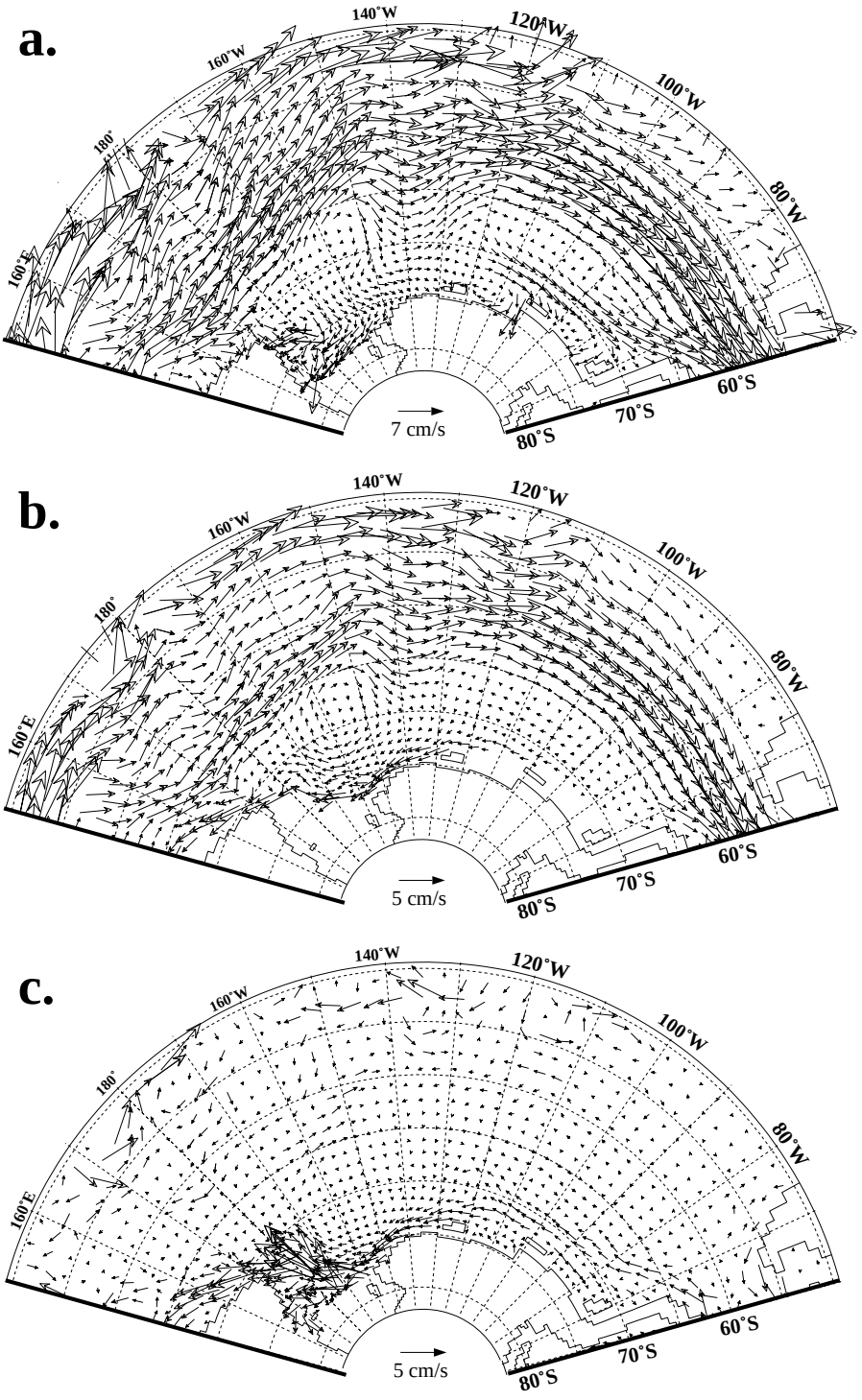

Figure 4.5: Modelled mean horizontal velocity distribution (1978-2001) in **a.** the surface layer, **b.** at 1000 m depth and **c.** the bottom layer. Vectors are shown for every second model grid point. Blank areas are due to regions covered by ice shelves and with bottom depth < 1000m in **b**.

The near-surface current pattern is subject to a strong wind influence. The use of daily changing winds as atmospheric forcing instead of long-term means leads to larger current fluctuations due to the inclusion of, e.g., synoptic variability, thus obscuring the gyre structure in a long-term mean of the surface current pattern (Fig. 4.5 a). At 1000 m depth the gyre structure can be clearly seen, since currents at this depth are no longer affected by synoptic variability of the winds (Fig. 4.5 b). The thick perennial sea ice cover in the Amundsen and Bellingshausen Seas reduces the wind influence on the ocean surface leading to low velocities in the coastal current (Fig. 4.5 c) as found in both model and observations (Whitworth et al. 1998, Hohmann et al. 2002). Coastal current velocities increase considerably upon reaching the Ross Sea, much of which is ice-free or covered by thin sea ice during summer. Near-surface cores of eastward flow close to the continental shelf break can be seen both in the eastern Ross and Bellingshausen Seas (Fig. 4.5 a). The reason for both can be found in the cancellation of the barotropic, wind-driven component of the coastal current by an eastward, baroclinic component induced by the density gradient between shelf and open ocean waters. In the Bellingshausen Sea this is possible because of the weak wind influence, while in the Ross Sea highly dense shelf waters set up a density gradient strong enough to support a counter current, which will henceforth be referred to as the Southern Ross Sea Counter Current (SRSCC). In the Amundsen and Bellingshausen Seas warm CDW is carried westward with the relatively weak (2-4 cm/s) bottom-intensified coastal current (Fig. 4.5 c). CDW also flows south along the eastern limb of the Ross Gyre ($\sim$ 140°W) at mid-depth (Fig. 4.5 b). Near the bottom most waters progress westward from the Ross Sea continental shelf into the South Indian basin, while a weaker flow follows the Pacific-Antarctic Ridge northeastward into the South-East Pacific basin (Fig. 4.5 c).

4.2.2 Ross Sea continental shelf

The most striking feature of the horizontal circulation on the continental shelf is the bottom-intensified westward slope current (Fig. 4.6). In the bottom layer, modelled velocities in this current are about 7 cm s^{-1} in a north-northwestward direction. This compares well with a value of 9 cm s^{-1} observed close to the bottom near the continental shelf break (Picco et al. 1999).

In the surface layer the coastal current splits at 175°W to follow either the ice

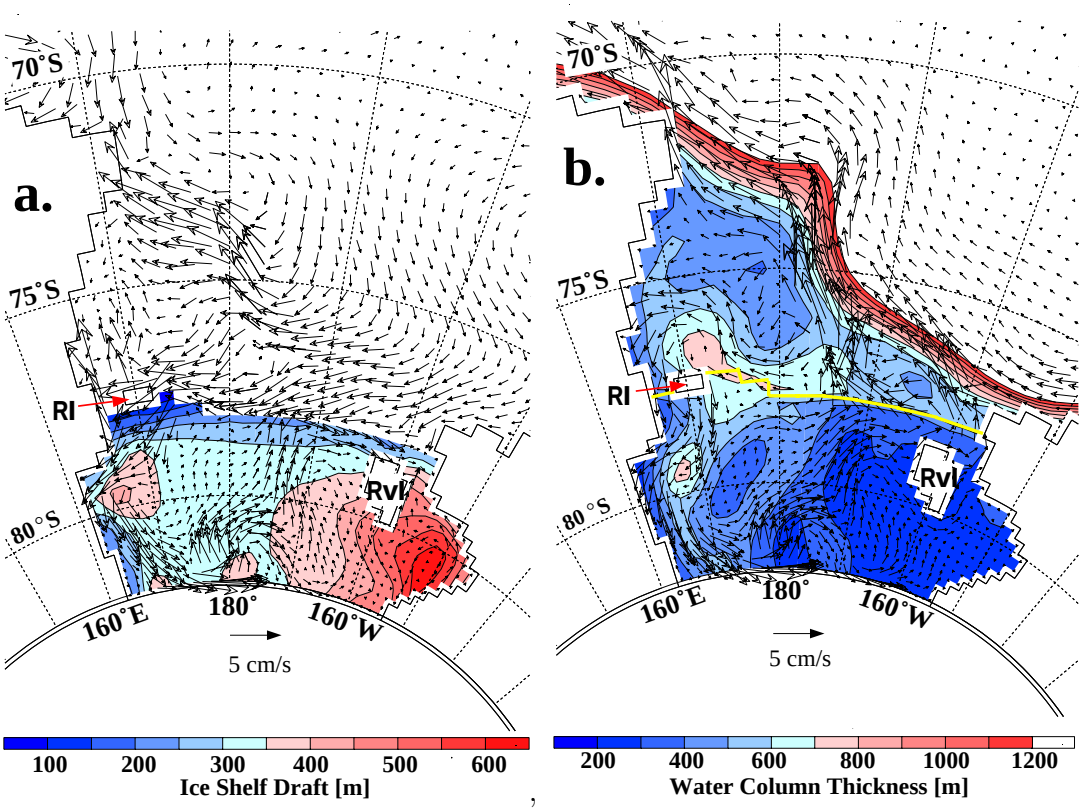

Figure 4.6: 24-year mean horizontal circulation pattern in the Ross Sea. The thick yellow line marks the position of the ice shelf edge: **a.** Surface Circulation. Velocities (vectors) at the ocean surface in the open ocean and in the layer closest to the ice shelf base in the ice shelf cavity and ice shelf draft (colour coded). **b.** Bottom circulation. Velocities in the lowest model layer (vectors) and water column thickness (colour coded). RI = Ross Island, RvI = Roosevelt Island.

shelf edge up to Ross Island as observed by Pillsbury & Jacobs (1985) and Keys et al. (1990), or the continental shelf break (Fig. 4.6 a). At the bottom and at mid-depth on the western shelf the flow is guided topographically entering the cavity through McMurdo Sound (Fig. 4.6 b), in agreement with observations (Lewis & Perkin 1985) and the circulation pattern suggested by Locarnini (1994), joining an anticyclonic circulation cell that extends underneath the ice shelf all the way to the southern model boundary (Fig. 4.6 b). In the upper ocean, the main flow into the ice shelf cavity is located east of Ross Island. Velocities are directed more to the west in the surface layer outside the ice shelf cavity than in the bottom layer due to wind influence (Fig. 4.6 a).

In the ice shelf cavity, the anticyclonic circulation is largely confined to the area of

large water column thicknesses west of 175°W. While current velocities of about 3-4 cm s^{-1} can be found along this main path, they do not exceed 1.5 cm s^{-1} in the eastern cavity. As described by Hellmer & Jacobs (1995), another weak anticyclonic circulation cell can be discerned near the bottom around Roosevelt Island (Fig. 4.6 b). Simulated ISW leaves the cavity through two pathways: one in the central Ross Sea and one east of Roosevelt Island. Both are in agreement with Jacobs et al. (1970), while the central outflow, located at 173°W, also coincides with the ISW observations by Pillsbury & Jacobs (1985) and Picco et al. (1999). However, in the model this outflow is very weak since the main current follows the sub-ice topography to the east just south of the ice shelf front (Fig. 4.6). This is caused by a model resolution (40 km at the ice shelf front) too coarse to represent the meridional ridges in this area. The northwestward directed outflow east of Roosevelt Island agrees well with observations (Hellmer & Jacobs 1995, Rock 1995), though the model slightly underestimates bottom velocities with 6 cm s^{-1} compared to an observed 9 cm s^{-1} (Rock 1995).

4.3 Seasonal cycle on the Ross Sea continental shelf

The summer waters on the Ross Sea continental shelf are among the best sampled around Antarctica. This is due to the fact that the Ross Sea is ice-free during summer and hence conditions are logistically convenient to conduct oceanographic measurements. However, very little data are available in winter and from underneath the Ross Ice Shelf. But it is during this time and in this location that water masses are modified and formed resulting in products that have the potential to become Antarctic Bottom Water. The relevant water masses are High Salinity Shelf Water (HSSW) formed in the southwestern Ross Sea during winter due to extensive brine release in the Ross Sea Polynya (Zwally et al. 1985 , Jacobs & Giulivi 1998) and Ice Shelf Water (ISW) as a product of interaction with the deep Ross Ice Shelf base (Jacobs et al. 1985). Since the seasonal cycle and especially the winter processes on the Ross Sea continental shelf deserve closer attention, a more detailed investigation is presented in this section.

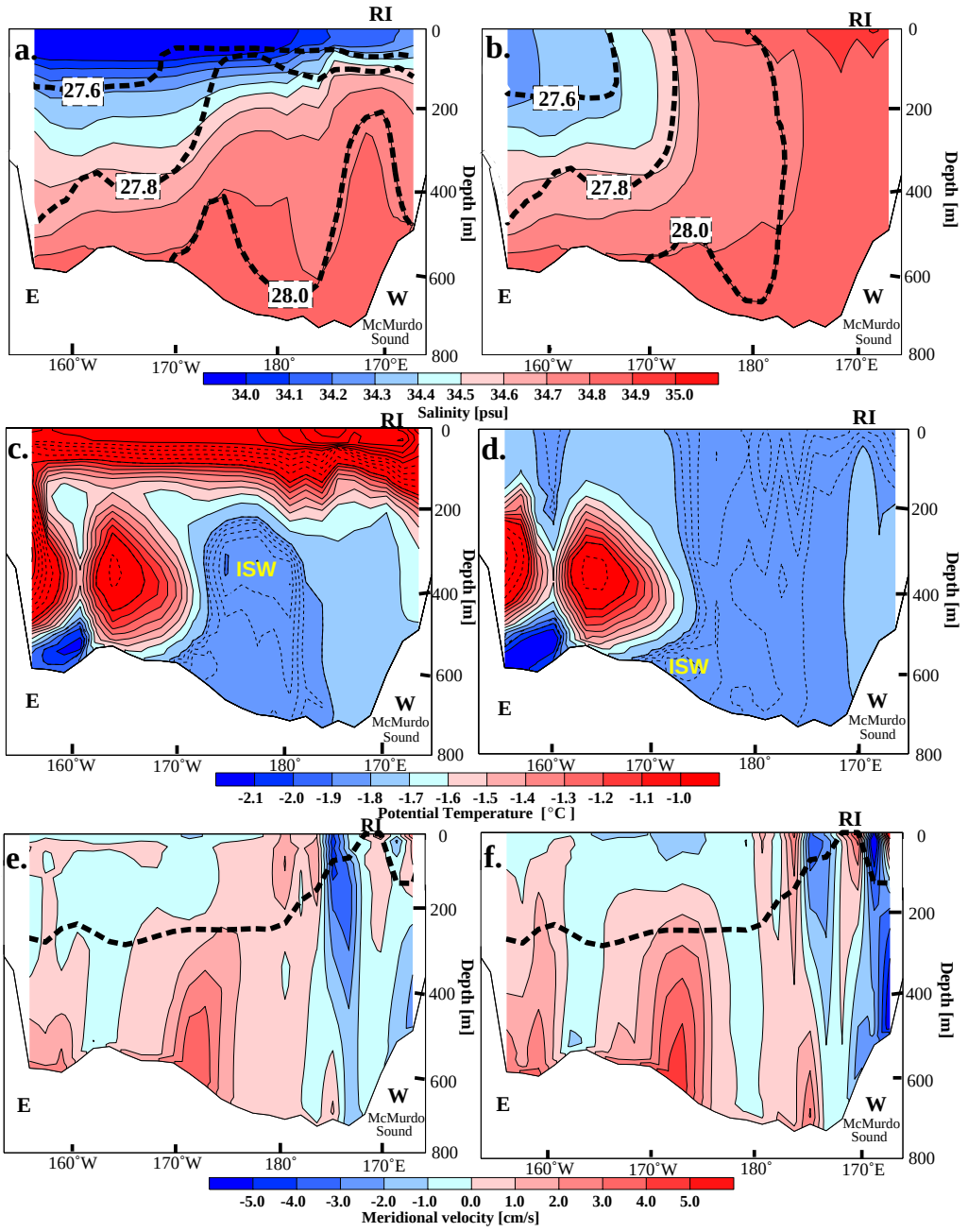

Figure 4.7: Modelled sections along the Ross Ice Shelf edge, facing south, for salinity (colour coded) and density (thick, dashed contour lines): **a.** Summer (February). **b.** Winter (September). Potential temperature: **c.** Summer (February). **d.** Winter (September). Addditional isotherms are marked by dashed contours every 0.2°C for Θ > -1.0°C and 0.02°C for -1.8°C > Θ > -2.0°C. Meridional velocities: **e.** Summer (February). **f.** Winter (September). Positive (negative) values denote northward (southward) velocities. The ice shelf draft (Greischar et al. 1992) is marked by the thick, black, dashed line. Shown are 24-year (1978-2001) means for the relevant months. RI = Ross Island.

4.3.1 Water mass distribution and horizontal circulation

The summer salinity structure along the ice shelf edge displays the characteristic distribution of predominantly LSSW in the eastern and HSSW in the western Ross Sea (Fig. 4.7 a). The density gradient caused by this salinity structure supports the anticyclonic circulation described in the previous section and which is clearly visible in Fig. 4.8. A drastic steepening of the isohalines (and isopycnals) occurs in winter because of enhanced sea ice growth in the Ross Sea polynya (Fig. 4.7 b). Through deep convection the released brine raises the salinity on the western shelf to a value > 34.8, almost constant over the entire water column. This enhanced horizontal density gradient increases the circulation strength of the anticyclonic cell from 1.1 Sv in March to 2.4 Sv in November (Fig. 4.9). This agrees well with the notion that this circulation is strongly controlled by the thermohaline structure on the shelf (Pillsbury & Jacobs 1985).

The smoothed model topography does not permit the development of the observed in- and outflow pattern along the central part of the Ross Ice Shelf edge (Pillsbury & Jacobs 1985). Instead, weakly modified HSSW is advected into the eastern Ross Sea along the ice shelf edge within the cavity (Fig. 4.6). It exits the cavity with the outflow east of Roosevelt Island (Fig. 4.7 a & b) as part of a single anticyclonic circulation cell. This is consistent with the idea proposed by Locarnini (1994) that two separate anticyclonic circulation cells on the Ross Sea continental shelf are needed to preserve the observed horizontal salinity gradient along the bottom. Therefore, a more accurate representation of Ross Sea topography in the model due to higher resolution is likely to further improve our results.

As a result of the eastward diversion within the cavity, the central outflow of ISW (Fig. 4.7 c & d) is weaker and warmer by -0.2°C than observed (Jacobs & Giulivi 1998). Found at 400 m depth in summer, the outflow core is displaced close to the bottom in winter due to strong vertical movement as a result of deep convection. A core of warm MCDW reaches the ice shelf front in the eastern Ross Sea (Fig. 4.7 c & d). It does not penetrate deeply into the cavity but returns almost immediately (Fig. 4.7 e & f) as described by Pillsbury & Jacobs (1985) and Keys et al. (1990). The maximum temperature of -0.8°C is slightly higher than measured (Jacobs & Giulivi 1998) due to an overestimation of the CDW intrusion onto the continental shelf which is narrower than in reality due to topography smoothing in the model.

The vertically integrated transport clearly shows the anticyclonic circulation cell described in Section 4.2.1 that (Fig. 4.8). This pattern does not change in the eastern Ross Sea and in most of the cavity throughout the year only in the transport of the circulation cell varies, but more substantial temporal and spatial changes occur around Ross Island.

By August, the water column has homogenised at salinities between 34.8 and 34.9 from Ross Island to the Victoria Land coast (Fig. 4.7 b). Through McMurdo Sound HSSW flows south into the cavity over most of the water column (Fig. 4.7 f). Due to the increase in the zonal density gradient, the strength of the anticyclonic circulation cell increases to 2.1 Sv, i.e., almost to maximum strength. A northward current of low-salinity water exists all winter along the western slope of McMurdo Sound carrying glacial meltwater out of the cavity (Fig. 4.7 f) agreeing well with winter observations (Barry & Dayton 1988).

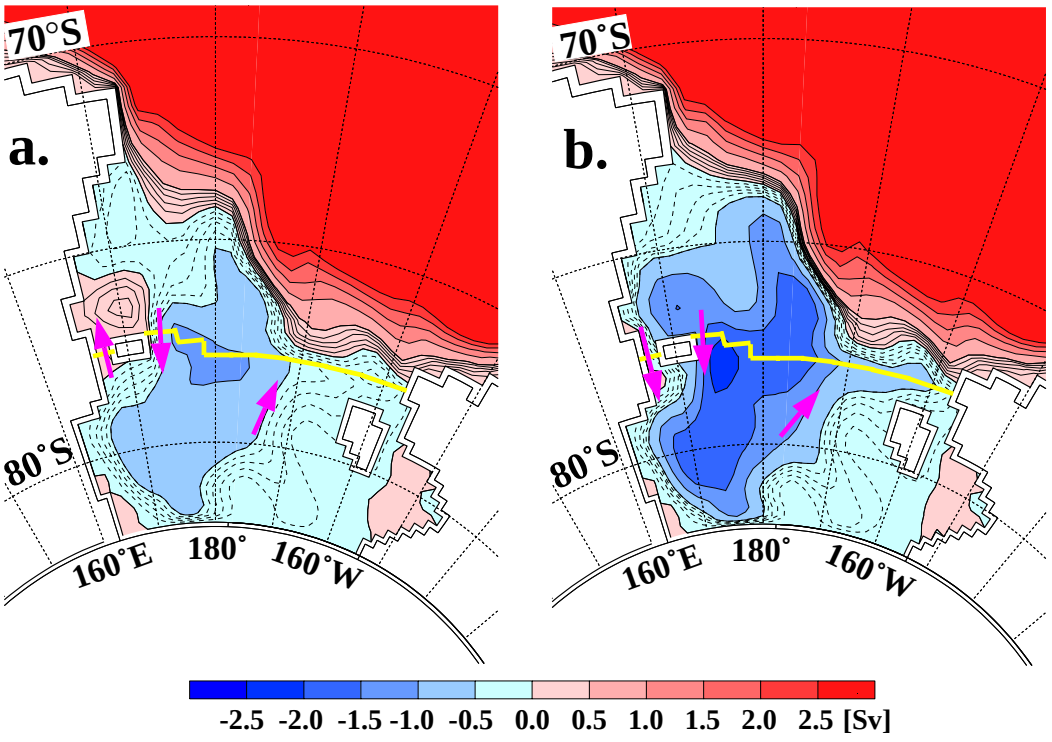

Figure 4.8: Seasonal variation of the vertically integrated transport (24-year mean for 1978-2001). Shown is the vertically integrated transport stream function: **a.** At minimum strength (March). **b.** At maximum strength (October). Solid contour lines/positive values denote cyclonic circulation, dashed contour lines/negative values anticyclonic circulation.

Towards the end of winter, the brine input to the water column in the western Ross Sea starts to decrease. By November, the meltwater flow through McMurdo Sound has been sufficient to erode most of the HSSW near Victoria Land, reversing the zonal density gradient. This in turn increases the northward current due to a positive feedback. Together with the input of freshwater due to sea ice melting this process leaves a dome of HSSW at about 170°E (Jacobs & Giulivi 1998) as seen in summer salinity sections (Fig. 4.7 a). During the summer months the minimum depth reached by the top of the dome, here defined as the minimum depth reached by the 34.8 psu isohaline, increases from 100 m in December to 350 m in April.

The minimum strength of the anticyclonic circulation cell in March and April (1.2 Sv) coincides with the period at which freshwater input due to the melting of sea ice and ice shelf has reduced the horizontal density gradient along the ice shelf edge to its minimum value (Fig. 4.7 a). Supported by southeasterly winds acting on the ocean surface unperturbed by sea ice in summer the near-surface inflow east of Ross Island reaches its maximum strength. This inflow carries near-surface waters into the ice shelf cavity, only slightly blocked by the shallow ice shelf draft of about 80 m (Fig. 4.7 e & f).

A resulting positive meridional density gradient between inflow and Ross Island induces a westward current that transports low-salinity water towards McMurdo Sound along the southern periphery of Ross Island. In the far southwestern corner of the Ross Sea, sea ice growth has already commenced again, but the resulting brine release is not yet strong enough to trigger deep convection. Therefore, outflow through McMurdo Sound continues to alter the density structure until the water column homogenizes due to the onset of deep convection. The vertically integrated transport of the cyclonic circulation around Ross Island amounts to 0.4 Sv (Fig. 4.8 a).

4.3.2 Melting and freezing at the Ross Ice Shelf base

The modelled mean basal melt rate for the entire Ross ice shelf cavity from 1978 to 2001 is 41 cm a^{-1}. Since previous estimates of the average basal melt rate only include the inner ice shelf cavity and exclude melting near the ice shelf front (Jacobs et al. 1979, Jacobs et al. 1992), the first row of grid boxes defined as ice shelf were not taken into account to calculate a comparable value from the model results. Hence, modelled average melting for the inner Ross Ice Shelf cavity is 22

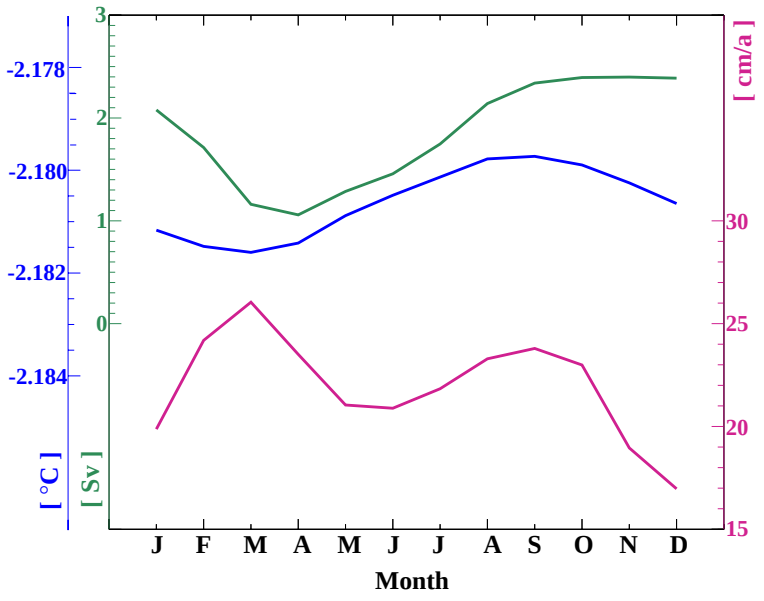

Figure 4.9: Seasonal cycles of the monthly mean maximum transport of the main anticyclonic circulation cell on the Ross Sea continental shelf as shown in Fig. 4.8 (green line, near left scale), ice shelf basal melt rate for the inner cavity (red line, right scale), and averaged potential temperature in the uppermost model layer in the inner cavity (blue line, far left scale).

cm a^{-1} which agrees well with values previously published, 25 cm a^{-1} (Jacobs et al. 1979) and 22 cm a^{-1} (Jacobs et al. 1992). A bimodal seasonal cycle exists in the inner cavity with maxima in March and August and minima in May and December (Fig. 4.9). Melting along the ice shelf front occurs at a mean rate of 187 cm a^{-1}, which is still less than the 320 cm a^{-1} basal melting at the Ronne Ice Shelf Front estimated by Kohnen (1982).

The March maximum of 26 cm a^{-1} is caused by warm summer surface waters carried into the cavity with the surface-intensified inflow east of Ross Island (Fig. 4.7 c & e). This enhances melting south of Ross Island, where basal melt rates exceed 100 cm a^{-1} (Fig. 4.10). Bamber & Bentley (1994) deduced the presence of rapid basal melting in this region from satellite altimeter observations. Modelled basal melt rates in the rest of the inner cavity do not exceed 20 cm a^{-1}, so that the melting south of Ross Island represents a considerable proportion of the total basal mass flux. The thin ice shelf draft near the edge (Fig. 4.7 e & f) east of Ross Island may result in part from this warm near-surface inflow. When in September the transport of the anticyclonic circulation cell is above 90 % of

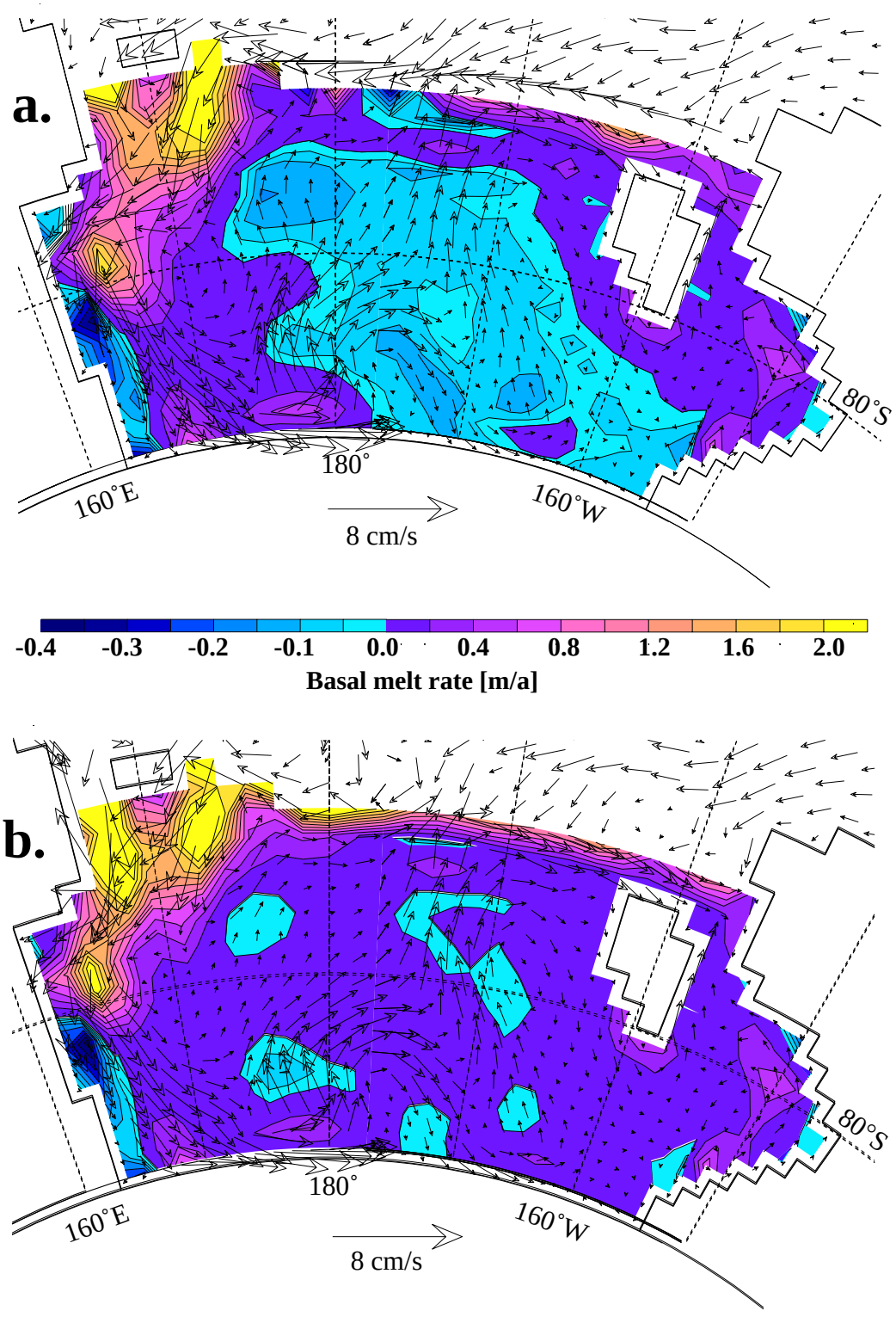

Figure 4.10: 24-year mean (1978-2001) distribution of basal melt rates beneath the Ross Ice Shelf (negative values denote freezing) and velocities in the uppermost model layer (vectors): **a.** December. **b.** August.

its maximum value, increased cavity ventilation results in a second maximum of melting of 23.8 cm a^{-1} (Fig. 4.9). For the May/June minimum of 21.0 cm a^{-1} neither of these mechanisms apply: the surface waters on the continental shelf have already cooled down and circulation strength is still comparatively low.
After October the mean temperature of the water in contact with the inner ice shelf base drops (Fig. 4.9), since cold winter waters have reached this part of the cavity. With less potential heat for melting the water soon becomes in situ supercooled as it rises from the southwestern corner towards the centre of the cavity. Therefore, starting in Decmber, freezing occurs over a large area in the central Ross Ice shelf cavity (Fig. 4.10 a) During most of the year, basal freezing only occurs in patches at a mean rate of 2.5 cm a^{-1} (Fig. 4.10 b). Previous estimates of basal freezing rates range from 2 cm a^{-1} (Zotikov et al. 1980) to 3.5 cm a^{-1} (Jacobs et al. 1979). Between November and February, however, the rate of basal freezing increases to 7 cm a^{-1} in the model's central cavity, causing the second minimum of net basal melting of 17.0 cm a^{-1} for December (Fig. 4.9).

4.3.3 Regional fresh-water budget

The fresh-water budget on the Ross Sea continental shelf is dominated by the flux due to sea ice growth and melting (Fig. 4.11). The annual mean fresh-water export due to sea ice transport off the continental shelf is equivalent to 26.6 mSv (1 mSv = 10^3 m^3 s^{-1}), similar in magnitude to the value calculated for the inner Weddell Sea (Timmermann et al. 2001). Since the area defined by Timmermann et al. (2001) is considerably larger than that of the Ross Sea continental shelf, this emphasizes the exceptionally vigorous sea ice production in the southern Ross Sea. Ice shelf melting and net precipitation contribute less with similar amounts of 4.6 mSv and 4.0 mSv, respectively. Since the southernmost part of the ice shelf cavity is not included in the model, the fresh-water flux due to ice shelf melting might be too small. However, the only direct measurement in that region, based on an ice core, revealed weak basal freezing (Zotikov et al. 1980), indicating that this part of the cavity is not likely to add a large amount of melt water to the overall fresh water budget.
The fresh-water fluxes from ice shelf melting and net precipitation do not balance the fresh-water extracted by sea ice production resulting in an annual mean fresh water export of 18 mSv from the Ross Sea continental shelf. Fresh-water imported by the coastal current along the southern edge of the Ross Gyre compensates the

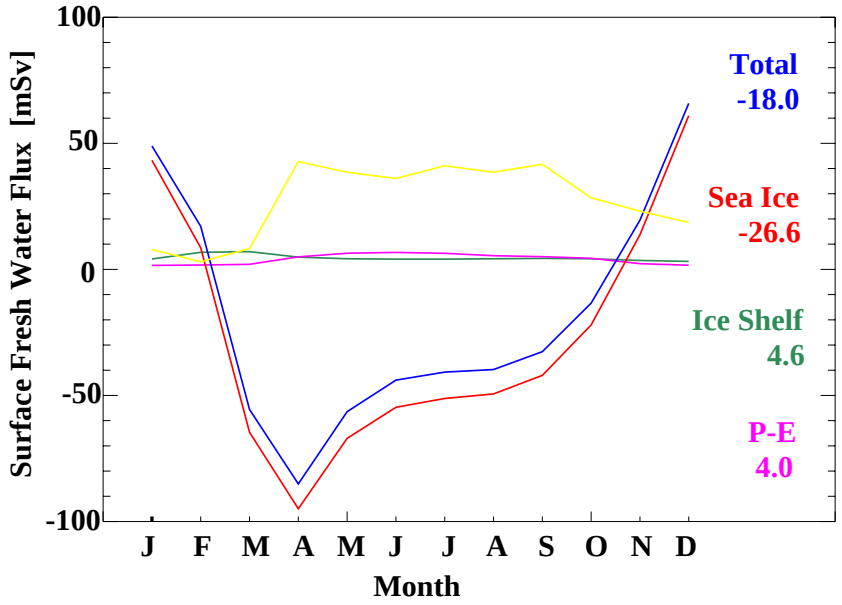

Figure 4.11: Mean annual cycle of monthly mean surface fresh-water fluxes from sea ice formation (red line), basal melting of the Ross Ice Shelf (green line), net precipitation (magenta line), and the overall surface fresh water flux for the Ross Sea continental shelf (blue line). Also shown is the sea ice transport off the Ross Sea continental shelf (yellow line). The annual means of the fresh-water fluxes due to sea ice formation (red) and export (yellow) are equal in magnitude but opposite in sign. 1 mSv = 10^3 m^3 s^{-1}.

fresh-water extraction due to sea ice formation and export. The interannual variability of sea ice export and oceanic fresh-water import, and their influence on shelf water salinities will be investigated in more detail in Chapter 6.

4.4 The effect of McMurdo Sound topography on water mass exchange across the Ross Ice Shelf front

As shown in the previous section, the McMurdo Sound region is an important area for the circulation and dense water formation in the southwestern Ross Sea and their variability throughout the year. A point of debate has been whether the topography of McMurdo Sound permits exchange with the cavity and if so which effect this might have. Following the acquisition of new information about the cavity configuration in the Ross Island and McMurdo Sound area (U. Nixdorf,

personal communication) the analysis of circulation and water mass distribution on the Ross Sea continental shelf in the previous chapter was extended to explore the sensitivity to various topographies of McMurdo Sound.
For atmospheric forcing, daily NCEP Reanalyses from 1978-1987 were used as spin-up time and the mean annual cycle of the years 1988-1997 was used for analysis.[3] Comparisons were drawn between the standard model landmask configuration for McMurdo Sound (Fig. 4.12 a) and two modified topographies. First, McMurdo Sound was narrowed by the introduction of the peninsula known as Minna Bluff (Fig. 4.12 b) and second, it was closed off completely (Fig. 4.12 c).

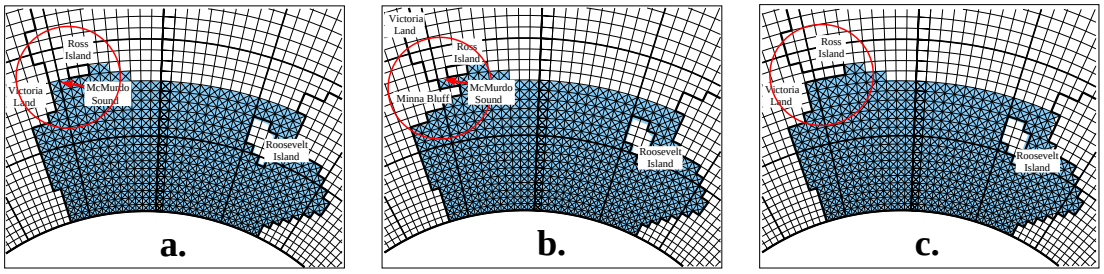

Figure 4.12: Model landmasks used for sensitivity studies: **a.** Standard run, **b.** Minna Bluff, **c.** No Sound.

The typical salinity structure along the ice shelf edge of predominantly Low Salinity Shelf Water (LSSW) in the eastern and High Salinity Shelf Water (HSSW) in the western Ross Sea (Jacobs & Giulivi 1998) is preserved in all three sensitivity experiments (Fig. 4.13). This reflects the strong gradient in sea ice growth rates along the ice shelf front with high growth rates in the polynya area and is hence unaffected by the change in landmask.
However, observations (Barry & Dayton 1988) and model results show that a northward current of low-salinity water exists all winter in the western McMurdo Sound carrying glacial meltwater out of the cavity. This near surface outflow from the cavity through McMurdo Sound seen in the reference experiment seems to be necessary to lower salinities in the western Ross Sea sufficiently for the observed dome of HSSW near 170°E (Jacobs & Giulivi 1998) to appear. With progressive closure of McMurdo Sound the isohalines, e.g. the 34.8 line, on the western side of the dome start to level out due to the suppression of the fresh-water flow (Fig. 4.13 b-c). Narrowing McMurdo Sound also prevents the drainage of HSSW along the bottom in winter leading to enhanced HSSW salinities in the western

[3]This shorter period was chosen due to time constraints.

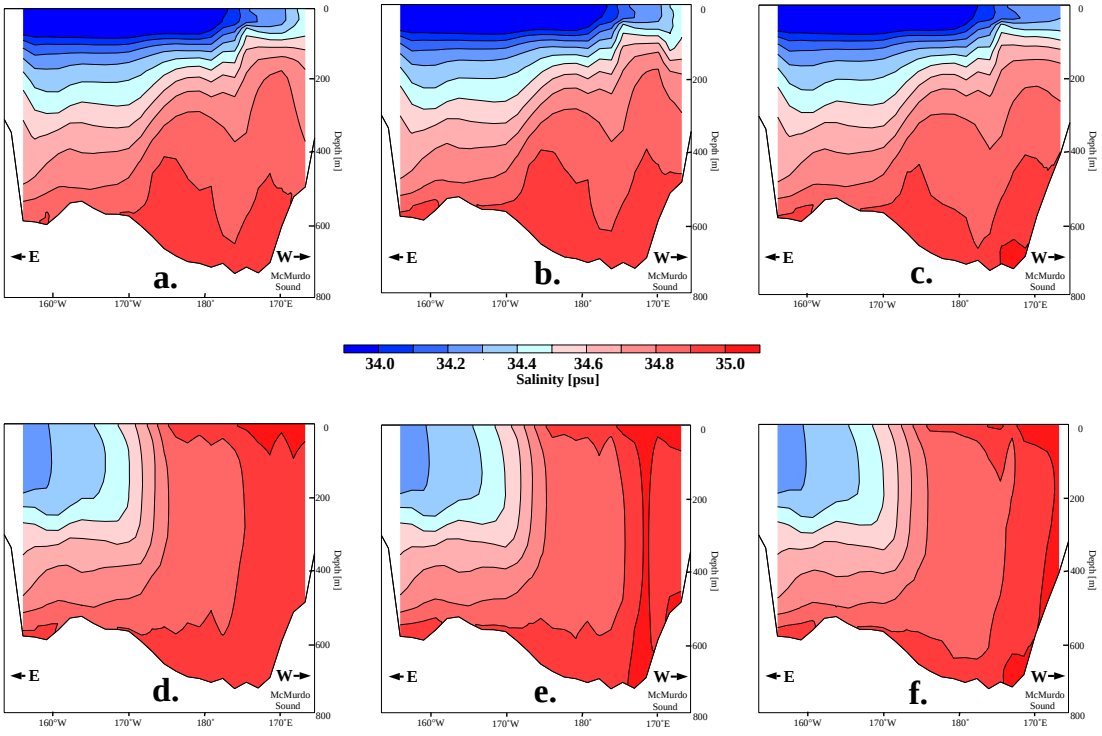

Figure 4.13: Salinity section (10-year mean) along the Ross Ice Shelf Edge, facing south. Top row: Summer (February). Bottom row: Winter (September). **a.** & **d.** Reference simulation, **b.** & **e.** Minna Bluff, **c.** & **f.** No Sound.

Ross Sea (Fig. 4.13 e-f). However, the changes in HSSW salinities induced by the alteration of McMurdo sound topography prove to be smaller than the interannual variability of the model displayed over the 10-year period considered.

In summer, when the main cavity inflow is located near the surface east of Ross Island, closing McMurdo Sound does not have much of an effect on the circulation pattern (Fig. 4.14 a-c). In winter, however, HSSW mainly drains south into the cavity over the whole water column in the reference experiment (Fig. 4.14 d). In the "Minna Bluff" experiment there is less southward flow through McMurdo Sound, which is compensated by increased near-surface inflow east of Ross Island (Fig. 4.14 e). For McMurdo Sound closed, the picture remains much as in summer, only with a large area of weak southward flow appearing around 180° (Fig. 4.14 f). The peak strength of the anticyclonic circulation cell does not reflect the substantial changes in inflow location in winter (Fig. 4.15). This finding supports the hypothesis by Pillsbury & Jacobs (1985) that the horizontal circulation on the Ross Sea continental shelf is predominantly thermohaline driven. The zonal

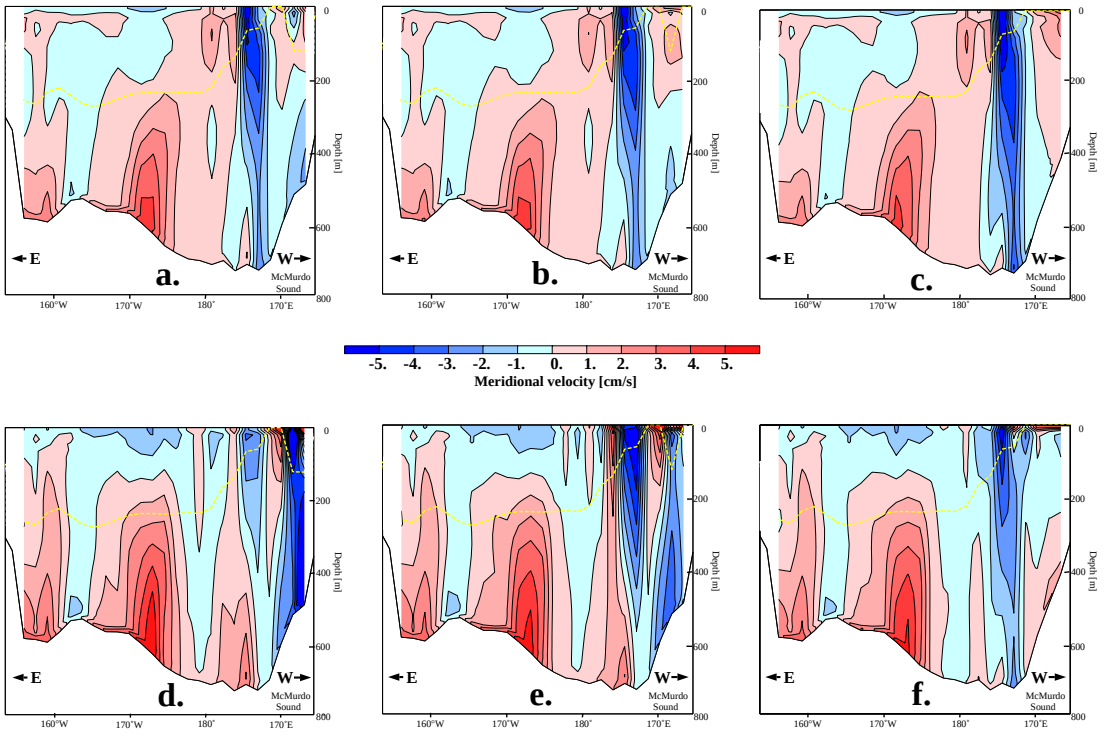

Figure 4.14: Meridional velocity section (10-year mean) along the Ross Ice Shelf Edge, facing south. Top row: Summer (February). Bottom row: Winter (September). **a.**& **d.** Reference simulation, **b.** & **e.** Minna Bluff, **c.** & **f.** No Sound. Positive values denote northward velocities, negative southwards. The ice shelf draft is marked by the thick, yellow, dashed line.

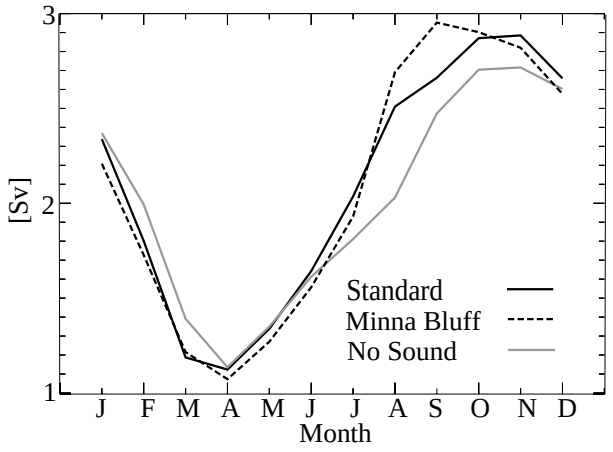

Figure 4.15: Seasonal cycle of the maximum transport of the main anticyclonic circulation cell on the Ross Sea continental shelf for the different McMurdo sound topographies.

	Standard	Minna Bluff	No Sound
Cavity [ma^{-1}]	0.276	0.261	0.256
[mSv]	3.28	3.06	3.05
Edge [ma^{-1}]	3.28	3.06	3.05
[mSv]	2.39	2.28	2.09
Total [ma^{-1}]	0.45	0.43	0.40
[mSv]	5.67	5.34	5.14
[Gta^{-1}]	178.7±26.5	168.6±23.6	162.3±20.8

Table 4.1: Mean basal melt rates and fresh water fluxes for standard and sensitivity runs. Edge denotes the mean over the front row of grid boxes defined as ice shelf, cavity the mean over the rest.

salinity gradient and its winter steepening which control the circulation strength are preserved in all three runs. The change of McMurdo Sound topography hence causes a change in inflow location, but does not change the maximum transport of the anticyclonic circulation cell on the Ross Sea continental shelf.

In the inner cavity, the bimodal seasonal cycle of the basal melting rate with maxima in March and August and minima in May and December (cf. Fig. 4.9) is preserved for all three experiments. The "Minna Bluff" and "No Sound" experiments show lower melt rates during winter, when strong basal melting occurs south of McMurdo Sound in the standard run, due to the shift in inflow location. Overall, this leads to a 5% reduction in the basal melt rate for the inner cavity which supplies about 60% of the total fresh water flux from the cavity (Table 4.1). Closing McMurdo Sound leads to a lowering of the total basal mass flux in the cavity by about 10 %. Again, this change is smaller than that caused by interannual variability.

The November temperature section along the Ross Ice Shelf front shows two central cores of Ice Shelf Water (ISW), one at $\sim$ 200m depth and the second near the bottom (Fig. 4.16 a). We will concentrate on these two central cores, rather than the much colder one seen to emerge east of Roosevelt Island, since they are much more likely to be affected by changes around McMurdo Sound due to the existence of separate circulation regimes in the eastern and western parts of the cavity (Locarnini 1994). Also, the central ISW core is thought to participate in the formation of Low Salinity Bottom Water (Jacobs 1970), as it consists mainly

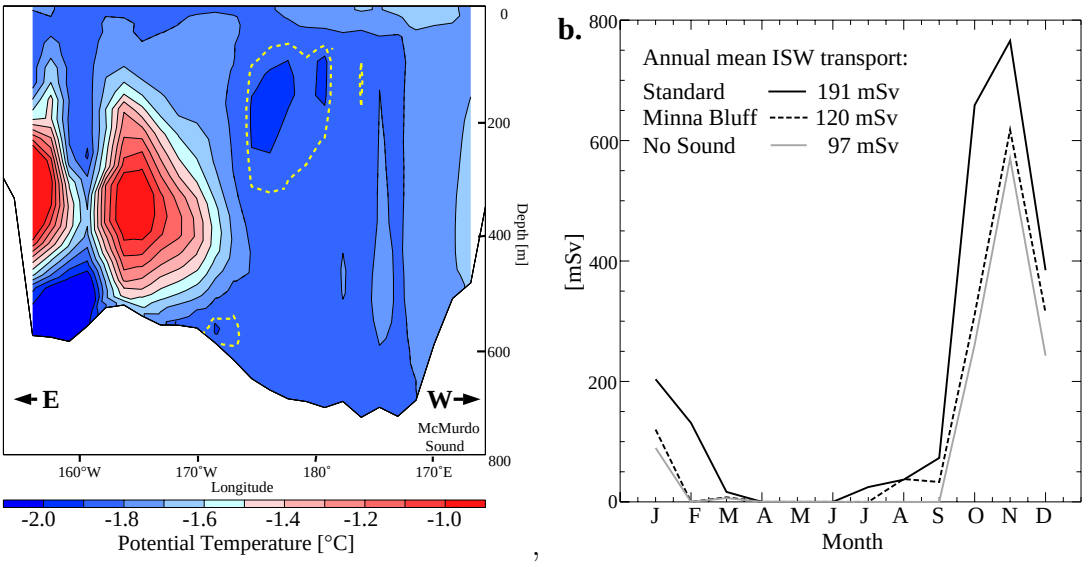

Figure 4.16: Ice Shelf Water (ISW) outflow from the Ross Ice Shelf cavity: **a.** Potential temperature section along the Ross Ice Shelf front, November mean (1988-1997). The dashed yellow line represents the -1.88° isotherm to mark the ISW outflow. **b.** ISW transport across the Ross Ice Shelf front, central core.

of HSSW modified through interaction with the ice shelf base, and is consequently saline and dense enough. Since the ISW outflow is underestimated in the model, -1.88°C was defined as the upper temperature limit for ISW.

The March to June minimum of the ISW outflow (Fig. 4.16 b) can be attributed to the presence of a strong westward wind-driven current along the ice shelf front. In addition, deep convection and the associated destruction of the stratification during the sea ice growth season erode the ISW plume as it exits the cavity. At the November maximum, the water column has started to regain a stable stratification at the onset of summer melting along with a sea ice cover still present which reduces the wind influence. This enables ISW to leave the cavity at a rate of about 0.75 Sv.

Closing McMurdo Sound results in a 50% reduction of the ISW emerging from the cavity in the annual mean and a 33 % reduction of the November peak (Fig. 4.16 b). This is rather large in comparison to the changes seen in other variables, especially since the overall circulation strength is almost unaffected (Fig. 4.15). Earlier, the seasonal shift of the main cavity inflow westward to McMurdo Sound in the standard run was pointed out. This shift is another constraint on the ISW flow out of the cavity. In the sensitivity experiments this shift does not occur at

all or only to a lesser degree, while the maximum transport of the thermohaline-driven anticyclonic circulation cell increases just as before. This results in a weak southward flow over a broad area reaching as far east as the location of the ISW cores, the strength of which gets weakened considerably.
This study implies that flow through McMurdo Sound ought to be possible for the observed salinity structure in the southwestern Ross Sea to appear. The influence on the central ISW core suggests that McMurdo Sound appears to fulfil an important function in guiding the spreading of HSSW and in affecting one of the possible sources of AABW in the Ross Sea.

4.5 Summary

Modelled circulation and water mass characteristics of the Pacific Sector of the Southern Ocean were investigated with a particular focus on conditions on the Ross Sea continental shelf. Validation against summer observations shows that the coupled sea ice-ocean model BRIOS2.2 provides a very reasonable representation of the water mass distribution and the circulation in the Ross Sea. The main water mass characteristics are reproduced and the modelled circulation patterns support earlier hypotheses based on observations. In addition, modelled mass fluxes at the ice shelf base show a detailed distribution of melting and freezing regimes with values in the range partly provided by the literature.
Intrusion of warm Circumpolar Deep Water onto the continental shelf in the Amundsen and Bellinghausen Seas as part of a southward extension of the Antarctic Circumpolar Current leads to a Ross Gyre warmer than the Weddell Gyre. A first value for the total Ross Gyre transport of 20 Sv is obtained from the model results along with a double-cell structure of the gyre with, in contrast to the Weddell Gyre, a pronounced asymmetry in transport of the two cells. Modified Circumpolar Deep Water (MCDW) enters the Ross Sea continental shelf at the eastern and central sections of the shelf break. The model shows the shelf circulation to be largely barotropic below the surface layer forming an anticyclonic circulation cell that extends from the shelf break to the southern end of the cavity in the western Ross Sea.
The zonal gradient of sea ice formation is reflected by shelf water salinities, with high growth rates in the western Ross Sea resulting in deep convection and in the formation of High Salinity Shelf Water as the densest water mass in the Southern Ocean. Winter steepening of the isohalines increases the transport of

the anticyclonic circulation cell that occupies the western part of the continental shelf and the ice shelf cavity and enhances the southward drainage of HSSW into the cavity. This confirms the strong thermohaline forcing of the Ross Sea continental shelf circulation by supplementing the summer-biased observations with a detailed picture of winter conditions. More subtle seasonal changes in the circulation pattern occur around Ross Island and through McMurdo Sound.

The model studies presented here identify McMurdo Sound as a key region for the circulation and water mass distribution in the Ross Sea. Freshwater outflow from McMurdo Sound is responsible for the dome structure in the salinity distribution along the ice shelf edge in the western Ross Sea. Drainage of HSSW through McMurdo Sound into the cavity in winter prevents brine accumulation and thus lowers HSSW salinities to the range observed. Prohibition of High Salinity Shelf Water drainage along the Victoria Land coast leads to a weakening of the central Ice Shelf Water outflow, thus affecting the balance of the two sources of Antarctic Bottom Water in the Ross Sea.

As a result of large salt fluxes due to sea ice formation on the western shelf and strong sea ice export from it, the fresh-water budget of the Ross Sea continental shelf is negative. Fresh-water imported by the coastal current compensates for this extraction.

Chapter 5

Sea ice variability in the Pacific sector of the Southern Ocean

5.1 Sea ice drift in the Amundsen Sea - validation and implications

As shown in Chapter 3 the Amundsen Sea continental shelf is covered year-round by an ice pack of considerable thickness making the collection of data difficult or impossible. In this section data gained from three Alfred-Wegener-Institute (AWI) sea ice drift buoys released in this region for the first time will be presented. A comparison to model data provides validation for short temporal and spatial scales and gives insight into the time scales and causes of the short term variability of sea ice drift, and the influence of wind and ocean currents.

5.1.1 Drift data

The sea ice drift buoys with ARGOS identities 9358, 9361, and 9364 were deployed on sea ice floes during a late March 2000 RVIB *Nathaniel B. Palmer* cruise NBP00-01 in the eastern Amundsen Sea (Fig. 5.1). They registered air temperature at 2-m height, air pressure at sea level, and position (GPS) for periods between 242 and 580 days (Table 5.1). Gaps towards the end of the drift of 9364 (Fig. 5.1, black broken lines) are caused by intermittent data transfer presumably after the decay of its ice floe left the buoy floating in rough seas.
The northern pair of buoys (9358 & 9364) deployed near the continental shelf break show a synchronous behavior for most of the drift until the failure of buoy

9358 (Fig. 5.1). The southern buoy (9361) stayed close for one month before drifting westward increasing the gap to 3 - 4 times the initial separation. West of 125°W it drifted parallel to, but north of, the 1995-97 track of iceberg B10b (Fig. 5.1). Transmission of the last position of 9361 near 135°W coincides with the onset of summer melting in late November, probably weakening the ice floe and releasing the buoy into open water. In November 2000, 9358 ceased operating while 9364 moved westward through the summer. Its drift extended beyond the last registered position of 9361, in deep water, and again parallel to the track of iceberg B10b. Near 145°W, 9364 began to move northward, similar to the early voyage of iceberg B10a (Fig. 5.1).

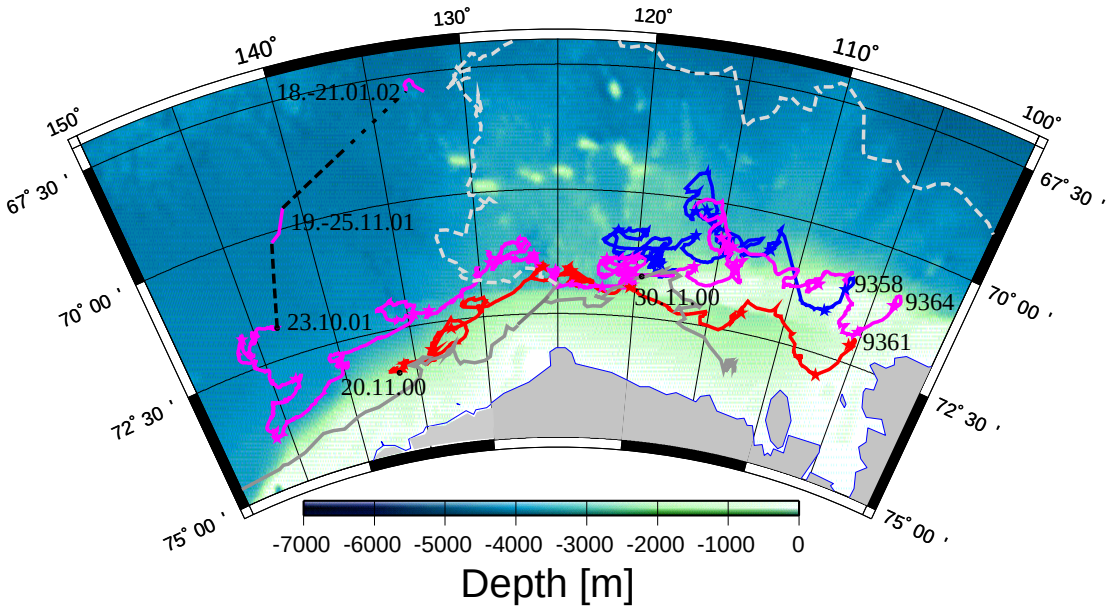

Figure 5.1: Bottom topography (ETOPO 2; available at www.ngdc.noaa.gov/mgg/global), drift tracks of AWI buoys 9358 (blue), 9361 (red), and 9364 (magenta), and icebergs (grey lines) B10 & B10b (solid), and B10a (dashed) in the Amundsen Sea. Coastline coordinates still show iceberg B10 close to its calving site at Thwaites Glacier near 105°W. Colored stars on the buoy tracks indicate the beginning of a new month. Dates mark the end of periods of data transmission (colored solid lines). The drift buoys were deployed between 20 and 23/3/2000.

Several aspects of the sea ice and iceberg drifts are noteworthy. The sea ice buoys all moved westward, with short-term fluctuations superimposed on a general drift along the edge of the continental shelf. The deep-draft icebergs B10, B10a and B10b followed similar tracks after reaching the shelf break (Fig. 5.1, gray lines).

ID	Date	Position	Duration [day]	Distance [km]	Speed [m/s]	u_{mean} [m/s]	v_{mean} [m/s]
9358	03/20/00	71.095°S	252	3320	0.15	-0.017	-0.005
		106.894°W	(207)				
	11/30/00	71.671°S					
		119.641°W					
9361	03/22/00	72.134°S	242	2670	0.12	-0.05	-0.009
		105.558°W	(232)				
	11/20/00	73.385°S					
		136.274°W					
9364	03/23/00	71.076°S	580	7170	0.14	-0.025	-0.001
		103.734°W	(568)				
	01/21/02	67.896°S					
		132.030°W					

Table 5.1: Drift details of AWI buoys 9358, 9361, and 9364. Date and position are provided for start and end of the drift, which defines the duration. Interrupted data transmissions reduced the actual number of days with observations to the numbers given in brackets. The last three columns contain the mean speed and mean zonal and meridional translocation for each buoy.

Iceberg B10a in 1996 (Fig. 5.1, gray dashed line) and buoy 9364 in 2001 (Fig. 5.1, intermittent magenta line) broke this pattern between 130°W and 145°W, tracking northward for several hundred kilometers before reversing direction in the Antarctic Circumpolar Current.
While the mean absolute speeds for all three buoys are similar (Table 5.1), the mean zonal and meridional velocities show pronounced differences, reflecting the drift characteristics. Less variable in the zonal direction, the southern buoy (9361) drifted westward with the highest mean velocity of -0.05 ms^{-1}.

5.1.2 Comparison of observed and modelled buoy tracks and drift velocities

Rather than comparing the modelled Eulerian sea ice drift fields with the observed Lagrangian sea ice buoy data, the drift of buoys was simulated in the model

sea ice velocity field. A model buoy was introduced at the starting point of each observed buoy. Following the approach of Timmermann et al. (2002a), additional model buoys were released at intervals of 30 days at the position of the relevant observed buoy at that date (Fig. 5.2 - 5.4). This approach produces an ensemble of simulated trajectories around the observed tracks. Once the simulated and observed trajectories diverge, of course, the modelled buoy may be forced into a different drift regime and diverge even further from the observed track (Harder and Fischer, 1999). The model buoys are only allowed to drift until they reach open water, since at this point the sea ice momentum balance becomes meaningless. The model buoys released at the March starting point of the observed buoys do not move due to the underestimation of the summer sea ice extent, but viable tracks result from the ones deployed in April. It should also be noted that the observed buoy tracks are located in a small portion of the total model area, only 30 by 10 grid points (of 242 by 65) for the widest-ranging buoy (9364), and the 2.5° x 2.5° grid of the NCEP reanalysis cannot represent features smaller than this grid size. Nevertheless, the modelled drift generally corresponds to the observed drift and will be discussed in more detail below.

Both the observed and modelled buoy 9358 are located in the transition zone of highly variable drift direction (Fig. 5.2 a). While the model buoys introduced after July 2000 (West of 115°W) follow the observed drift fairly closely, the earlier buoys perform a net eastward drift as opposed to the westward one of the observed trajectories. Whether this is due to the wind field or the ocean surface currents will be investigated in the following section. A northward loop appears in the observed buoy tracks as well as the modelled ones between May and July.

The model buoys released along the track of 9361 reflect its westward drift along the coast (Fig. 5.3 a). The simulated tracks are more convoluted than the observed one, fall short of the endpoint of 9361, and are located slightly to its north. The first model buoy, released in April, is carried into the transition zone between easterly and westerly winds. This and the fact that the modelled drift of 9361 is directed less clearly zonally suggests that the change from coastal westerlies to deep ocean easterlies is further south in the NCEP Reanalyses data than in the winds experienced by the buoys.

The observed drift of 9364 (Fig. 5.4 a) is represented fairly well by the model buoys. The northeastward turn in July and August 2001 can be seen clearly in both modelled and observed buoys. However, modelled drifts do not follow the coast as closely as the observed buoy which tracks more to the southwest. An

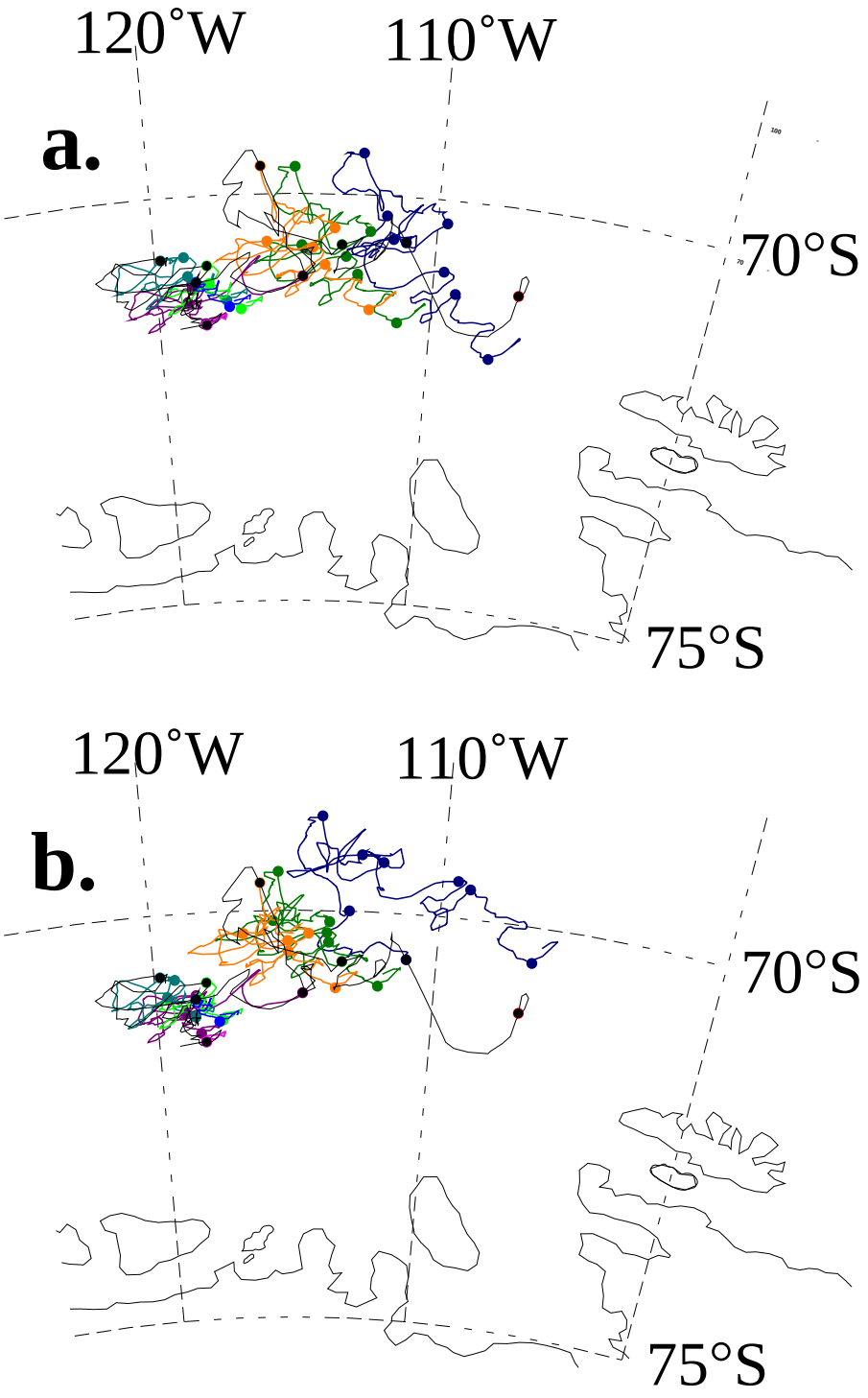

Figure 5.2: Observed (black) and simulated (colour) sea ice drift trajectories for buoy 9358 with (a) and without (b) ocean surface currents. Marks are set every 30 days. Model buoys are released every 30 days (changed colour).

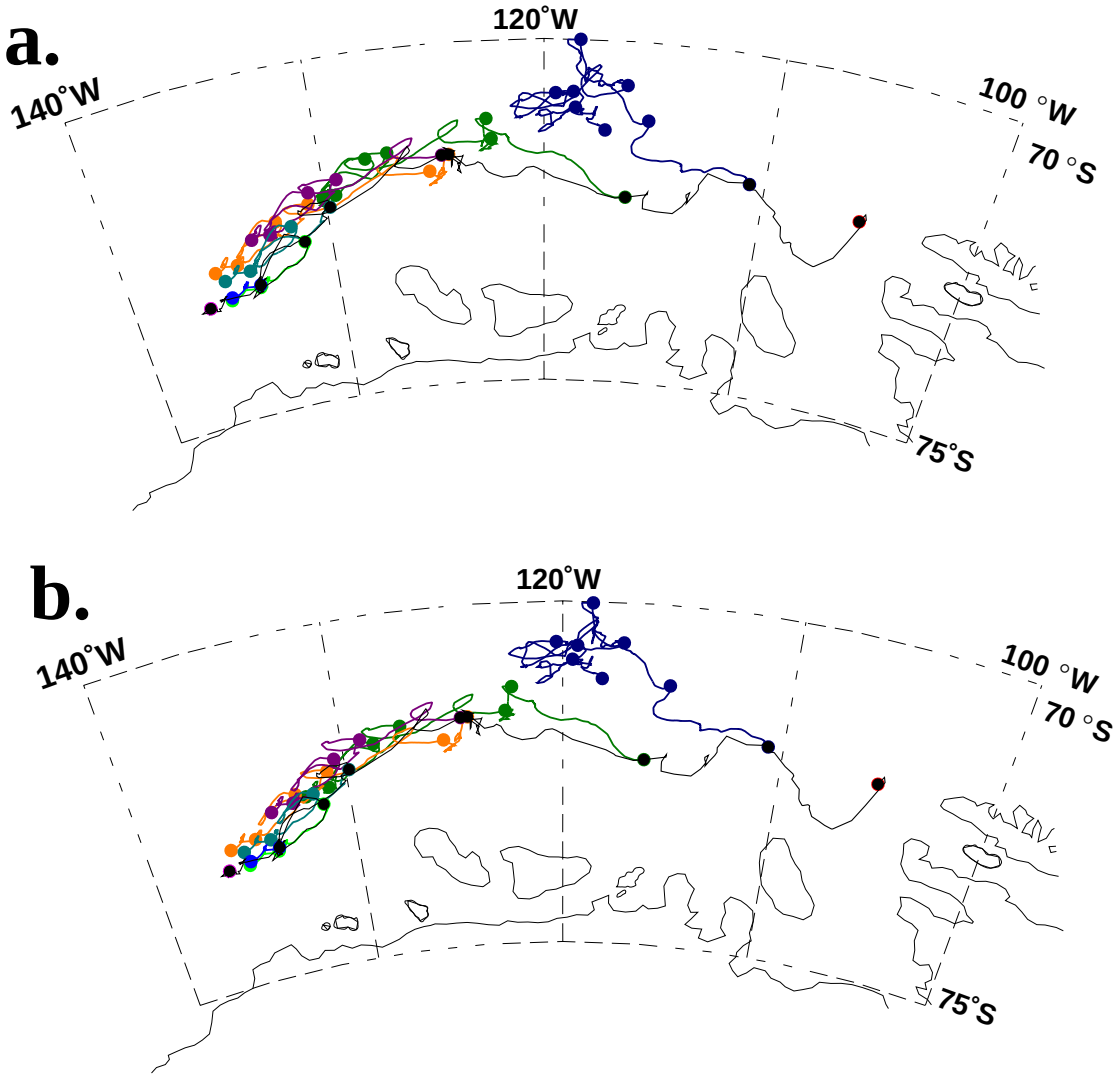

Figure 5.3: Observed (black) and simulated (colour) sea ice drift trajectories for buoy 9361 with (a) and without (b) ocean surface currents. Marks are set every 30 days. Model buoys are released every 30 days (changed colour).

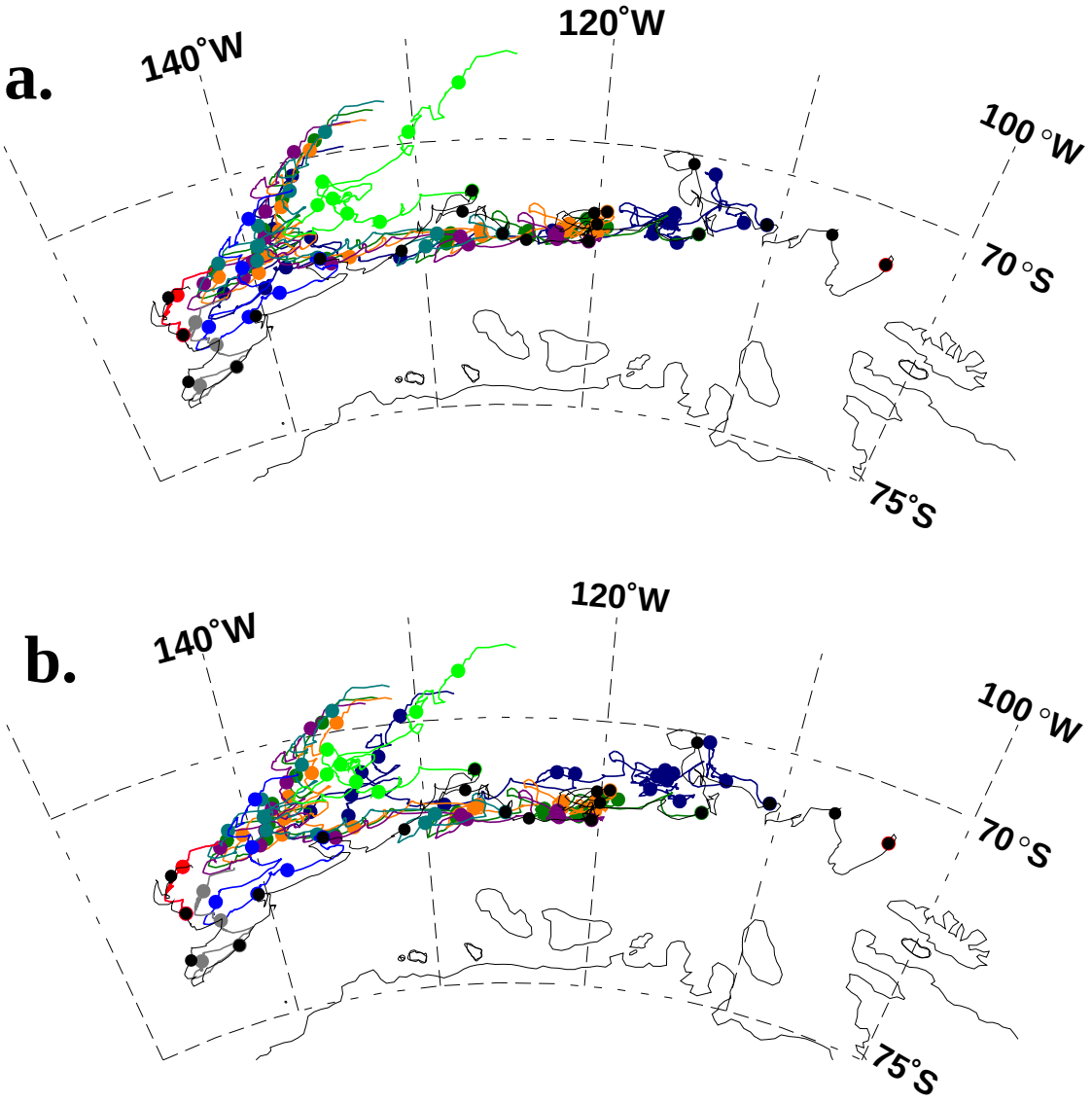

Figure 5.4: Observed (black) and simulated (colour) sea ice drift trajectories for buoy 9364 with (a) and without (b) ocean surface currents. Marks are set every 30 days. Model buoys are released every 30 days (changed colour).

		u-component [m/s]		
ID		**9358**	**9361**	**9364**
Mean	Model	0.010±0.091	-0.037±0.089	-0.010±0.091
	Obs.	-0.020±0.126	-0.050±0.107	-0.025±0.099
	NCEP	-0.94±4.39	-2.59±4.5	-1.13±4.5
RMS	Model	0.091±0.108	0.096±0.121	0.092±0.11
	Obs.	0.127±0.156	0.118±0.147	0.103±0.114
	NCEP	4.48±5.25	5.19±6.09	4.67±5.61

		v-component [m/s]		
ID		**9358**	**9361**	**9364**
Mean	Model	-0.005±0.078	0.006±0.061	0.003±0.065
	Obs.	-0.007±0.110	-0.009±0.080	-0.001±0.087
	NCEP	-0.57±3.3	0.070±3.1	-0.36±2.98
RMS	Model	0.078±0.100	0.062±0.085	0.065±0.088
	Obs.	0.110±0.14	0.088±0.114	0.087±0.114
	NCEP	3.35±3.97	3.09±3.53	3.00±3.73

Table 5.2: Arithmetic mean and root-mean-square of modelled and observed sea ice drift velocity components of AWI buoys 9358, 9361, and 9364, and of the NCEP wind velocity components along their tracks.

underestimation in the NCEP zonal wind velocities is indicated by the fact that neither the simulated buoys for 9361 nor those for 9364 drift as far westward as their observed counterparts.

For a more quantitative comparison the modelled and observed drift velocities were compared along the buoy tracks. The model generally underestimates the magnitude of the rms-velocities[1] by 25% for both u and v (Table 5.2). A possible reason is low NCEP wind speeds, as shown in a comparison of ship-based wind observations with NCEP winds in Appendix B. The positive modelled mean u-component of 9358 reflects the net eastward drift of the modelled buoys, rather than westward as observed. Since winds in the transition zone are highly variable with a comparatively small mean value, even small deviations between NCEP and actual winds can add up to a significantly different net ice drift velocity.

[1]Root-mean-square velocity, defined as $v_{rms} = \sqrt{\frac{1}{n}\sum_{i=1}^{n} v_i^2}$ where v denotes the velocity component to be averaged.

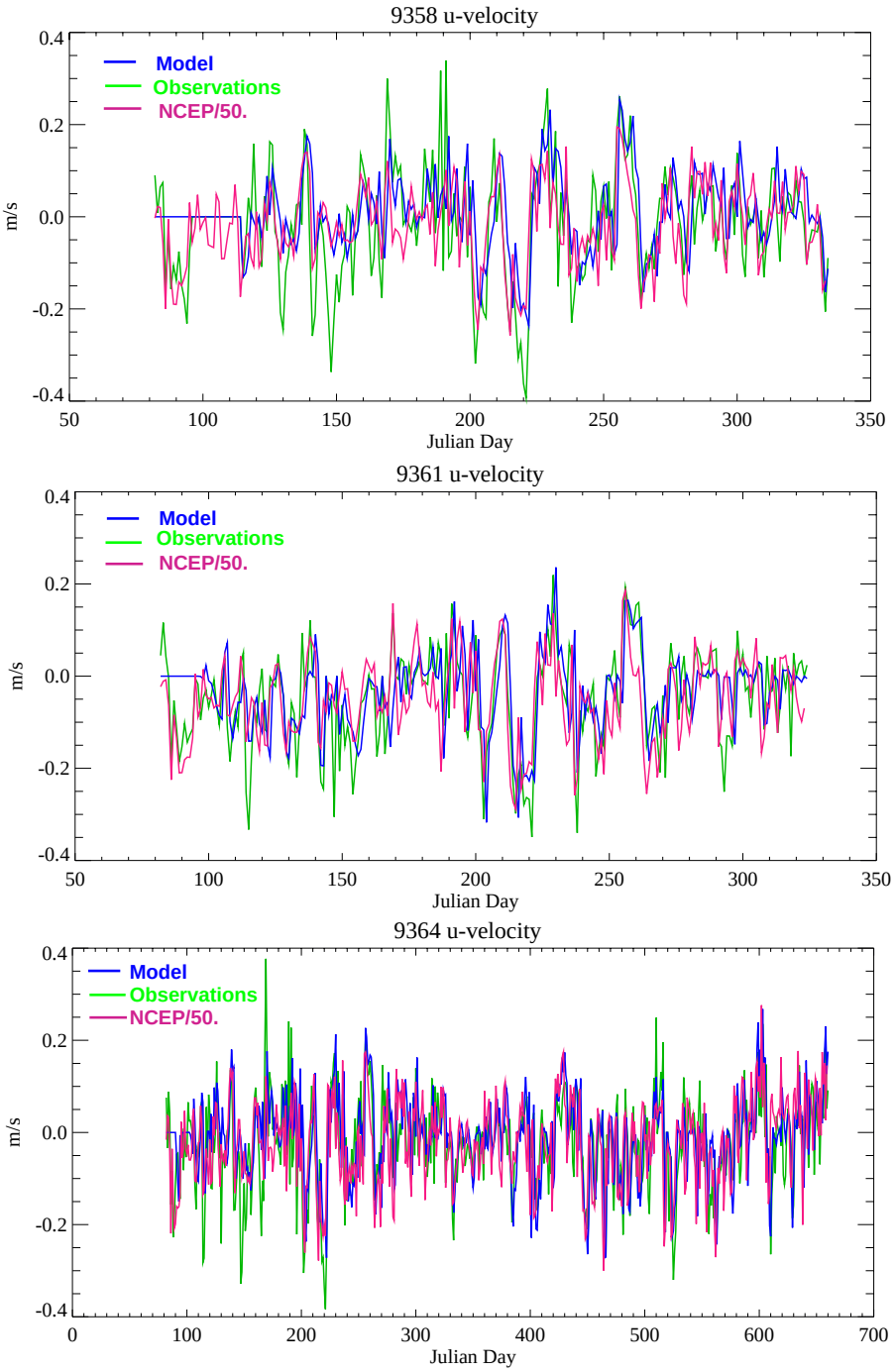

Figure 5.5: Time series of observed (green) and simulated (blue) zonal drift velocity components and NCEP wind velocities (magenta) along the observed buoy tracks. NCEP velocities were divided by 50 to make them comparable in scale to the sea ice drift velocities. Shown here are daily averages for all three series. Buoy numbers are marked above each plot.

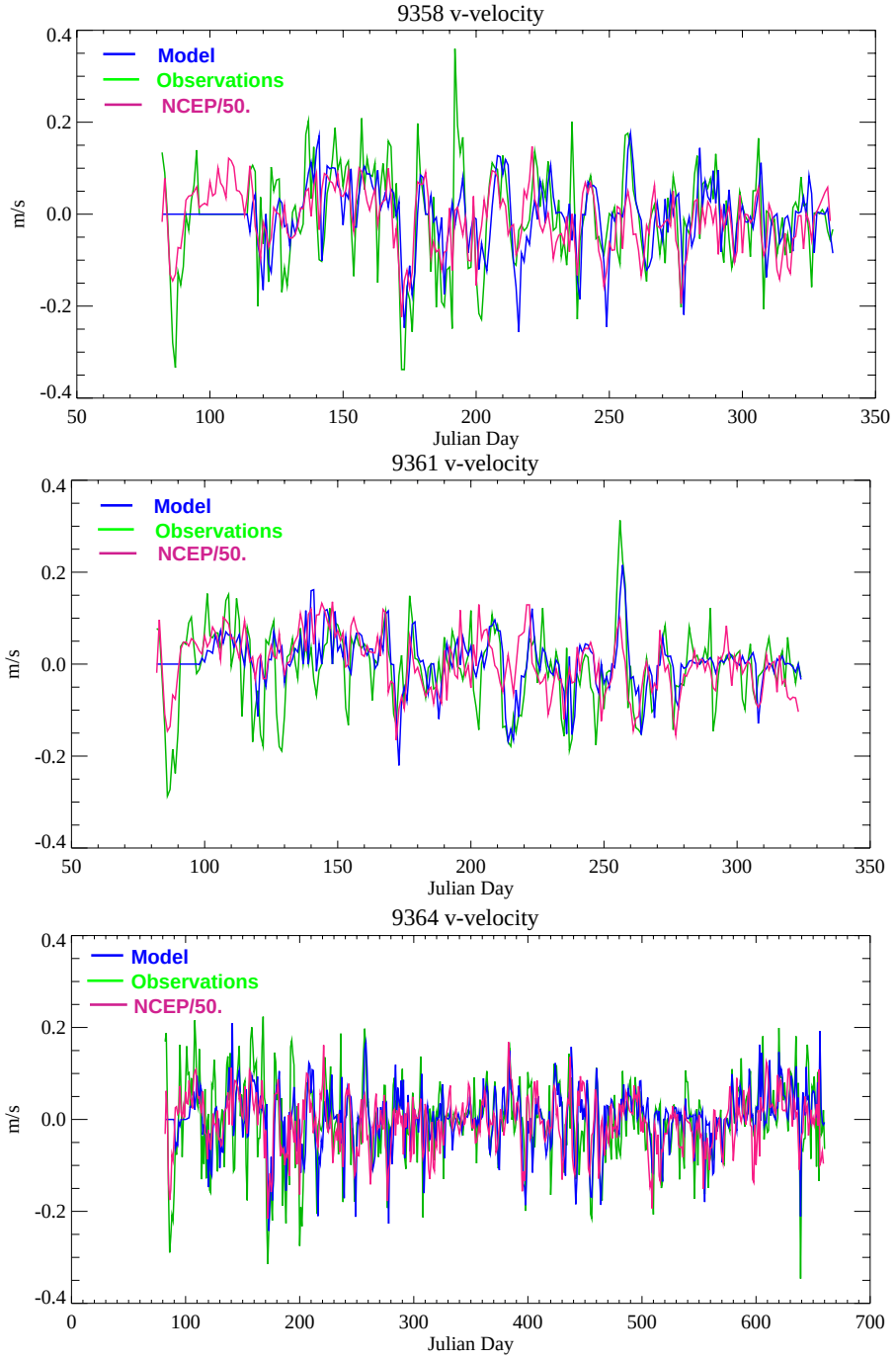

Figure 5.6: Time series of observed (green) and simulated (blue) meridional drift velocity components and NCEP wind velocities (magenta) along the observed buoy tracks. NCEP velocities were divided by 50 to make them comparable in scale to the sea ice drift velocities. Shown here are daily averages for all three series. Buoy numbers are marked above each plot.

Similarly, the modelled 9361 and 9364 buoys show a net northward meridional velocity rather than a slight southward drift as observed. As the meridional drift component is fairly small, major effects do not result from the difference in direction.

Observed sea ice velocities are larger than the simulated ones by 30 - 65 % during high ice velocity events due to the underestimation of wind speed by the NCEP Reanalyses especially during the passage of strong synoptic events, e.g. the peak in the v-component of the observed buoy 9358 at day 190 (Fig. 5.6, also cf. Appendix B). The agreement between modelled and observed velocities appears to be better in winter than in autumn when the modelled ice pack has different internal dynamics caused by the underestimation of the summer sea ice cover.

Comparison of the timeseries of observed and modelled sea ice drift and NCEP wind velocities along the observed tracks shows that most observed events happening on a time scale of several weeks are well matched by the NCEP Reanalyses and hence the model (Fig. 5.5 & 5.6). For free ice drift, sea ice drift speeds are expected to be approximately 2.5 % (Fischer 1995) to 3.0 % (Martinson & Wamser 1990) of the 10m wind speed. Model values are lower between 1.85 % and 2.33 %. Due to uncertainties in the choice of atmospheric and oceanic stress coefficients in the model, ratios above 2 % indicate that the free drift assumption may still be applicable. This is the case for the meridional drift components of all three buoys with ratios between 2.0 % and 2.3 %. For the zonal component, ice drift to wind speed ratios are smaller. A value of 1.85 % for buoy 9361 suggests that zonal ice movement in winter in the Amundsen Sea cannot be described as free drift. Buoys 9358 and 9364 have values of $\sim$ 2.0 % for their zonal component. Inclusion of a summer period in the drift of 9364 and movement within the transition zone of 9358 may have resulted in a movement closer to free drift. These results, however, indicate that the free drift assumption is not applicable for zonal ice drift close to the Amundsen Sea coast in winter. Meridionally, a divergent ice pack allows movement that may be approximated by a free drift scenario.

In an fft-analysis (Fig. 5.7), the NCEP wind series show dominant periods of 16 days for u and 13 days for v, consistently for all three buoy tracks. The u-component exhibits two secondary peaks at 22/23 days and 29/30 days (Fig. 5.7). The latter peak may be due to atmospheric tides, while the 13-16 day peaks are probably due to high-index blocking of cyclones, i.e., of synoptic origin (G. König-Langlo, personal communication). The origin of the 22/23 day peak remains uncertain.

While the relative amplitudes of the peaks differ, the periodograms for the simulated and observed sea ice drifts generally agree for both velocity components with a closer match for buoys 9358 and 9361 than for 9364 (Fig. 5.7). Inclusion of a summer in the 9364 drift means that sub-model grid scale motion becomes more important in the observed ice pack than in winter when a compact ice pack follows a more coherent large-scale drift pattern. Especially in the v-component this leads to the absence of clear peaks above the 95%-significance threshold. In the observations, the 13-day peak of v is considerably stronger than in the model, possibly due to a misrepresentation of the meridional winds in the NCEP data because of their low meridional resolution.

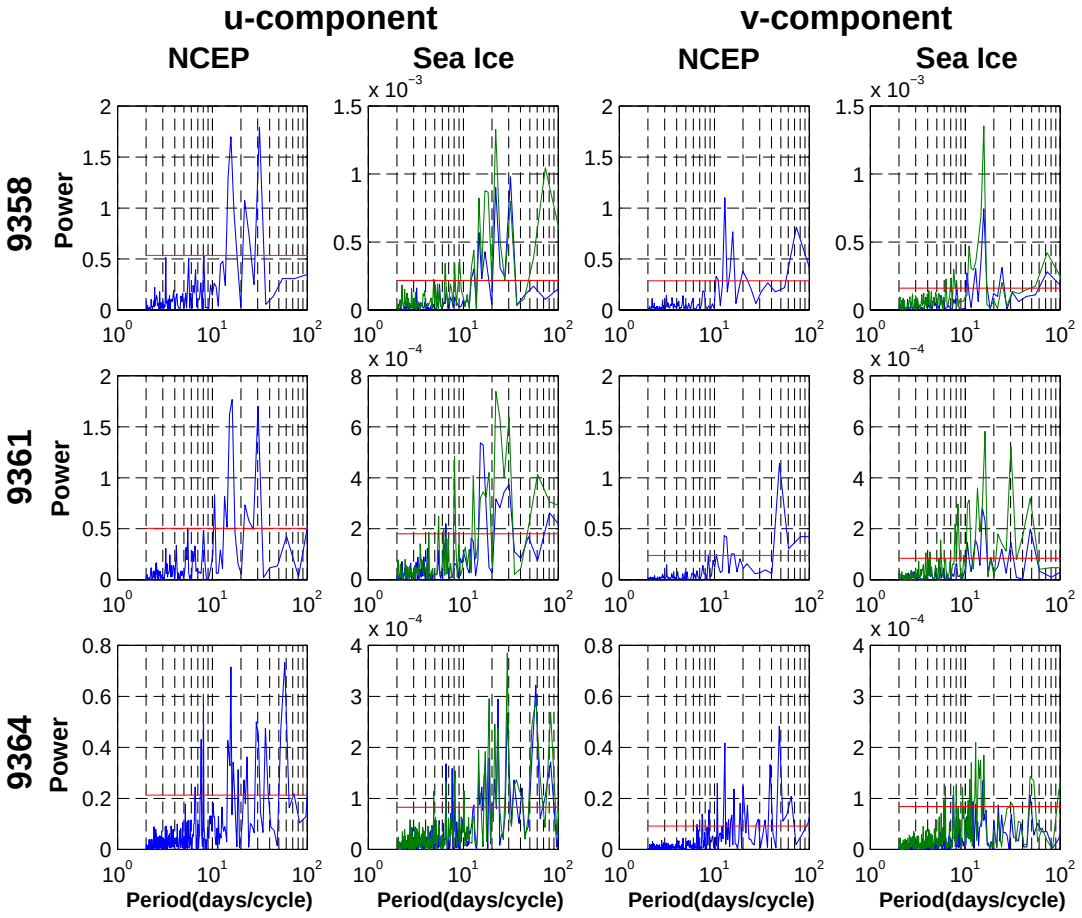

Figure 5.7: Periodogram of the time series of daily averaged velocity components along the observed buoy tracks for NCEP winds and simulated (blue lines) and observed (green lines) sea ice drift velocities. Red lines indicate the 95% significance level.

Semidiurnal and diurnal tidal currents have been identified as an important in-

fluence on sea ice motion in the vicinity of the continental slope in the Weddell Sea (Padman & Kottmeier 2000). When performing an fft-analysis on the initial, hourly observations, this does not seem the case for the Amundsen Sea, which is in agreement with model results that show tidal currents to be weak in the Amundsen Sea (L. Padman, personal communication).
The 13-day peak in the NCEP v-component does not appear strongly in any of the modelled sea ice drift velocities. Instead a dominant frequency can be seen around 15/16 days with additional peaks between 20 and 30 days in the v-component, periods also found in the u-spectra.
For both NCEP data and drift velocities the maximum power of the detected periodic signal in the meridional component is about half that found for the zonal component (Fig. 5.7). This agrees with the notion that the meridional winds and drift velocities are less coherent than their zonal counterparts (Table 5.2).
As already mentioned, principal periods of the zonal wind appear in the meridional drift velocities. The zonal wind component contributes to the meridional ice drift, since the ice drift veers left with respect to the wind direction due to the presence of ocean drag and the Coriolis force (Hunkins 1975). Since in the Amundsen Sea the zonal wind component is stronger and more steady in direction, zonal wind variability strongly impacts the meridional component of the sea ice drift, but the weaker meridional wind variability cannot be found in the zonal drift.

5.1.3 Influence of wind and ocean currents

To evaluate the relative influence of wind and ocean currents on sea ice drift, a sensitivity experiment was conducted in which the sea ice was only driven by wind. With sole wind influence on sea ice, the simulated buoy tracks differ only little from those in the reference run. For 9358, which best represents drift in the transition zone, trajectories are generally shifted to the West and North (Fig. 5.2 b), consistent with the southeastward currents in the surface layer of the ocean model in this region. The largest shift occurs for the April buoy, probably due to a stronger effect of ocean currents in the open autumn ice pack. The May-June loop disappears in the absence of ocean forcing indicating that this feature seems to be caused by the ocean surface currents rather than by a large-scale wind pattern. For 9361, the ocean surface currents cause a very slight northward

shift in the drift along the coast between 120°W and 140°W (Fig. 5.3 b), and for buoy 9364, the ocean influence accelerates its northward drift after the change of direction in winter 2001 (Fig. 5.4 a).
The influence of the Amundsen Sea ocean surface circulation appears to be less important than in the Weddell Sea (Timmermann et al. 2002 a), but can still be felt in the transition zone where wind directions are highly variable. Westward drift close to the coast appears to be almost exclusively wind-driven, consistent with a relatively weak coastal current. Internal dynamics of the ice pack, especially during the growth and decay seasons, both reflect and modulate the dominant influence of wind on sea ice drift in the Amundsen Sea.

5.2 Sea ice transports

Simulated sea ice transport provides a measure of sea ice exchange between different Antarctic marginal seas and the ACC regime and refines the picture given by the large-scale drift. To define the various regions of the South Pacific, boundaries are set at 70°S, 100°W, and 150°W (Fig. 5.8). The latter was chosen rather than 130°W (Gloersen et al. 1992, Jacobs & Comiso 1997), because the drifts of sea ice buoys and icebergs (cf. Section 5.1) indicate that a significant proportion of sea ice is transported north between 130°W and 150°W instead of continuing westward into the Ross Sea.
The closed gyre-type drift in the Bellingshausen Sea (Fig. 3.5), a region of typically perennial ice and sluggish flow, results in fairly large north- and southward components of the meridional sea ice transport ($13.2 \pm 5.4 \times 10^3$ m^3 s^{-1} and $12.3 \pm 4.2 \times 10^3$ m^3 s^{-1}, respectively). This circulation does not allow for much net export which amounts to $2.5 \pm 6.1 \times 10^3$ m^3 s^{-1} to the Amundsen Sea and $0.9 \pm 7.6 \times 10^3$ m^3 s^{-1} northward (Fig. 5.8). Standard deviations much larger than the actual values reflect strong variability of these exports, suggesting that the Bellingshausen Sea is not quite as isolated a region as indicated by the net transports.
From the Amundsen Sea, the modelled annual mean sea ice export across 150°W is $8.4 \pm 8.9 \times 10^3$ m^3 s^{-1} (Fig. 5.8). This transport can be separated into a westward ($18.3 \pm 6.2 \times 10^3$ m^3 s^{-1}) and an eastward ($9.9 \pm 4.9 \times 10^3$ m^3 s^{-1}) component, south and north of the transition zone, respectively (Fig. 3.5). The net meridional export across 70°S of $10.9 \pm 14 \times 10^3$ m^3 s^{-1} can be split into 20.3 $\pm$ 10.4×10^3 m^3 s^{-1} northward and $9.4 \pm 4.7 \times 10^3$ m^3 s^{-1} southward. Rather

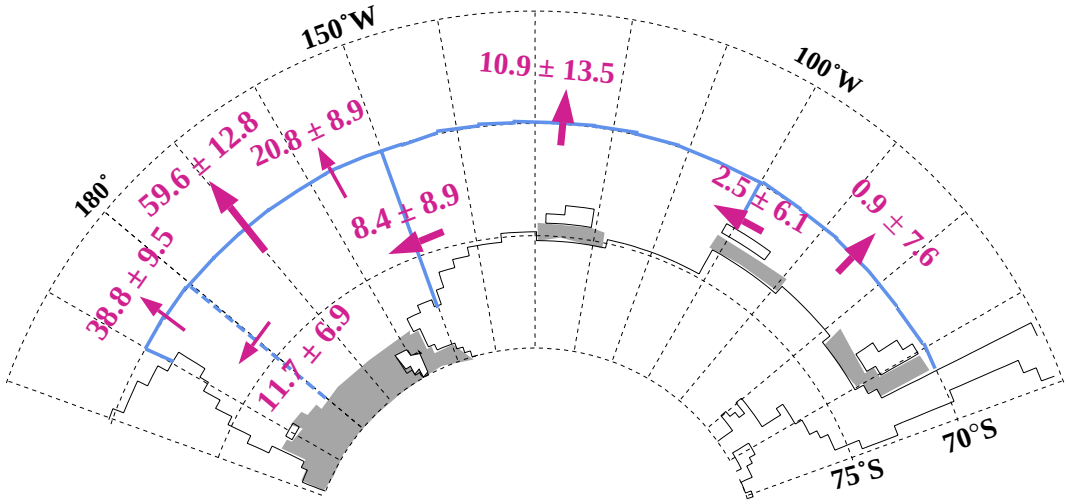

Figure 5.8: Schematic diagram of modelled mean annual sea ice transport (1978-2001) in the South East Pacific. Ice shelves are shaded grey. Units are in 10^3 $m^3 s^{-1}$.

than spatial like for the zonal transport, the split in the meridional transport is temporal and will be described in more detail in Section 5.4. Net westward and northward transports are of similar magnitude, but the former is primarily fed by thick perennial ice close to the coast, and the latter by thinner sea ice north of the transition zone.

The largest and most steady sea ice transport by far is the northward export out of the Ross Sea amounting to a mean of 59.6 ± 12.8×10^3 m^3 s^{-1} across 70°S between 150°W and Cape Adare (170°E) for the period 1978-2001[2]. As expected from the high ice drift velocities in this region 65 % of this northward export occur west of 180° across ∼ 25% of the distance between 150°W and Cape Adare. Total net exports[3] from the eastern and western Ross Sea are roughly equal with 24.1×10^3 m^3 s^{-1} and 27.1×10^3 m^3 s^{-1}, but as previously shown sea ice formation in the western part is considerably stronger. Sea ice formed along the Ross Ice Shelf edge in the eastern Ross Sea is transported northwestward across

[2]For comparison, the modelled value of 47 ± 13×10^3 m^3 s^{-1} out of the inner Weddell Sea is close to the value of 50 ± 18×10^3 m^3 s^{-1} based on analyses of ULS measurements (Harms et al. 2001). This confirms that the model produces a realistic representation of sea ice drift and thicknesses, and hence transports.

[3]The total net sea ice export from a region is defined as the sum of the sea ice transports across all its boundaries, e.g. the net sea ice export for the eastern Ross Sea is the sum of import from the Amundsen Sea, export across 180° to the western Ross Sea, and northward export.

180° to join the fast northward drift in the western Ross Sea. The region north of the eastern Ross Sea continental shelf has lower drift velocities with minor sea ice formation and a considerable amount of sea ice imported from the Amundsen Sea.
Both the meridional and zonal net sea transports increase westward towards the Ross Sea. While both components are roughly of the same size in the Amundsen and Bellingshausen Seas, northward transport out of the Ross Sea is a factor of six larger than the zonal transport into it manifesting its strongly negative fresh water balance.

5.3 Sea ice retreat in the Bellingshausen Sea

A long-term sea ice retreat in the Amundsen and Bellingshausen Seas has been much commented on in recent years (Jacobs & Comiso 1997, Parkinson 2002, Zwally et al. 2002). It is generally linked to a warming trend in air temperatures around the Antarctic Peninsula. As commented on before, satellite data provide the only reliable data set that contains sea ice properties for any length of time and so provides information about its spatial and temporal variability. Sea ice concentrations from SSM/I passive microwave data were used in section 3.1.1 to validate model sea ice extents and distributions. Here they are employed to validate the interannual variability as represented by the model. Since the major source of interannual variability in the model is the atmospheric forcing data, this validation will also reflect on the representation of interannual variability in the NCEP Reanalysis dataset. The boundaries of Amundsen and Bellingshausen Seas are defined as in the previous section and both regions are analysed separately.
Comparison of monthly and mean annual anomalies[4] shows that model and SSM/I data display a very good agreement in the magnitude and location of the peaks for the Bellingshausen Sea (Fig. 5.9 b). For the Amundsen Sea the modelled magnitude of sea ice extent variability is overestimated slightly, but the location of the peaks agrees well with the SSM/I data (Fig. 5.9 a). This gives some confidence in the ability of model results and forcing data to correctly represent the variability of the sea ice and ocean system, so that the model can be used to draw conclusions on parameters not covered by observations.

[4] "Anomaly" will henceforth denote monthly mean values with the mean seasonal cycle removed, the mean annual anomaly is simply the arithmetic mean of the monthly anomalies over one year.

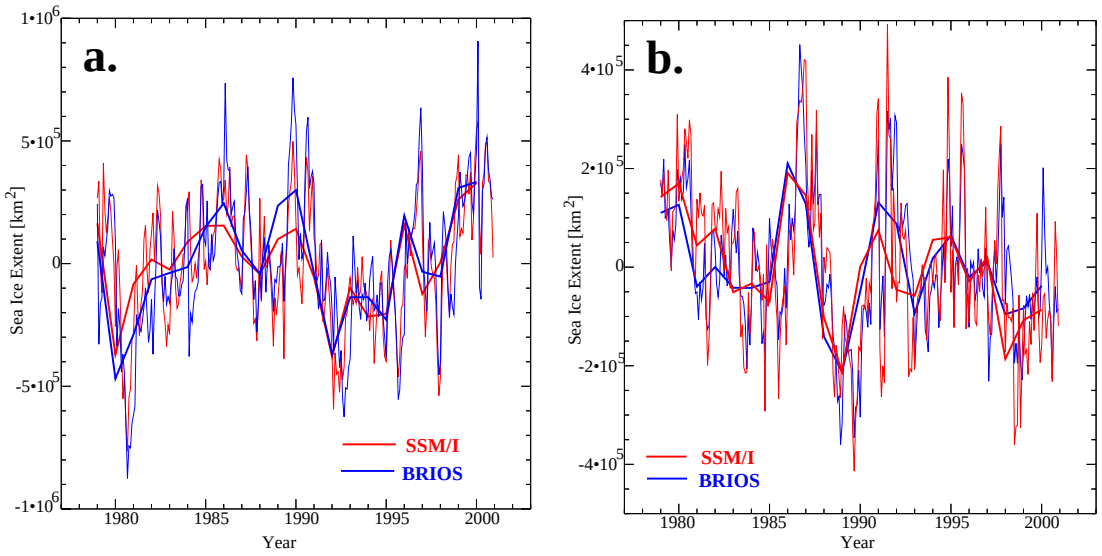

Figure 5.9: Monthly (thin line) and annual mean (thick line) anomalies of sea ice extent in **a.** the Amundsen and **b.** the Bellingshausen Seas as represented in the model BRIOS2.2 (blue) and in the SSM/I data (red).

Time series of sea ice extent for the Bellingshausen Sea (Fig. 5.9 b) show the reported decline in both model and SSM/I data. To quantify this trend and to identify which seasons are most affected, linear trends for each month were calculated. Both model and SSM/I data show negative trends significant above the 95% level for summer and autumn months (model: February to May, SSM/I January to May). These range from -5500 to -6900 m^2 per year in the model and from -10500 to -15200 m^2 per year in the satellite data. This discrepancy is due to model summer sea ice extents being much smaller than the observed ones. In the Amundsen Sea, however, both model and observation show positive trends in all months, none of which are significant above the 95 % significance level.

When the analysis for the model data is extended to 1958, the magnitude of the trend in the Bellingshausen sea ice extent decreases.[5] Rather than during autumn (February to May) and spring (October) as for 1979-2001, trends with statistical significance above 95 % are found all through winter for 1958-2001. A look at Fig. 5.10 a. shows that 1979 is located within a large positive anomaly in sea ice extent and volume explaining the large difference in magnitude for trends of the two time periods. However, NCEP Reanalysis data are thought to be of lower

[5]The trend on annual means is -2714 km^2 per year for 1958-2001 versus -5410 km^2 per year for 1978-2001.

quality before 1979 because of the missing inclusion of satellite data (Marshall 2002). Comments on the behaviour of the system before 1979 will therefore be made with caution. Nevertheless, model results indicate that using the late 1970s as a starting point to identify trends within the sea ice cover of the Bellingshausen Sea may well lead to misconceptions about the magnitude of these trends.

The reported sea ice retreat seems to be confined to the Bellingshausen Sea. Therefore the remainder of this section will be used to investigate the origin of this retreat, while interannual variability of the Amundsen sea ice is discussed in the following section with particular attention to sea ice transport from the Amundsen Sea to the eastern Ross Sea.

To determine which atmospheric variable is responsible for which part of the variability, the results of three sensitivity experiments are compared to the reference simulation with full atmospheric variability. In the first, a synthetic data set for the 2-m air temperature is used instead of the NCEP Reanalyses from 1948-2001. In the second, both components of the 10-m winds are replaced by a synthetic data set. In the third, the interannual variabiity of the net precipitation ($\mathcal{P} - \mathcal{E}$) was removed by replacing the NCEP Reanalyses for this forcing variable with a synthetic data set.

The synthetic data sets were computed by calculating a mean annual cycle of the years 1978-1996 and smoothing it with a 30-day running mean. To reinstate short-term variability, the difference between this smoothed data set and the unsmoothed data of 1985 was computed and added to the smoothed 1978-1996 data set. This synthetic data set is perpetually repeated each year for the relevant variable. The sensitivity experiments will be referred to as NO_T_VAR with no 2-m air temperature variability, as NO_UV_VAR with no variability in the 10-m wind velocities, and as NO_P-E_VAR where variability of the net precipitation ($\mathcal{P} - \mathcal{E}$) was removed.

Air temperature variability has a strong effect on sea ice extent and volume in the Bellingshausen Sea (Fig. 5.10). Warming trends significant at the 95 % level are found for both periods 1978-2001 and 1958-2001 between February and May and in October in agreement with the months that display negative trends in the sea ice extent (Fig. 5.11 a)[6]. Atmospheric warming trends are hence found in those months when the sea ice is particularly sensitive to temperature changes, i.e. during autumn freeze-up and the onset of spring melting at the sea ice edge.

[6] Air temperature trends are between 0.032 and 0.152°C per year for 1958-2001 for February to May and 0.125°C per year for October, respectively.

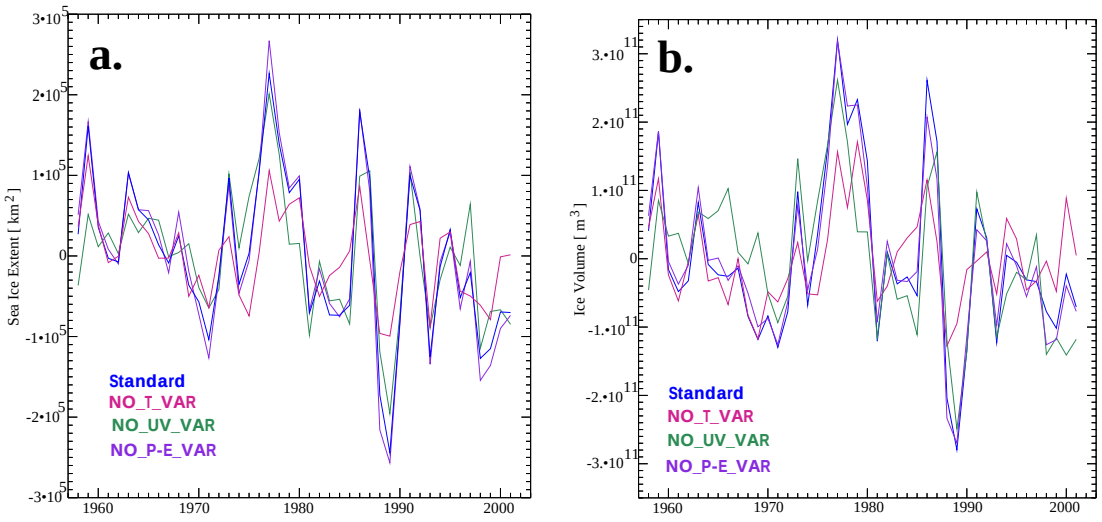

Figure 5.10: Annual mean anomalies in the Bellingshausen Sea of **a.** sea ice extent and **b.** sea ice volume for the standard simulation and sensitivity experiments (colour coded).

The period of sea ice melting is extended, since with the air close to the freezing point even a small positive trend results in temperatures exceeding the freezing point. In the standard simulation this leads to a decrease in sea ice volume for autumn and winter with a mean magnitude of -7.5 x 10^9 m^3 per year for 1978-2001 (Fig. 5.10 b).[7]

The meridional wind component shows a statistically significant decrease of -0.02 m s^{-1} per year for the annual means (Fig. 5.11 b). As a seasonal effect, this decrease can be identified in autumn with values around -0.04 m s^{-1} per year between March and May. Zonal winds south of 65°S in the Bellingshausen Sea show a positive trend, i.e become more easterly, between May and August.[8] When air temperature variability is removed in NO_T_VAR and the wind gains more relative influence in determining the interannual variability of sea ice extent and volume, the magnitude of the sea ice anomalies generally decreases and the location of smaller peaks does not agree with the standard simulation (Fig. 5.10). The removal of wind variability in NO_UV_VAR has a similar effect, but with smaller changes compared to the standard run. Both wind and air temperature

[7]Negative trends in the sea ice volume for 1958-2001 are smaller in magnitude than those for 1978-2001 and are only significant at the 90% level.

[8]Trends in the zonal wind component show magnitudes between 0.03 m s^{-1} per year, i.e. are about the same magnitude as those in the meridional wind component.

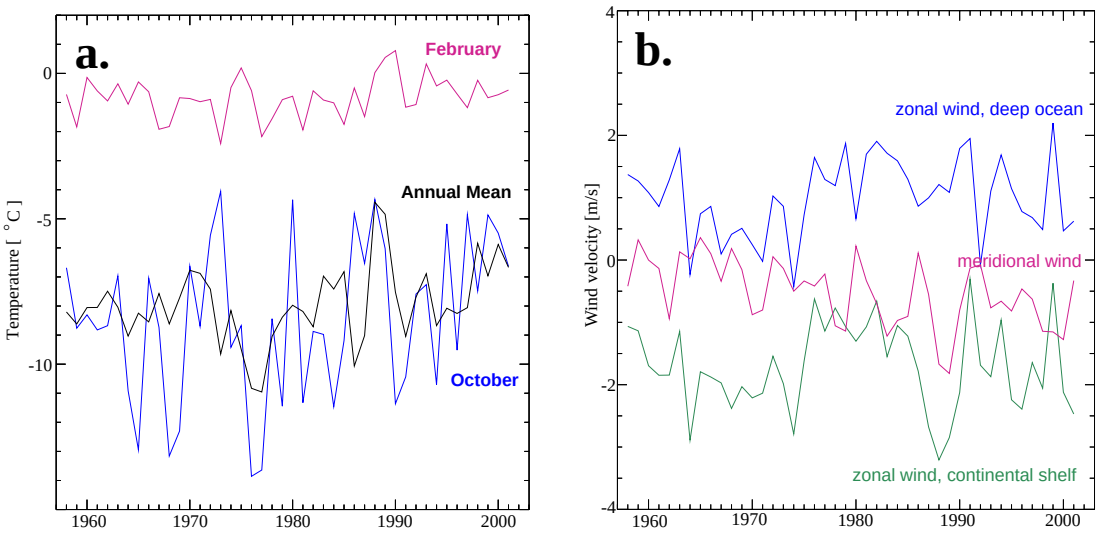

Figure 5.11: Time series of **a.** NCEP 2-m air temperatures. Shown are annual, February and October means (colour coded). **b.** NCEP 10-m wind velocities. Shown are annual means of the meridional wind component, the zonal component on the continental shelf (bottom depth < 1500m), and over the deep ocean north of the shelf. Values are a mean for the area south of 65°S between 60°W and 100°W.

variability thus control the sea ice extent and volume in the Bellingshausen Sea with air temperature having the stronger influence.

Winds in the Bellingshausen and Amundsen Seas show a zonal split of easterlies near the coast and westerlies further north (cf. Section 3.3), a behaviour which is reflected in time series of the zonal winds over and off the continental shelf in the Bellingshausen Sea (Fig. 5.11 b). Positive trends in both of these regimes thus imply different things: in the west wind drift, the trend leads to an increase in zonal wind velocities, while within the coastal easterlies it correspond to a decrease. Rather than implying weaker southerlies the negative trend in the meridional wind component signifies a change in the predominant meridional wind direction from southerly to northerly. More northerly winds during freeze-up lead to weaker northward transport of the newly formed sea ice and to less sea ice formation, which consequently leads to a smaller total sea ice volume. Stronger westerlies in winter drive the ice pack towards the Antarctic Peninsula rather than northward. Weaker coastal easterlies keep the ice within the Bellingshausen Sea rather than exporting it towards the Amundsen Sea. Hence, changes in all three wind regimes lead to a less divergent ice pack, a reduced sea ice extent and total ice volume. The removal of the interannual wind variability from the forcing data

lead to a reduction of trends in sea ice extent and sea ice volume (Fig. 5.10).

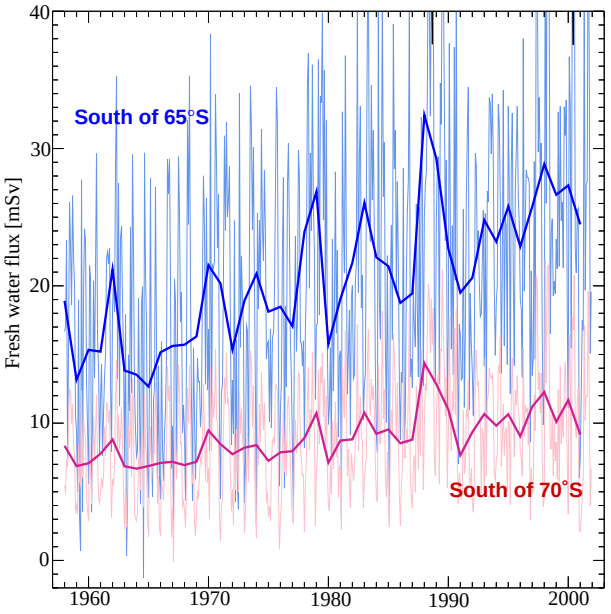

Figure 5.12: Time series of the fresh water flux due to NCEP net precipitation ($\mathcal{P} - \mathcal{E}$) for the Bellingshausen Sea south of 65°S (blue) and south of 70°S (red). Shown are annual means (thick,dark lines) and monthly means (thin, faint lines).

In contrast to the Ross Sea continental shelf (Section 4.3.3), net precipitation ($\mathcal{P} - \mathcal{E}$) represents a large contribution to the fresh-water budget of the Bellingshausen Sea. George VI and Abbot Ice shelves contribute 2.25 ± 0.5 mSv of fresh water and are only minor sources. The fresh-water flux due to sea ice is -3.6 ± 6.7 mSv south of 65°S - the small net value and large standard deviation reflect the inclusion of the sea ice edge and the interannual variability of its location - and -10.8 ± 2.9 mSv south of 70°S. A fresh-water flux of 20.6 ± 4.8 mSv due to net precipitation ($\mathcal{P} - \mathcal{E}$) results in a positive fresh-water balance for the Bellingshausen Sea south of 65°S. A large positive trend in net precipitation ($\mathcal{P} - \mathcal{E}$) [9](Fig. 5.12) has only a small effect on sea ice extent and volume (Fig. 5.10 b) in agreement with a model study by Marsland & Wolff (2001).
Worby et al. (1996) report snow ice formation being common within the Bellingshausen sea ice, a result which agrees with the high net precipitation rates in the NCEP Reanalyses and the consequently thick snow cover. An increase of net

[9]Its magnitude is 0.28 mSv per year for annual means and between 0.18 mSv and 0.61 mSv for time series of separate months of the year

precipitation and hence snow accumulation should result in increased snow ice formation and an increase in sea ice volume. Similarly, an increase in net precipitation over the open ocean should lead to an increase in sea ice volume by increasing the stability of the upper ocean and thus reducing upward ocean heat flux. Both mechanism, however, will not have a large effect in the Bellingshausen Sea, since much of the positive trend in net precipitation is confined to the area north of 70°S. As this latitude band usually contains the winter sea ice edge, much of its sea ice is advected from further south and not formed locally, but melts in this region (Fig. 3.7). As shown earlier, the location of the sea ice edge is highly sensitive to air temperature variability which appears to be the limiting factor of sea ice extent in the Bellingshausen Sea, again in agreement with model results by Marsland & Wolff (2001).
Thus, the analysis of the sensitivity experiments identified not only an increase in air temperature in the Bellingshausen Sea, as previously assumed, but also a decrease in meridional wind strength, a change in its predominant direction from southerly to northerly, and more westerly zonal winds as causes for the sea ice retreat in the Bellingshausen Sea. The latter conclusion is drawn with caution since the increase in westerlies, along with the increase in net precipitation, might be due to the spurious interannual variability introduced by the beginning assimilation of satellite sea ice data in the late 1970s (Marshall et al. 2002).

5.4 Sea ice export from the Amundsen Sea

Sea ice transport from the Amundsen to the Ross Sea represents the main import to the Ross Sea (see Section 5.2). A better understanding of the processes governing its interannual variability is thus desirable. The general drift pattern in this region (see also Section 3.3) and the simulated variability of sea ice drift on small temporal and spatial scales in the model were validated in Section 5.1 giving confidence of a realistic representation.
Sea ice export from the Amundsen into the Ross Sea reaches a maximum in May and June at an average of $23\times10^3 m^3 s^{-1}$ and a minimum in October when the transport is small and even slightly eastward. As well as the seasonal cycle, the interannual variability of the sea ice transport across 150°W is in phase with the mean zonal wind velocity with a correlation coefficient r=0.72 for monthly mean anomalies, i.e., monthly mean values with the seasonal cycle removed (Fig.5.13 a & b). Between June and January the correlation exeeds this value and hence

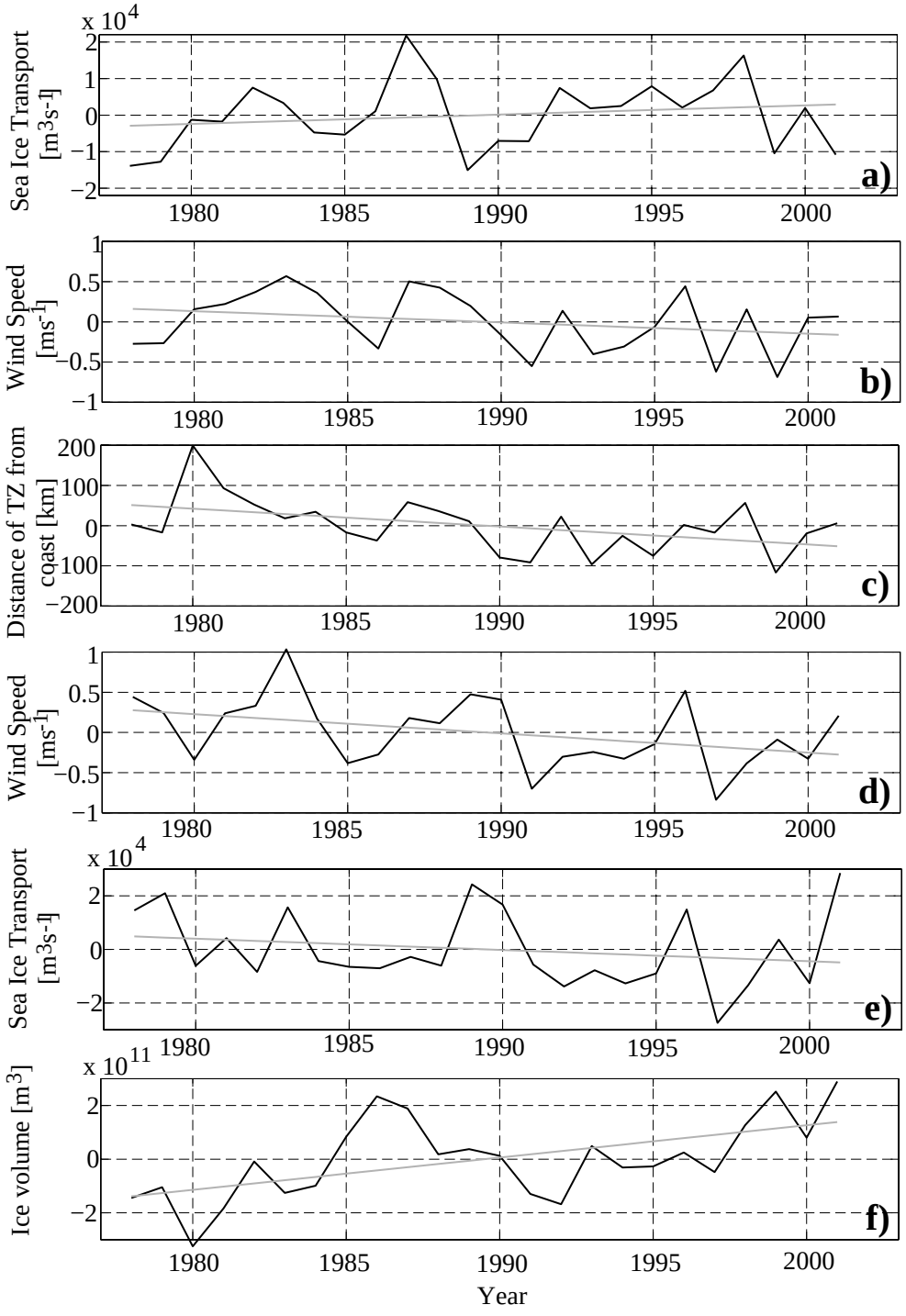

Figure 5.13: For the Amundsen Sea (100°W - 150°W), with westward and northward velocities and transports defined as positive, annual mean anomalies (black) and trend lines (gray): **a.** Sea ice transport across 150°W, **b.** Mean zonal wind velocity, **c.** Mean location of the transition zone (TZ) from westward to eastward velocities in the zonal winds, **d.** Mean meridional wind velocity, **e.** Sea ice transport across 70°S, and **f.** Sea ice volume south of 70°S.

explains more than 50 % of the transport variability with a maximum in August (r = 0.92). During the sea ice minimum and the onset of the growth season, between February and May, the correlation drops due to an underestimated summer sea ice cover in the model (cf Section 3.1 & 3.2).

The meridional winds determine how much sea ice is available within the band of easterly winds to be transported westward into the Ross Sea. Between 1978 and 2001, south of 70°S, a strong per year increase in sea ice volume (1.32×10^{10} m^3, Fig. 5.13 f) is connected to a negative trend in NCEP meridional wind speed (0.023 ms^{-1} per year, Fig. 5.13 d) and is consistent with the trend in sea ice extent (Fig. 5.9 a). The corresponding decrease in the northward sea ice transport is strongest in April (310 m^3s^{-1} per year, Fig. 5.13 e), at the zonal wind speed maximum, and in August and September (2800 m^3s^{-1} per year) at maximum sea ice extent. Despite a decrease in the zonal winds south of 70°S (0.014 m s^{-1} per year, significant at the 90% level, Fig. 5.13 b), there is an increase in the zonal sea ice transport (253 m^3s^{-1} per year, Fig. 5.13 a), but only significant at the 75% level, due to the increase of sea ice volume close to the coast. On a seasonal basis, an increase in the September zonal sea ice transport (1870 m^3s^{-1} per year) is related to enhanced zonal wind strength (0.091 m s^{-1} per year). All trends are statistically significant at the 95% level unless stated otherwise.

The drift of buoy 9364 in late 2001 and iceberg B10A in 1996 were cited earlier as evidence for events of strong northward sea ice transport east of 150°W. These events coincide with minima in sea ice transport into the Ross Sea, strong southerly and weak easterly winds (Fig. 5.13 a, b & d), and maxima in the northward sea ice transport (Fig. 5.13 e). A decrease in easterly mean zonal wind speed does not necessarily correspond to a decrease in the actual wind velocity, but often represents a southward shift of the transition zone between easterly and westerly winds (Fig. 5.13 c). This enables the sea ice to join the northeastward drift before it reaches the eastern Ross Sea. Similarly, the increase in zonal wind strength in September manifests itself as a widening of the band of easterly winds along the coast.

Weak meridional winds and strong zonal winds result in strong sea ice transport into the Ross Sea, e.g., 1998 (Fig. 5.13). Similarly, strong meridional and weak zonal winds lead to weak westward sea ice transport, e.g. 1990. In addition, the reduction of ice volume in the southern Amundsen Sea by strong meridional winds can lead to a relatively low zonal sea ice transport despite the presence of strong easterly winds, e.g., in 1983/84, 1996 (Fig. 5.13 a, b & d). Conversely, if thick

sea ice accumulates in the southern Amundsen Sea, because of weak southerly winds, fairly weak easterlies can still result in high sea ice transport rates, e.g., 1986 and 1993 (Fig. 5.13 a, b & d). Anomalies can also build up over longer time periods as between 1985 and 1987 when weak zonal and meridional winds helped to accumulate a large volume of sea ice in the Amundsen Sea (Fig. 5.13 b & d). When the easterlies increased again in 1987, this resulted in the maximum westward sea ice transport seen in the 24-year time period investigated (Fig. 5.13 a).

Interannual variability of sea ice extent and related atmospheric parameters at periods between 3 and 6 years have repeatedly been reported for the Southern Ocean (White & Peterson 1996, Venegas et al. 2001). A Fourier analysis for model results in the Amundsen Sea (not shown) yields a period of 6 years for monthly mean anomalies of both NCEP wind components, sea ice transport, and volume, along with signals at various periods between 2.5 and 4 years. Sea ice transport across 150°W and 70°S and sea ice volume south of 70°S also suggest longer-term variability at a period of $\sim$ 12 years (Fig. 5.13).

5.5 Interaction with the Ross Sea ice cover

The Ross Sea polynya (Fig. 3.5) is the largest, most persistent coastal polynya in the Southern Ocean. Vigorous sea ice production and export from this latent heat polynya, and the substantial amount of sea ice imported to the Ross Sea from the Amundsen Sea as noted above, make interactions between these sea ice regimes of particular interest.

Modelled large scale drift pattern and sea ice thickness distribution suggest distinct sea ice regimes in the eastern and western Ross Sea. We thus split the Ross Sea into an eastern and a western part along 180°, a meridian typically east of the main polynya area (Fig. 3.5), taking 70°S as the northern boundary. For the period 1978-2001, the September mean modelled sea ice thicknesses in the Amundsen Sea, and eastern and western Ross Sea are 1.61 $\pm$ 0.13m, 1.65 $\pm$ 0.13m, and 1.27 $\pm$ 0.18m, respectively. Consistent with the analyses of Tin et al. (2003) and Zwally et al. (1985), this suggests sea ice in the western Ross Sea is formed locally, but a large proportion of eastern Ross sea ice is advected from the Amundsen Sea.

A positive correlation (r=0.66, significant at the 99% level, as are all following correlation coefficients) exists between sea ice import across 150°W and the sea

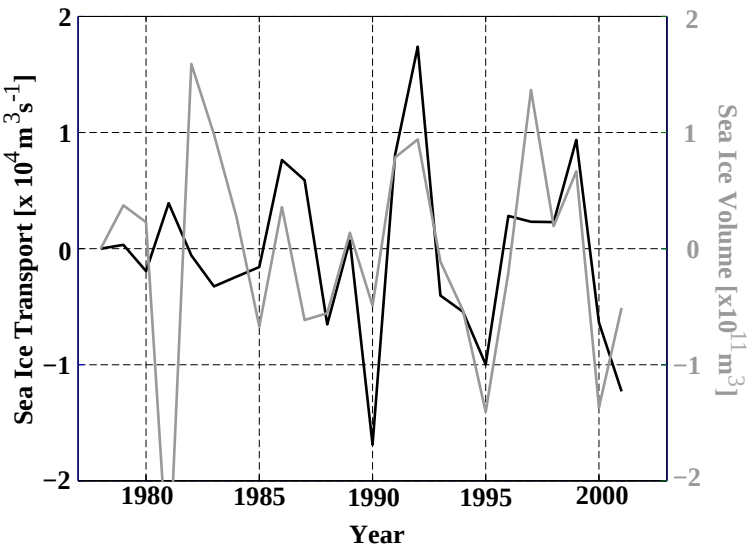

Figure 5.14: Annual mean anomaly (1978-2001) of sea ice transport across 150°W (black line, left scale) and sea ice volume in the eastern Ross Sea (gray line, right scale).

ice volume in the eastern Ross Sea (Fig. 5.15 a). Similarly, the mean sea ice growth rate in the eastern Ross Sea is anticorrelated to both sea ice volume and import (r = -0.59), indicating that sea ice imported from the Amundsen Sea inhibits local sea ice formation. A map of correlation coefficients of the sea ice import time series across 150°W onto sea ice thickness anomalies confirms that the positive correlation is confined to the southeastern Ross Sea (Fig. 5.15 b). The inverse correlation between meridional and zonal sea ice export from the Amundsen Sea (Section 5.4) is documented by an area of negative correlation of sea ice thickness north of 70°S in the Amundsen Sea. Analysis of separate months reveals that the influence is strongest in autumn and early winter (March to July) at the maximum of sea ice transport across 150°W and growth rate. The region of maximum correlation between sea ice thickness and sea ice transport across 150°W moves further west up to 180° with increasing lag up to 3 months. In the western Ross Sea, there is no significant correlation between import from the Amundsen Sea and local sea ice thickness, i.e., volume (Fig. 5.15 b). Much of the sea ice formation in the eastern Ross Sea occurs in a narrow strip along the ice shelf edge. Wind drives this sea ice northwestward across 180° to join the fast northward drift in the western Ross Sea. Amundsen sea ice is imported into the region north of the eastern Ross Sea continental shelf which is more static

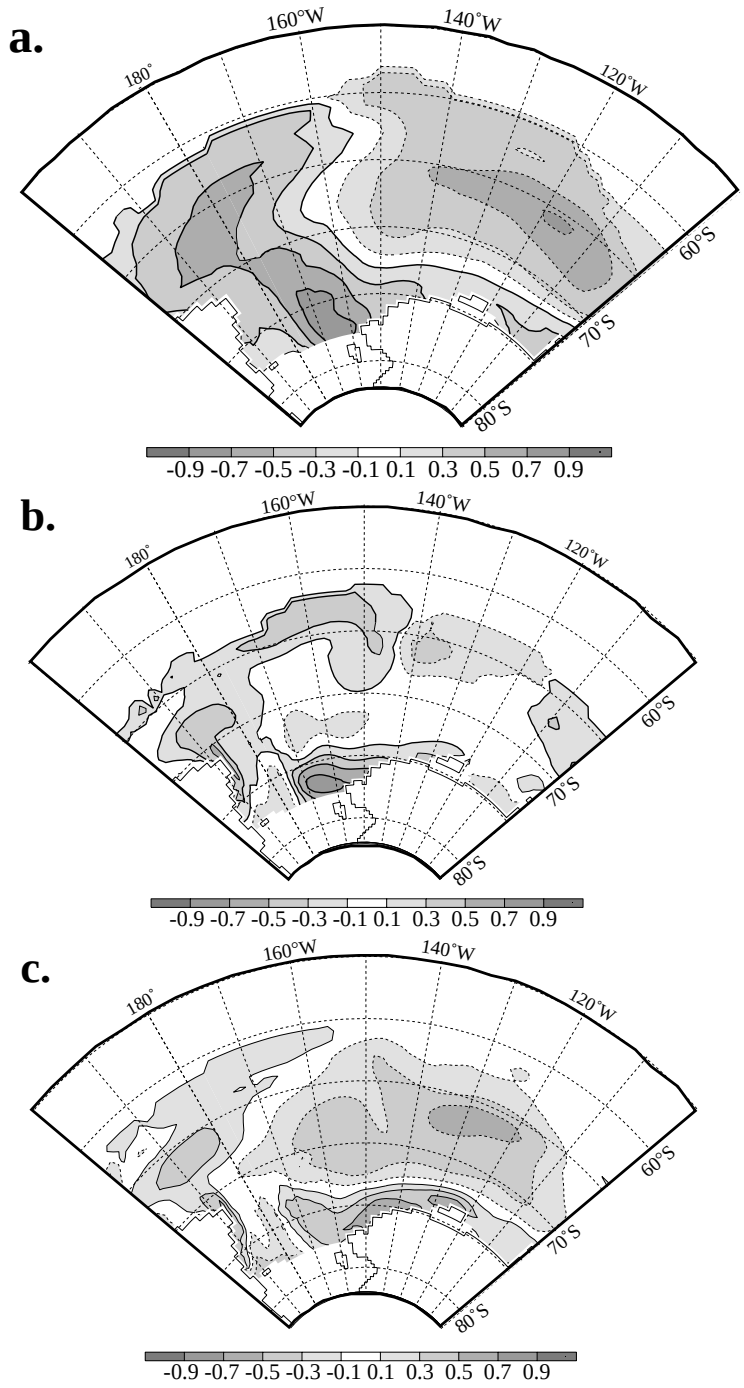

Figure 5.15: Maps of correlation coefficients onto sea ice thickness anomaly: **a.** for sea ice transport anomaly across 150°W, annual means, zero lag; **b.** for sea ice transport anomaly across 70°S between 180° and Cape Adare, monthly means for May (transport) and June (thickness), **c.** for sea ice transport anomaly across 70°S between 180° and Cape Adare, monthly means for July (transport) and August (thickness). Correlation coefficients $r > 0.5$ are significant at the 99 % significance level. Dashed contours denote negative r-values.

with only minor sea ice formation.

The northward transport is mainly controlled by the meridional drift velocity, i.e., by the wind speed, with r > 0.8 from April to January for wind speed and meridional drift velocities. Only around the autumnal equinox, at sea ice minimum (r > 0.71), and in early spring near the sea ice maximum (r > 0.59), does sea ice volume in the western Ross Sea significantly influence the meridional transport. In early autumn, northward sea ice transport depends strongly on whether any sea ice has remained within the western Ross Sea over summer to be transported north. In late winter, consolidation of the ice to the north prevents free drift across 70°S, leading to an increased dependence of the northward ice export on sea ice thickness.

Between May and November the meridional transport across 70°S between 180° and Cape Adare is negatively correlated with sea ice thickness in the southwestern Ross Sea with a lag of 1-2 months (Fig. 5.15 c & d) as strong northward transport depletes the sea ice volume in this region. Positive correlations further north extend eastward and westward tracing the path of the sea ice originating from the western Ross Sea (Fig. 5.15 d).

Large northward transport in the western Ross Sea leads to a thickening of sea ice in the eastern Ross Sea (Fig. 5.15 c & d) and annual means of this transport are positively correlated to Amundsen sea ice import across 150°W south of 70°S with r=0.77. Strong northward export in the western Ross Sea then appears to facilitate the import of thick Amundsen Sea ice into the eastern Ross Sea. The correlation is especially strong in early winter (May and June) for a recently closed Ross Sea ice pack. This indicates that in fact sea ice conditions in the western Ross Sea determine the transport of Amundsen Sea ice into the eastern Ross Sea. Again, a substantial area of negative correlation is found north of the transition zone in the Amundsen Sea (Fig. 5.15 d). Since strong northward transport in the western Ross Sea leads to strong zonal import from the Amundsen Sea, it is also negatively proportional to the meridional export across 70°S in the Amundsen Sea, and to sea ice thicknesses north of this line.

5.6 Summary

A detailed analysis of sea ice drift in the Amundsen Sea was used as a basis for an investigation into the interaction between the sea ice regimes of the marginal seas

of the South Pacific and of its interannual variability. BRIOS2.2 performs well in representing sea ice drift in the Amundsen Sea also at small temporal and spatial scales, i.e., scales approaching the model resolution. Some misrepresentations pointed out in Section 5.1 can be clearly attributed to deficiencies in the NCEP forcing data. NCEP winds are generally too slow and do not capture peak speeds during storm events and the transition zone between easterly and westerly winds is slightly dislocated. Both problems are probably due to the coarse resolution at which the data is available.

The westward sea ice drift along the coast is predominantly wind-driven while in general ocean influence is surprisingly small. Daily to weekly variability of zonal and meridional ice velocities is dominated by the zonal winds, consistent with the predominantly zonal drift pattern and higher zonal wind velocity coherence. The recent sea ice retreat in the Bellingshausen Sea has been shown to depend on an increase in air temperature, a trend to more westerly zonal winds, and a change to predominantly northerly meridional winds. It is highly insensitive to a strong increase in net precipitation. The decrease in meridional winds extends into the Amundsen Sea and, there, leads to a sea ice thickening along the coast. For the region South of 70°S, model results show that roughly half of the sea ice generated in the Amundsen Sea is exported into the eastern Ross Sea. Transport across 150°W depends on the interplay between the strength of zonal winds, location of the transition between easterlies and westerlies, and variable northward transport by meridional winds. Interannual variability in the winds and sea ice parameters is strongest at a period of 6 years. This is on the longer side of previous circumpolar and regional findings which are based on sea ice extent, and, therefore, predominantly on the meridional wind variability. However, the interplay between meridional and zonal winds might lead to longer periods in zonal sea ice transport.

Sea ice volume and growth rates in the eastern Ross Sea depend on the amount of sea ice imported from the Amundsen Sea. In the western Ross Sea ice characteristics are determined predominantly by the local atmospheric and oceanic conditions. The import of Amundsen Sea ice into the eastern Ross Sea and eastern Ross Sea ice thicknesses show a strong positive correlation to northward export from the western Ross Sea. It appears that in the Ross Sea removal of locally formed sea ice is necessary for the intrusion of thick Amundsen Sea ice to take place. Changes in western Ross Sea ice formation that might affect dense water formation have thus to be of local origin.

Chapter 6

Variability of dense water formation in the Ross Sea

6.1 Variability of Ross Sea shelf water properties

In the previous chapters the basic mechanisms underlying the formation of highly dense shelf waters on the Ross Sea continental shelf have been described and analysed, confirming the model's ability to represent these satisfactorily. Reflecting the interest the variability of potential sources of AABW has gained in recent years (Jacobs & Giulivi 1998, Robertson et al. 2002), this analysis will now be extended to include the interannual variability of the volume, salinity, and potential temperature of these dense Ross Sea waters and of their formation mechanisms. As a density threshold a value of $\sigma_\Theta \geq 27.9$ was chosen, since this ensures that mixing products between shelf waters with densities above this threshold and CDW or MCDW potentially have the right characteristics to evolve into AABW. This dense water volume mainly contains HSSW formed in the southwestern Ross Sea that spreads across the western part of the continental shelf.

To obtain a sense of the typical salinity and potential temperature variability of the HSSW, a point was chosen north of Ross Island as shown in Fig. 6.1 a. Its position at 171.0°E, 77.2°S is located in the centre of the HSSW dome seen in summer salinity sections (Fig. 6.1 b) and is hence representative of HSSW characteristics. Choosing a single representative point prevents the inclusion of spatial averaging artifacts in the time series. The monthly mean modelled salinities and potential temperatures were calculated for depths below 300 m,

since this limit excludes the upper water column subject to a large signal of short-term variability in both salinity and potential temperature, which might obscure longer-term changes. The choice of position north of Ross Island also gives the opportunity of comparison to observations (Jacobs et al. 2002) and model validation.

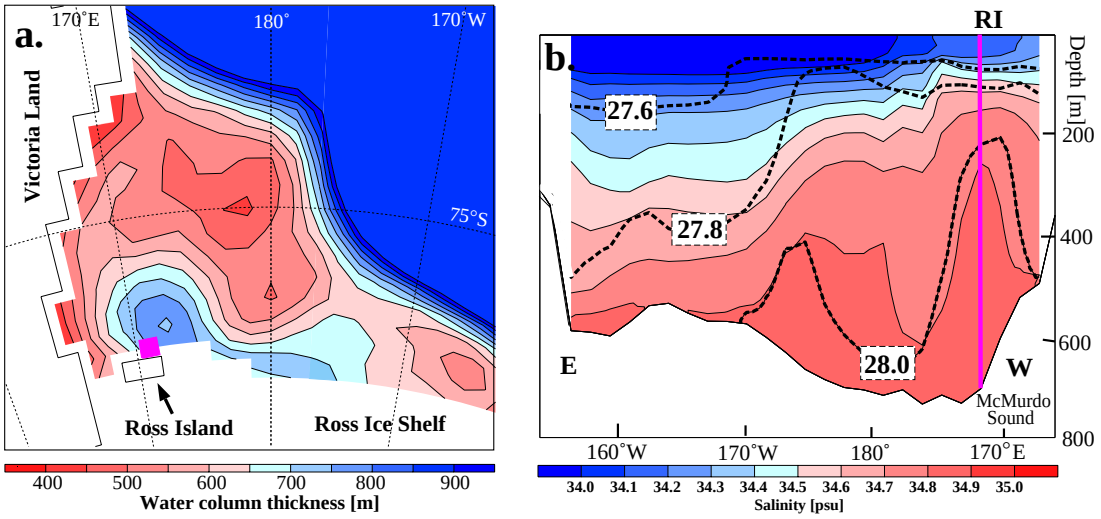

Figure 6.1: **a.** Map of water column thickness for the Ross Sea continental shelf. The position 171.0°E, 77.2°S is marked by the magenta square. **b.** Modelled section along the Ross Ice Shelf edge, facing south, for salinity (colour coded) and density (thick, dashed contour lines). The position of the time series is marked by the magenta line. RI = Ross Island.

All three time series show an interannual variability with a distinctly larger magnitude than that of the seasonal cycle (Fig. 6.2). Salinities are within the range commonly associated with HSSW in the Ross Sea and potential temperatures are slightly above sea surface freezing point, except for a ~ 0.07°C rise in the 1990s. The time series of dense water volume (Fig. 6.2 a) shows a $\sim 4 \times 10^{13}$ m^3 increase up to the early 60s and then plateaus out for the next two decades. From 1980 onwards the dense water volume decreases to the 1960 level. Shorter-term variations with characteristic periods of 5 and 9 years are superimposed on the decadal variability. Both periods can also be identified in the salinity and potential temperature variability of the HSSW. The temporal variation of the HSSW salinity corrresponds closely to that of the dense water volume, because at a few degrees above the sea surface freezing point salinity dominates the density of seawater. However, the recent decrease is sharper in salinity and only appears in

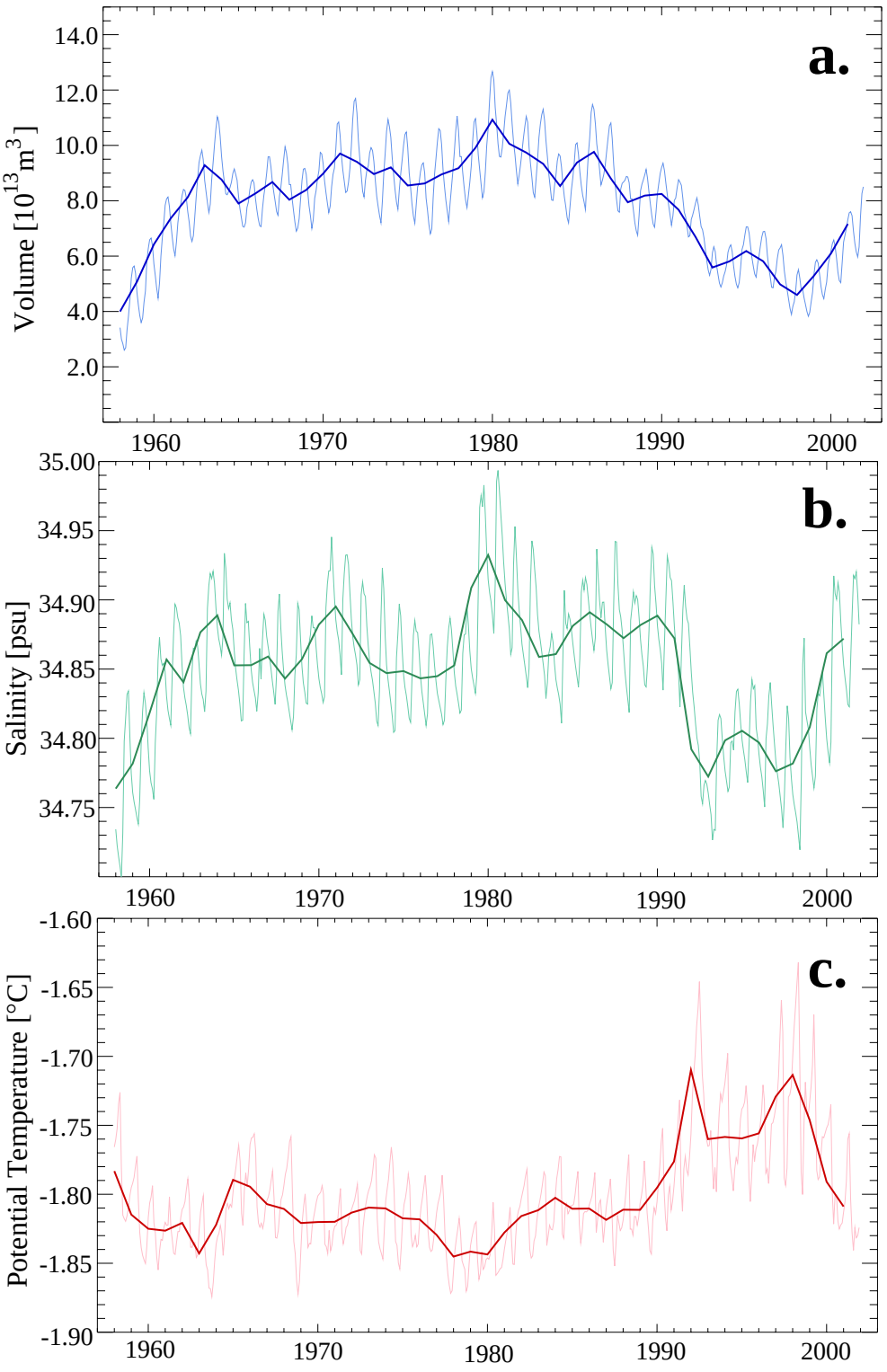

Figure 6.2: Monthly (thin lines) and annual (thick lines) means of **a.** volume of dense water ($\geq 27.9\ \sigma_\Theta$) on the Ross Sea continental shelf, **b.** mean HSSW salinity below 300 m northeast of Ross Island (171.0°E, 77.2°S as marked in Fig. 6.1), **c.** mean potential temperature for the same position.

the early 1990s and the shorter term variability is more pronounced.

A freshening of the HSSW in the southwestern Ross Sea since the 1960s has been reported from observations by Jacobs et al. (2002). Their data indicate a decrease in the HSSW salinity of ~ 0.06 psu at 700 m and ~ 0.03 psu at 200 m between the periods 1963-1978 and 1982-1997. They report a further decrease of approximately equal magnitude for a station taken in February 2000. Naturally, the observational data base is sparse with averages based on five stations between 1963-1978 and six between 1982-1997 and intervals varying between 11 months and 10 years. All stations were taken between December and January at a position off the northeastern coast of Ross Island with a bottom depth of 900 m. The exact months are given in Fig. 6.3.

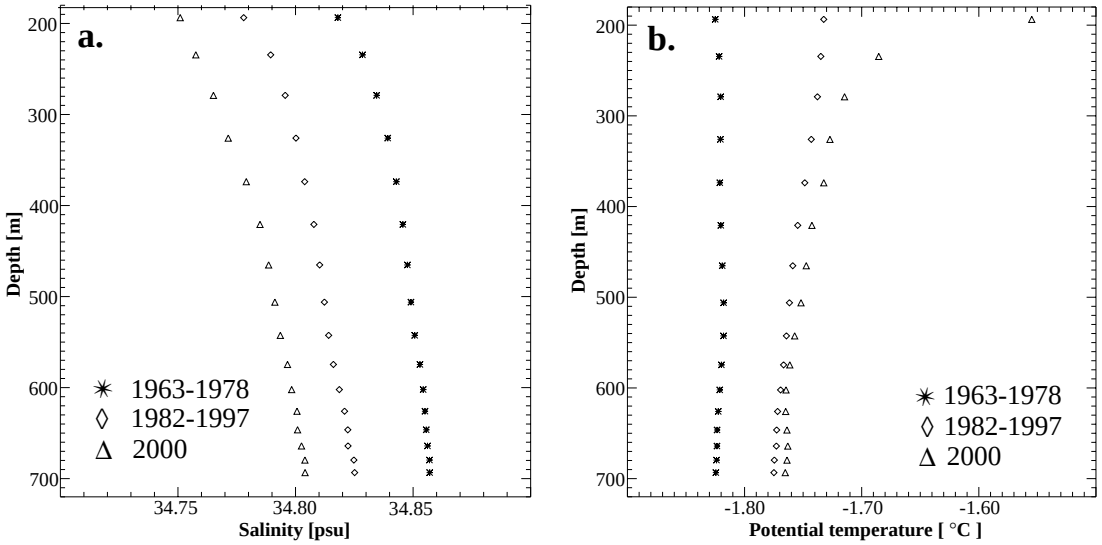

Figure 6.3: Simulated **a.** salinity and **b.** potential temperature profiles below 200m north of Ross Island. The 1963-1978 profile is an average of five monthly means (February 1963, January 1967, January 1968, December 1976, January 1978), whereas the 1982-1997 profile is an average of six monthly means (January 1982, January 1984, February 1994, December 1994, December 1995, January 1997). Also shown are February 2000 profiles.

To compare model results and observations, the model results were sampled for those months in which the station data were taken at the point 171.0°E, 77.2°S. As described above, this point is representative of HSSW conditions in the model and closest to the station location, being the easterly point north of Ross Island. The model bottom depth is only ~ 700 m due to the smoothing of the bottom

topography. The data were averaged over the same time periods as in Jacobs et al. (2002), i.e. 1963-1978 and 1982-1997.

Thus averaged the model salinity profiles (Fig. 6.3 a) show the same monotonous decline of HSSW salinities over the 40-year period as observed. Salinities of the 1963-1978 profile are very close to those observed. The salinity decrease towards 1982-1997 is ~ 0.04 psu at both 200 m and 700 m, while between 1982-1997 and 2000 a smaller decrease of ~ 0.025 psu is seen. Although the model underestimates the magnitudes of variability, the observed decrease of HSSW salinities is reproduced for a sample that is equivalent of station data available.

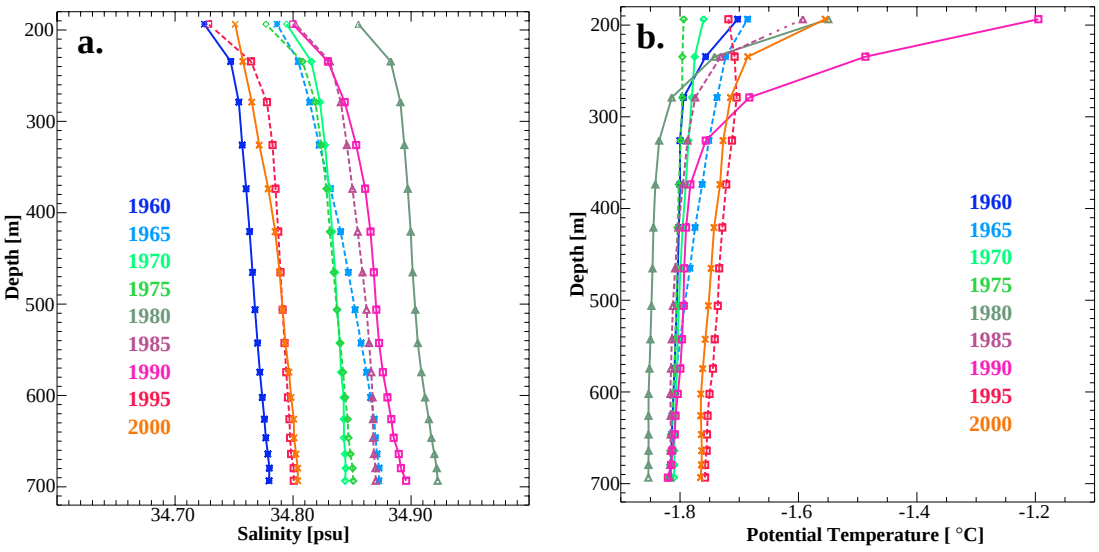

Figure 6.4: Simulated **a.** salinity and **b.** potential temperature profiles below 200 m north of Ross Island. February profiles are shown at 5-year intervals for the years colour-coded.

Jacobs et al. (2002) comment on potential temperatures being constant throughout the entire period covered by observations and close to the surface freezing point over the entire water column below 200 m. Model potential temperatures are warmer and display more variability with a warm near-surface anomaly apparent in the year 2000 profile (Fig. 6.3 b). A possible reason for this is given in Section 6.3.

The sampling frequency of the observations is highly irregular, and also the model time series (Fig. 6.2 b) does not show the steady decrease of HSSW salinities suggested by Jacobs et al. (2002). The model data was resampled at a regular interval of 5 years for February profiles of potential temperature and salinity,

shown in Fig. 6.4. February profiles were chosen, because end of summer conditions represent the effect of a full seasonal cycle of salinity increase due to brine release and freshening due to summer melting.
The salinity profiles sampled at a 5-year interval reflect the behaviour of the salinity time series shown in Fig. 6.2. Variability at a period of $\sim$ 10 years, i.e., just resolved by the 5-year sampling interval, overlies a longer signal that extends over the whole 44-year period analysed. While model salinities in the 1990s are lower than those in the preceeding decades, they are not the result of a the steady decrease deduced from the observations by Jacobs et al. (2002). Since the model results show the same behaviour when sampled equivalently to the observations, it can be concluded that the negative trend described by Jacobs et al. (2002) is an aliasing artifact due to irregular sampling. As mentioned previously, the Ross Sea continental shelf is one of the most frequently sampled locations in the Antarctic marginal seas. However, it appears that even this extensive data set is insufficient to resolve dense water variability and should be used with care.

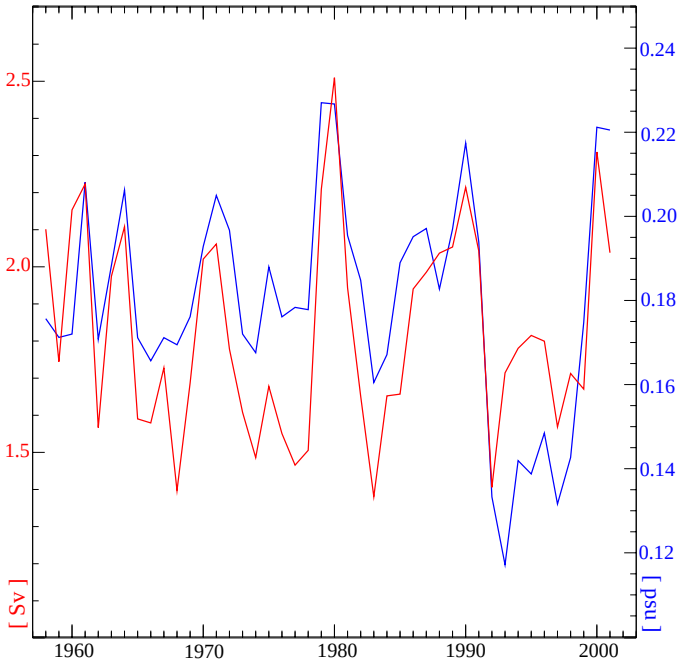

Figure 6.5: Detrended time series of annual means of the maximum transport of the anticyclonic circulation cell on the Ross Sea continetal shelf (red, left scale) and the salinity difference between High and Low Salinity Shelf Water (blue, right scale).

In Section 4.3 it was proposed that the anticyclonic circulation cell on the Ross Sea continental shelf is predominantly thermohaline driven. This conclusion was

drawn on the basis of the seasonal variation of the maximum transport and the salinity gradient between High and Low Salinity Shelf Waters in the western and eastern Ross Sea. Wind was attributed minor importance since confined to the surface layer. To increase the confidence in this hypothesis, the salinity gradient was expressed as the difference between the HSSW salinity north of Ross Island and the LSSW salinity below 300 m at the point 171.0°W, 77.8°S. Its interannual variability was compared to that of the maximum transport of the anticyclonic circulation cell on the Ross Sea continental shelf (Fig. 6.5). A good correlation (r=0.68), significant at the 95% confidence level, confirms the strong influence of the thermohaline structure on the circulation on the Ross Sea continental shelf including the ice shelf cavity. Noteworthy is also that the salinity difference beween the western and eastern Ross Sea continental shelf remains positive throughout the time period analysed in agreement with observations (Jacobs & Giulivi 1998). In contrast to the shift in the location of the density maximum and the associated change in circulation pattern identified by Timmermann et al. (2002b) on the southern Weddell Sea continental shelf, the circulation pattern and density distribution on the Ross Sea continental shelf do not change their basic shape, but only vary in strength.

6.2 Local atmospheric variability and its effect

Variability of the NCEP forcing data is an important source of interannual variability of water masses in the model and the only external source. Since circulation and water mass distribution at the northern model boundary at 50°S are temporally invariant, signals from lower latitudes can only enter the system through the atmospheric forcing data and not through the ocean. Origins of the interannual dense water variability on the Ross Sea continental shelf might either lie in the local atmospheric variability transmitted to the ocean by fresh water fluxes from sea ice and net precipitation or in circulation changes due to the local wind variability. Another possible source is the advection onto the continental shelf of anomalies in sea ice or ocean which were induced upstream, i.e., in a remote source.

To determine which atmospheric variable is responsible for which part of the variability the results of the two sensitivity experiments NO_T_VAR and NO_UV_VAR[1], where interannual variability of air temperature and wind velocities was removed,

[1]See Section 5.3 for a more detailed description of the synthetic data sets used to replace

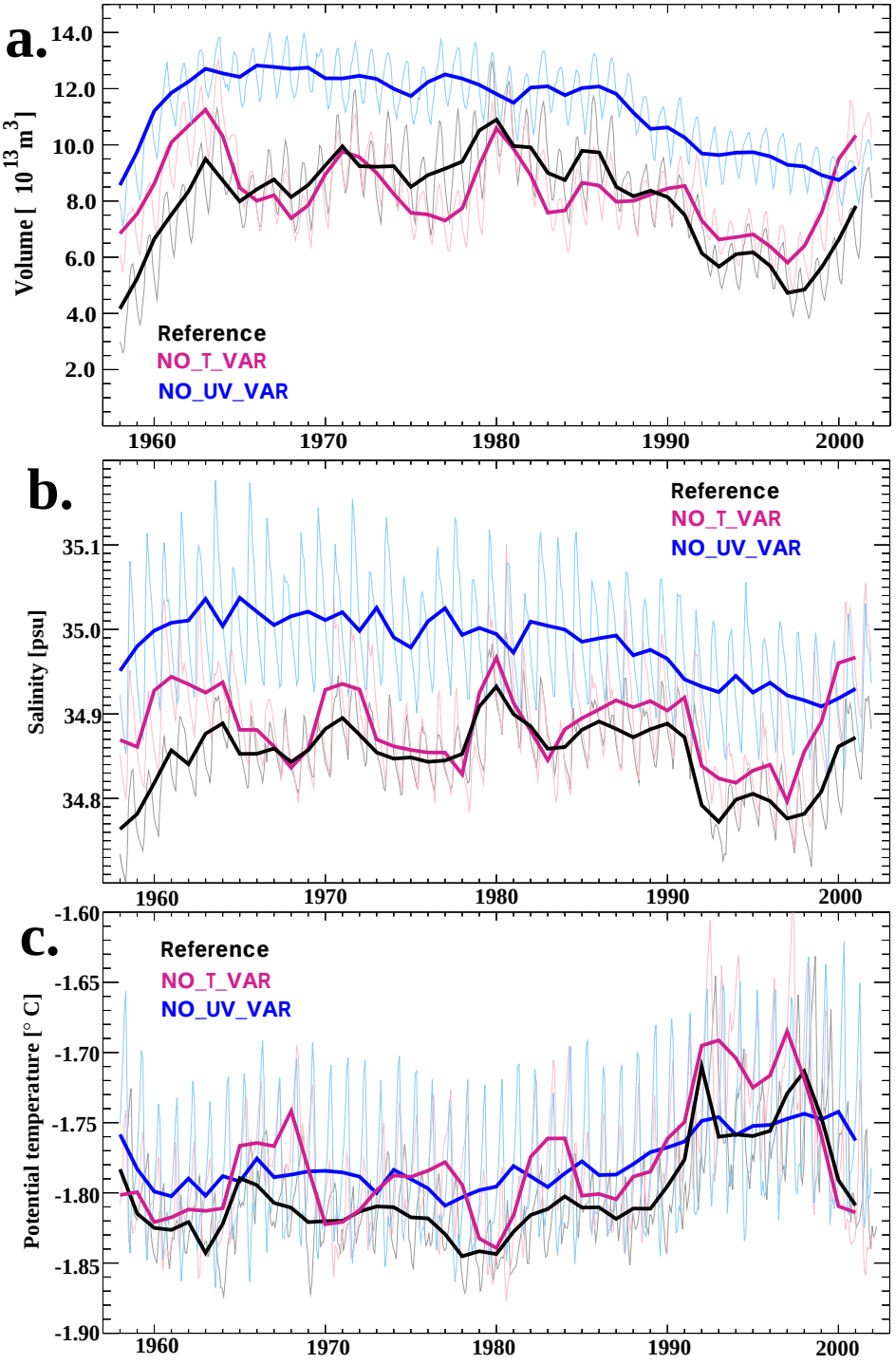

Figure 6.6: For the reference simulation and sensitivity experiments (colour coded): Monthly (thin lines) and annual (thick lines) means of **a.** volume of dense water ($\geq$ 27.9 σ_Θ) on the Ross Sea continental shelf, **b.** mean HSSW salinity below 300 m northeast of Ross Island (171.0°E, 77.2°S as marked in Fig. 6.1), **c.** mean potential temperature for the same position.

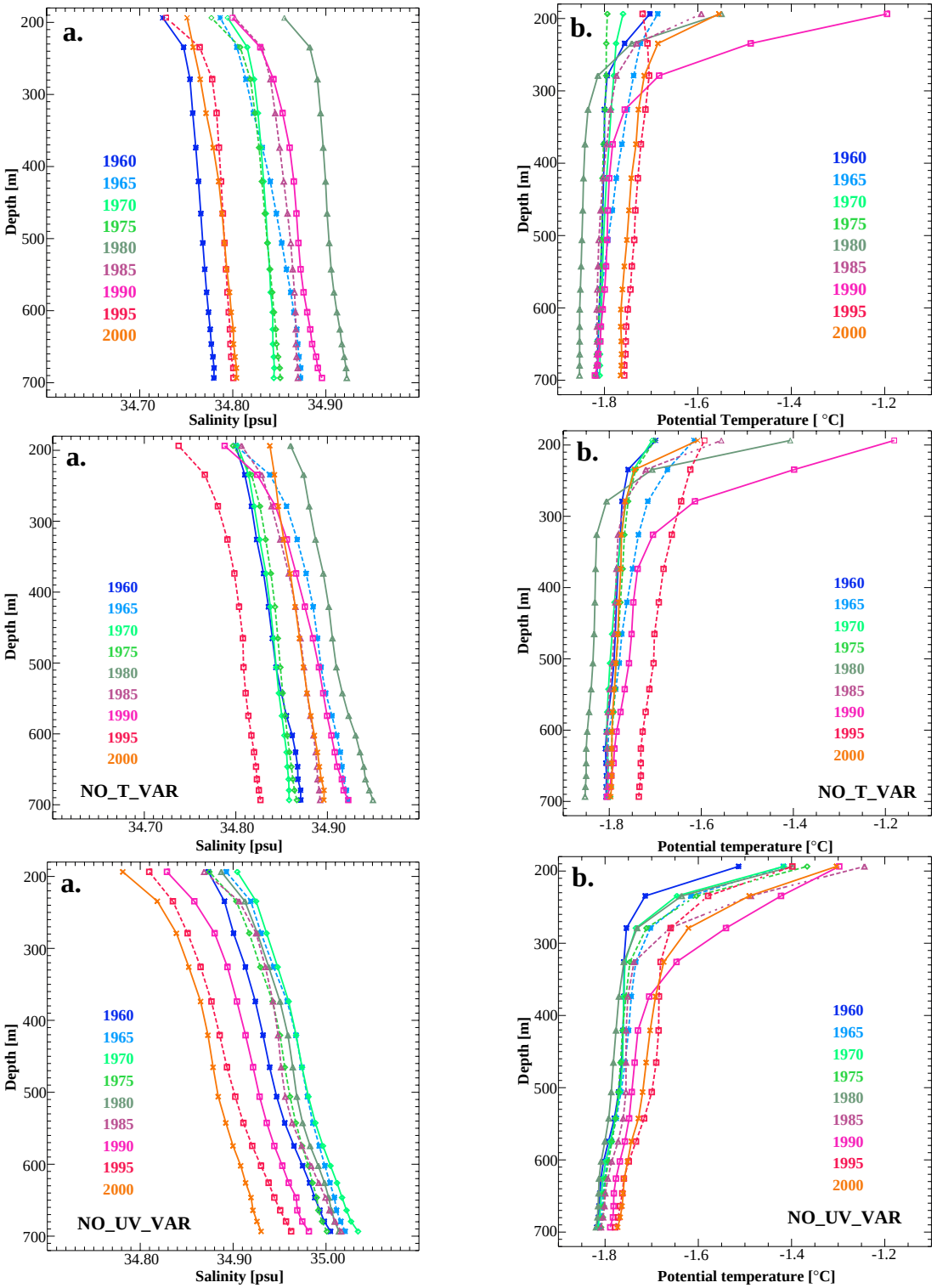

Figure 6.7: Simulated **a.** salinity and **b.** potential temperature profiles below 200 m north of Ross Island. February profiles at 5-year intervals are shown for the years colour-coded. Results for the reference simulation are shown again in the top row for ease of comparison.

respectively, are compared to the reference experiment with full atmospheric variability.

Wind variability appears to be the source of the shorter term variations and generally seems to be the dominant influence on the interannual variability of Ross Sea dense water. The time series of the reference and NO_T_VAR experiments match each other closely while those for NO_UV_VAR are smoother with a larger seasonal cycle (Fig. 6.6). The variability of dense water volume and HSSW salinity in the standard run appears to be a superposition of a short-term signal induced by wind variability onto a smoother signal with variability on the order of several decades induced by air temperature variability. While the wind induced variability is periodic at 5 - 6 and 9 years, it is hard to tell whether the same applies to the air temperature induced signal. If periodic, the model results suggest a period of $\sim$ 40 years, which is close to the 44-year time period analysed, so this has to remain speculation.

The 5 and 9-year periods also appear in the NCEP winds and air temperature time series for the southwestern Ross Sea. The 9-year period can be found in the meridional wind component (Fig. 6.8 b) and the air temperatures (Fig. 6.9), while the shorter is dominant in the zonal winds (Fig. 6.8 a). As shown before, the winds are mainly directed meridionally in the southwestern Ross Sea which is defined in this study as the area north of the Ross Ice Shelf edge, east of Victoria Land, south of 76°S, and west of 180°. Southerly winds predominate with rare instances of northerly monthly means - there are 4 occurences of 1-2 month length in the 44-year time period of NCEP winds used (Fig. 6.8 a).

Zonal winds are more variable in sign. While mostly westerly, easterly winds occur frequently in summer with speeds up to 4 m s^{-1} (Fig. 6.8 c). In the synthetic data set zonal summer winds are easterly between December and February, but only with speeds $\leq$ 0.5 m s^{-1}, similar to the long-term mean. Summer events of strong easterlies in the standard and NO_T_VAR runs prevent the sea ice from being driven northeastward and from melting north of the continental shelf. Instead, fresh melt water is added to the water column in the southwestern Ross Sea lowering HSSW salinities the following winter. Since events of strong northeasterly summer winds do not exist in the synthetic data sets of the NO_UV_VAR experiment, HSSW salinities are around 0.15 psu higher than in the other two sensitivity experiments.

The annual mean series of NCEP 2-m temperature for the southwestern Ross

the standard NCEP Reanalysis data for these sensitivity experiments.

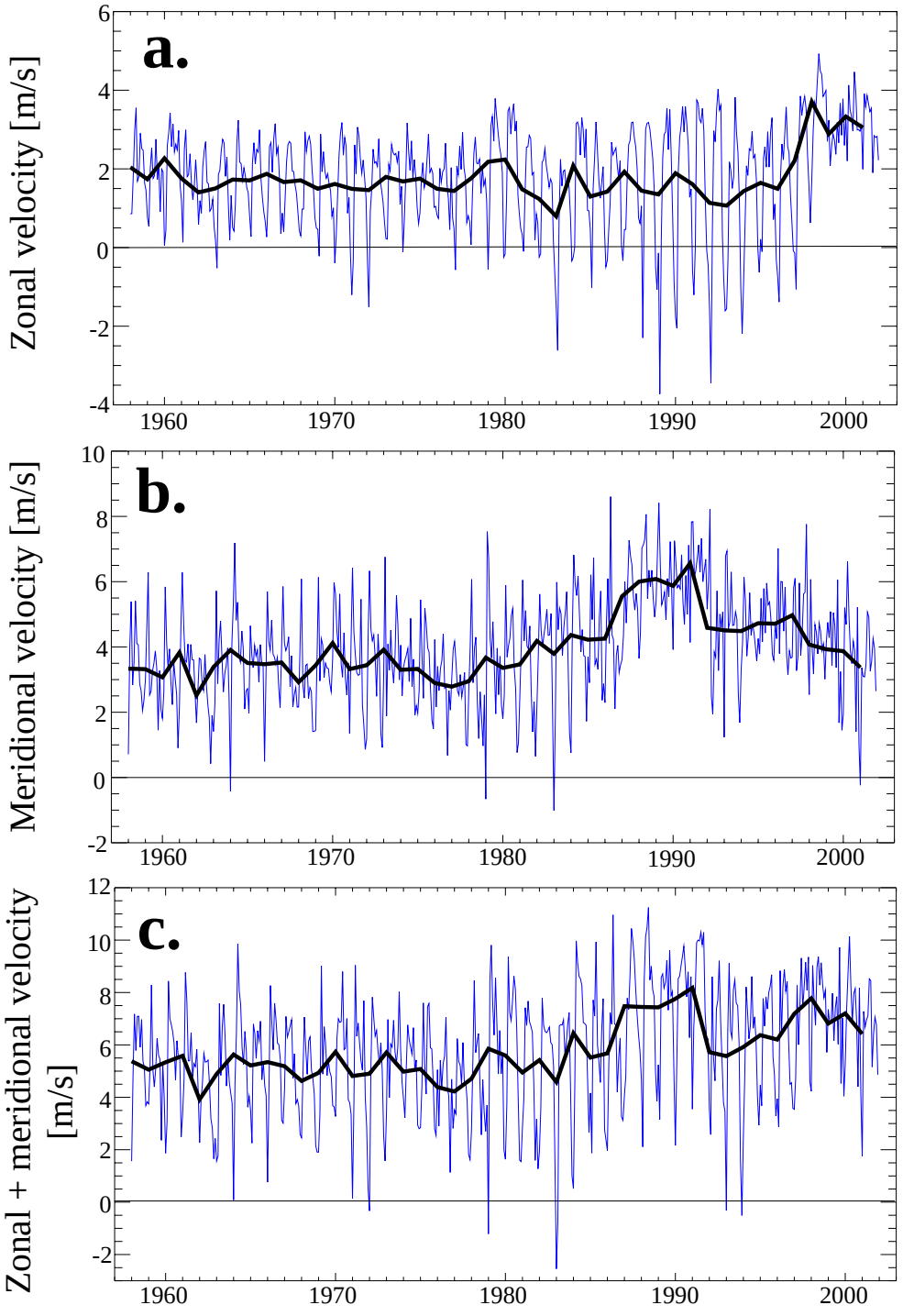

Figure 6.8: Time series of NCEP 10-m wind velocities in the southwestern Ross Sea. **a.** Zonal wind component. **b.** Meridional wind component. **c.** Sum of zonal and meridional wind component. Shown are monthly (thin, blue line) and annual (thick, black line) means. Positive wind velocities denote southerly and westerly winds.

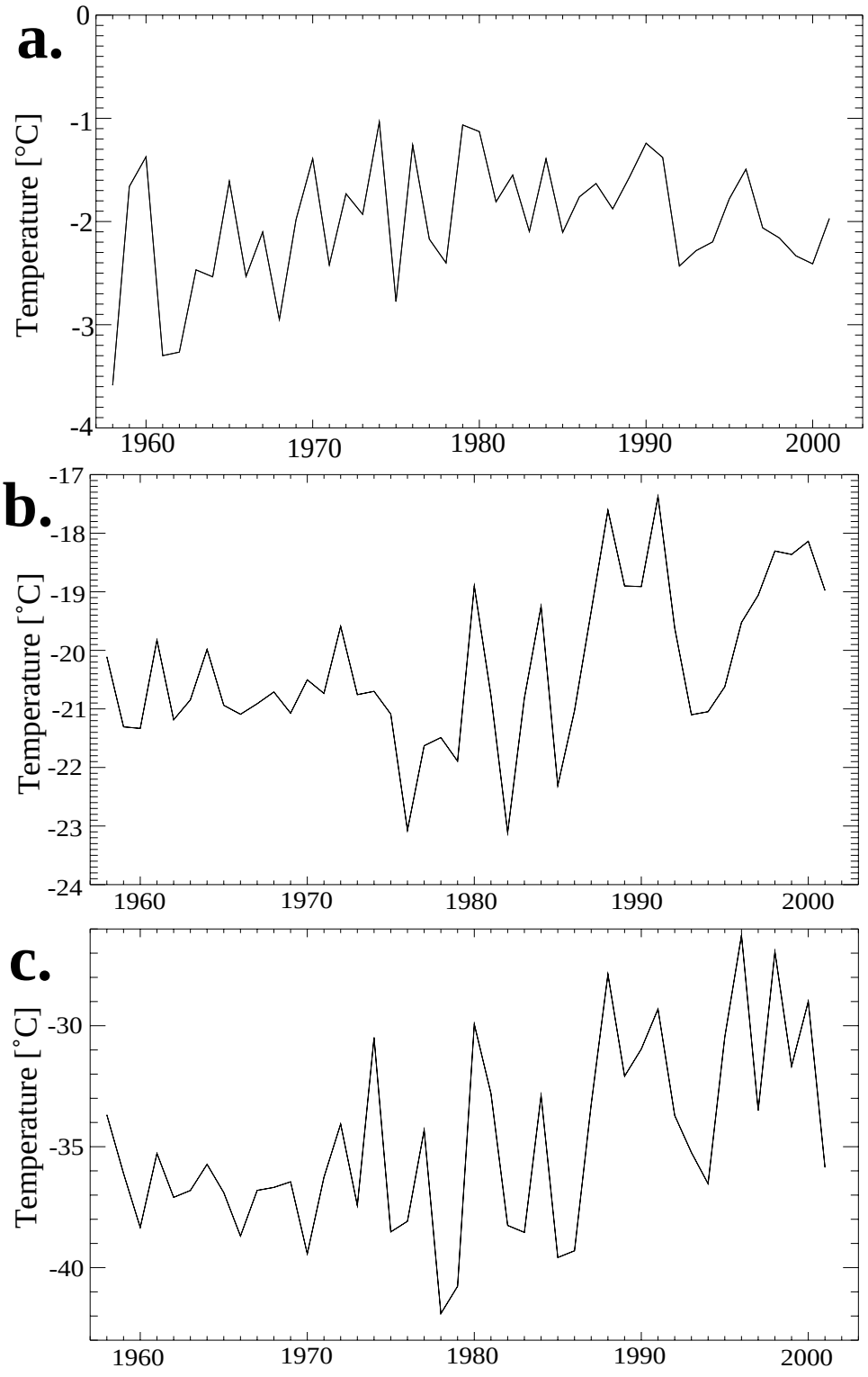

Figure 6.9: Time series of NCEP 2–m air temperatures in the southwestern Ross Sea. **a.** December mean temperatures. **b.** Annual mean temperatures. **c.** August mean temperatures.

Sea (Fig. 6.9 b) shows a positive trend of 0.046°C per year between 1958-2001, significant at the 95% level.[2]

The positive trend is caused by a warming in the winter temperatures from June to October (Fig. 6.9 c). Summer temperatures display no significant trend in January and February temperatures even decrease after 1980. Significant trends are found in December and March - positive in December, negative in March - indicating a shift of the summer period to earlier months. The December increase occurs mainly before 1980 with temperatures leveling out after this point (Fig. 6.9 a).

Salinity and potential temperature profiles sampled at 5-year intervals add information about different levels of the water column (Fig. 6.7). The profiles reflect the general character of the interannual variability identified from the time series. The reference simulation displays the largest range of salinity variability with 0.16 psu, compared to 0.13 psu in NO_T_VAR and 0.1 psu in NO_UV_VAR, i.e. wind and temperature induced variability are of similar magnitude. Similarly, the potential temperature varies considerably less in NO_UV_VAR than in the experiments including wind variability, especially near 200 m where the effect of wind induced mixing and transport is strongest. The warm intrusion around 1990 appears to be wind-induced. Both, the standard and NO_T_VAR simulations, show a sharp ~ 0.08°C rise in potential temperature in the early 1990s, while the NO_UV_VAR run only shows a gradual temperature increase of ~ 0.03°C that extends over almost the entire period investigated (Fig. 6.6 c). Just as wind induced turbulent mixing, transport and vertical current shear cause a larger range of salinity and potential temperature variability, it also helps to transmit these changes vertically leading to a nearly homogeneous water column below 300 m for the reference and NO_T_VAR experiments (Fig. 6.7).

Local fresh-water fluxes are dominated by sea ice formation and melting and its variability (Fig. 6.10). Fresh-water fluxes due to net precipitation and ice shelf basal melting are much smaller with annual means of 4 - 6 mSv. Their range of variation of around 3 mSv is small enough to make them act effectively as a near

[2]Annual means are more variable after the mid 1970s than before (Fig. 6.9). Their standard deviation increases from 0.5°C to 1.6°C with a value of 1.32°C for the entire period. King & Turner (1997) quote a standard deviation of 1.09°C (NCEP 0.96°C) for Scott Base on Ross Island for the period 1958-1984. Their timeseries for Scott Base is similar to the NCEP mean after 1970. This suggests that the temperature variability, especially in winter, is underestimated in the early NCEP Reanalyses and that its representation improves with increasing assimilation of station, ship, and satellite data.

constant source of freshwater with the only fresh-water variability imposed by the sea ice. Hence, the analysis of the local fresh-water and atmospheric variability on the Ross Sea continental shelf will concentrate on the sea ice fresh-water flux. A few comments should be made, however, about the fresh-water flux due to melting at the Ross Ice Shelf base. The results from the standard and sensitivity runs suggest that there is a strong dependence of ice shelf basal melting on wind variability (Fig. 6.10 c). As demonstrated in Section 4.4, melting at the ice shelf front contributes about 40 % to the total basal mass flux of the Ross Ice Shelf cavity with large summer peaks seen in Fig. 6.10 c caused by warm summer surface waters coming in contact with the ice shelf base. In summer, winds can act on the sea surface unperturbed by sea ice and drive warm surface waters southwestward towards the ice shelf front. Even in the inner cavity, a summer maximum in the basal melt rate appears due to a wind-driven inflow (see Section 4.4). Since the annual mean basal melt rate is dominated by this summer peak, the lack of wind variability in NO_UV_VAR explains the near constant annual mean basal melt rate in this experiment. Thus, these sensitivity studies prove the importance of wind fluctuations for determining the variability of sub-ice shelf basal melting.

The southwestern Ross Sea is enclosed by boundaries of land and ice shelf to the south and west. Thus, southwesterly winds lead to a divergent ice pack and strong sea ice formation, while winds with an easterly zonal component have the opposite effect. To decide whether wind conditions are favourable for sea ice formation and brine release or not, the wind components were added, rather than calculating the wind speed (Fig. 6.8 c).[3]

For the reference simulation, there is a good negative correlation (r=-0.67) between the sum of the zonal and meridional wind components and the sea ice fresh-water flux, i.e., strong southwesterly winds cause a large negative fresh water flux and strong brine release. For monthly means, correlations, significant at the 95%-level ($r \leq -0.6$), appear between April and October with the fresh water flux lagging the winds by one month. There is no significant correlation of fresh-water flux with the sum of the zonal and meridional wind components between November and March when air and ocean surface temperatures approach the freezing point. In November, December, and March, however, a positive cor-

[3]Both westerly and southerly winds are defined to have positive wind speeds. Hence addition of the wind components leads to large positive values for southwesterly and large negative values for northeasterly winds.

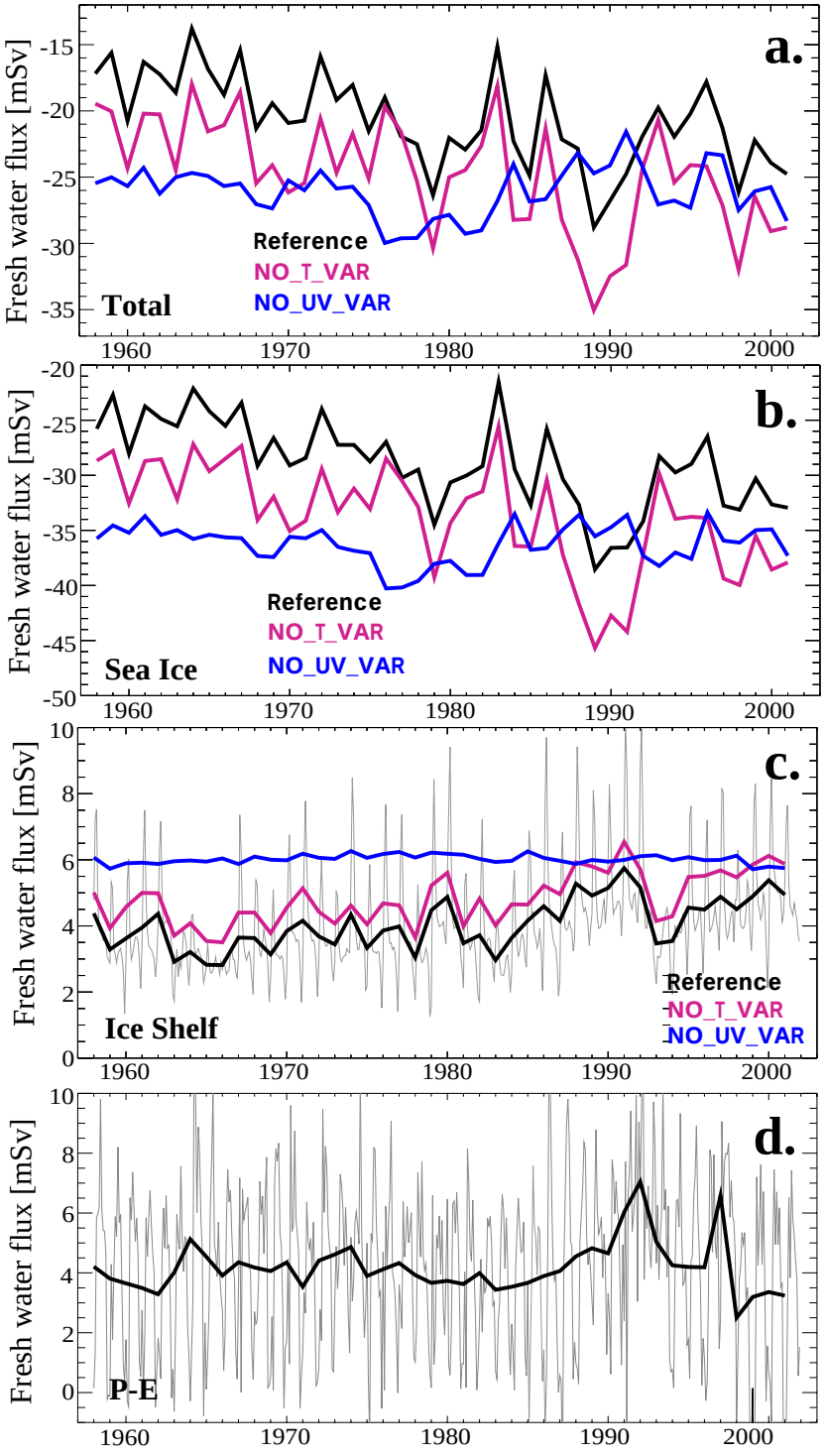

Figure 6.10: Timeseries of modelled freshwater fluxes on the Ross Sea continental shelf (bottom depth $\leq$ 1000m). **a.** Total freshwater flux. **b.** Freshwater flux due to sea ice production and melting. **c.** Basal mass flux in the Ross Ice Shelf cavity, annual means (thick lines) and monthly means for the reference simulation (thin black line). **d.** NCEP net precipitation, annual (thick line) and monthly means (thin line).

relation with air temperatures is found to be significant at the 95% level. The onset of melting and freezing during this period is determined by air temperatures approaching the freezing point and warming or cooling the ocean surface.

However, there is no significant correlation between the annual time series of air temperature and sea ice fresh-water flux. Instead, wind variability appears to be the dominant influence on the interannual variability of the fresh-water flux due to sea ice. In NO_T_VAR, i.e., without temperature variability, the correlation between annual means of wind strength and sea ice freshwater flux rises to r=-0.81. The strong dependence of the sea ice fresh-water flux on the winds confirms that the Ross Sea polynya is predominantly a latent heat polynya. Only in NO_UV_VAR does the air temperature variability have a significant influence on the sea ice fresh-water flux, again mainly in spring and autumn and not reflecting the increase in the variability of NCEP air temperatures after 1978.

Surprisingly, there is no significant correlation between the sea ice fresh-water fluxes and HSSW salinities in any of the three experiments (Fig. 6.6 b & 6.10 b). Since changes in the sea ice fresh water flux are small ($\sim$ 6 mSv) in NO_UV_VAR, this result might be expected in this case. However, wind induced changes in the other two experiments represent a considerable proportion of the annual mean sea ice freshwater flux. Strong peaks in brine input around 1980 and 1990, and minima in the mid-80s and 90s correspond to maxima and minima in HSSW salinity, but the relative amplitude of the fresh water extrema is not reflected in the salinities. The annual cycle of sea ice freshwater flux has an amplitude of $\sim$ 150 mSv (Fig. 4.11) and translates to a seasonal salinity change of around 1 psu at the model sea surface. Fig. 6.6 b shows that this seasonal cycle is damped to around 0.1 psu below 300m. Year-round observations in McMurdo Sound reveal a similar attenuation of the seasonal salinity signal within the water column from 0.8 psu at the surface to 0.2 psu below 300m (Tressler & Ommundsen 1962).

The maximum sea ice freezing rate occurs in April when the continental shelf is mostly ice-free or ice concentrations are low. Thus the wind-driven surface currents are still strong (4 - 5 cm s^{-1}), advecting much of the peak salinity signal out of the area where HSSW is formed, before convection reaches its full strength. Hence, the interannual variability of the freshwater flux is already attenuated in the surface layer. Since even the large seasonal cycle of sea ice induced salinity variation is reduced significantly towards greater depths, the much smaller interannual variations are altered almost beyond detection.

It can be concluded that the variability of local fresh-water input does not trigger

the dense water variability on the Ross continental shelf, but only raises the salinity to the level associated with HSSW within the seasonal cycle. Instead, the interannual variability seems to have its origin in a remote source and is carried onto the continental shelf with the inflowing waters.

6.3 Variability of the continental shelf inflow

In Section 4.3 it was concluded that fresh-water import with the coastal current onto the Ross Sea continental shelf balances the 18 mSv of net fresh water extraction calculated in a budget of the local fresh-water sources and sinks. Consequently, the shelf inflow appears to be a strong candidate to carry the signals of interannual salinity and potential temperature variability onto the Ross Sea continental shelf.

Commonly, the continental shelf is defined as the area with bottom depths of less than 1000 m. Thus, the continental shelf break is defined as the 1000 m isobath for this study and the variability of water flowing onto the shelf across this line taken to represent the inflow characteristics and variability. The continental shelf break was split into a western part from Cape Adare to Pennell Bank, a central part that runs almost meridionally along the eastern side of Pennell Bank, and an eastern part that extends near-zonally to Cape Colbeck (Fig. 6.11).

The analysis of Fig. 4.6 in Section 4.2.2 suggests that inflows near the surface are located in the eastern and central parts of the shelf break, while near the bottom flow onto the continental shelf only occurs in the central part of the Ross Sea. To capture the vertical variation within the water column, time series of the mean inflow salinity and potential temperature were calculated for 100 m bins for the eastern and central sections of the continental shelf break.

As for the HSSW, the amplitude of the salinity variability is attenuated towards greater depth in all three experiments (Fig. 6.12). The inflow salinity time series have similar characteristics in their variability as their HSSW counterparts with salinities below 600 m being near homogeneous. Those including wind variability show shorter, periodic signals, while variability of the NO_UV_VAR run again is smoother. Unlike on the continental shelf, the absence of wind variability does not induce an increase in salinity of the inflowing water reflecting the presence of the large volume of CDW.

To quantify the connection between shelf inflow and dense water properties and to identify the depth at which salinity and potential temperature signals are carried

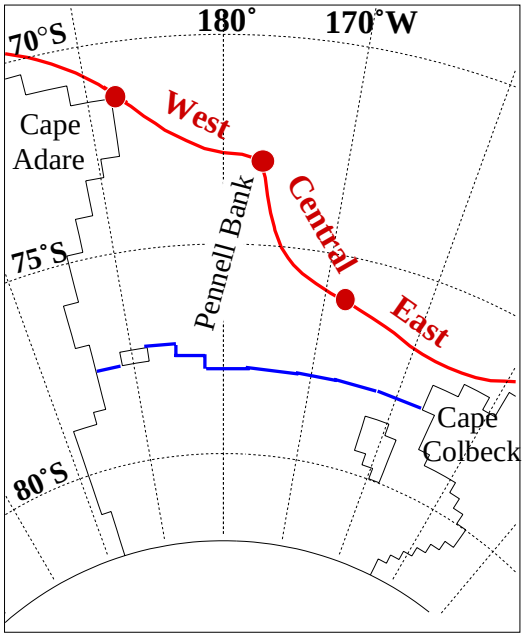

Figure 6.11: Map of the Ross Sea with the 1000 m isobath marked red as represented by the model. Marked by maroon dots are the boundaries of the western, central and eastern sections. The blue line represents the ice shelf front.

onto the continental shelf, a correlation analysis was performed for the eastern and central shelf break segments. Its results are summarised in Table 6.1.

Significant correlations between the inflow and HSSW salinities are found within the top 300 m of both the eastern and central segments of the shelf break in agreement with the main inflow location at this depth. Stronger correlations and shorter lags for the central segment reflect the westward advection of the salinity signal towards the region of HSSW formation. In the previous section the strong attenuation of the seasonal and interannual surface salinity signals due to sea ice formation was mentioned. Much of this attenuation happens in the top 50 m of the water column where wind influence and the associated advection are strongest. Below 100 m the thermohaline-driven and topography guided circulation pattern described in Sections 4.2 and 4.3 gains importance and the correlation loses its seasonal dependence enabling the salinity signal to be transmitted to the HSSW without major attenuation. For the top 100 m, correlations between inflow and HSSW salinitites are strongest in winter when ice cover reduces the wind influence on the surface currents and exchange between the top 100 m and the HSSW is strongest due to deep convection.

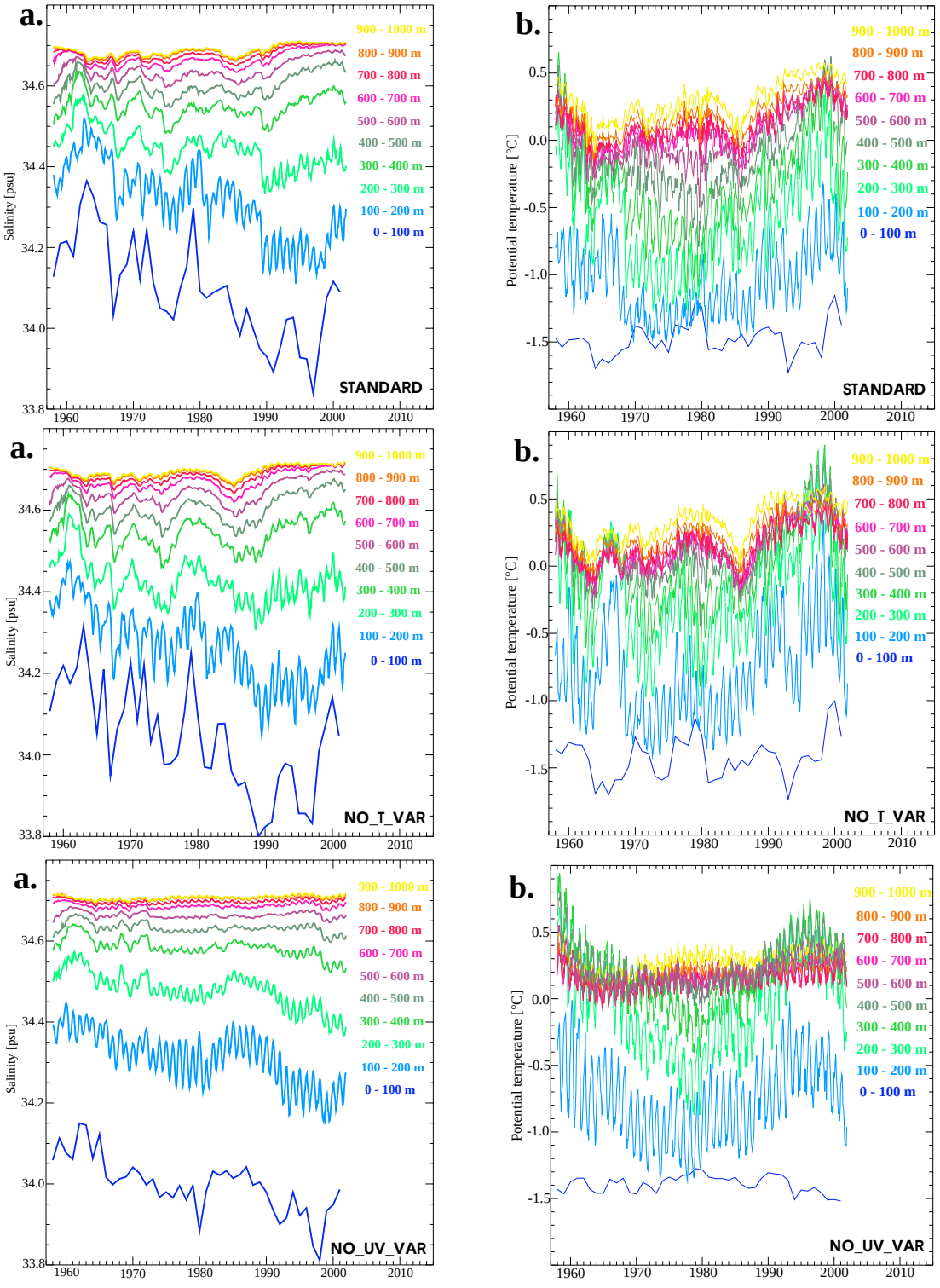

Figure 6.12: Simulated characteristics of the Ross Sea continental shelf inflow: Time series of **a.** salinity for the eastern section and **b.** potential temperature for the central section. Depth is colour coded. For the interval 0 - 100 m annual rather than monthly means are shown.

	Standard		NO_T_VAR		NO_UV_VAR	
	East	Centre	East	Centre	East	Centre
100		0.70(1)	0.50(1)	0.66(1)	0.68(0)	0.80(0)
200	0.56(2) 0.55(0)	0.74(1) 0.61(0)	0.45(1)	0.65(1)	0.77(0)	0.72(0)
300	0.55(2) 0.70(0)	0.64(0)	0.43(1)	0.72(0)	0.74(0)	0.67(0)
400	0.72(0)	0.73(0)		0.76(0)	0.66(0)	0.69(0)
500	0.72(0)	0.79(0)	0.47(0)	0.73(0)		0.75(0)
600	0.70(0)	0.79(0)	0.49(0)	0.64(0)	0.49(0)	0.77(0)
700	0.65(0)	0.75(0)	0.47(0)	0.61(0)	0.49(0)	0.65(0)
800	0.64(0)	0.72(0)	0.49(0)	0.59(0)	0.53(0)	0.58(0)
900	0.64(0)	0.70(0)	0.51(0)	0.59(0)	0.55(0)	0.60(0)
	0.62(0)	0.69(0)	0.51(0)	0.57(0)	0.52(0)	0.59(0)

Table 6.1: Table of correlation coefficients between time series of salinity (blue) and potential temperature (red) at the continental shelf break and in the HSSW. The number in brackets are lags in years, with positive lags denoting HSSW time series lagging behind those at the continental shelf break. All correlation coefficients given are significant at the 95 % level.

Unlike the salinity variability, the potential temperature time series show variability at large amplitudes all through the water column to the bottom (Fig. 6.12). Those for the standard and NO_T_VAR runs show the large warming peak in the 1990s familiar from the HSSW potential temperature series (Fig. 6.6 c). The signal of potential temperature variability is strongest between 300 and 700 m within the core of the coastal current in contrast to the salinity signal which is transmitted above this depth (Fig. 6.1). Consequently, as the inflow to the continental shelf is located in the central shelf break segment for this depth range, correlation for the eastern segment are weaker and reflect the westward advection of the potential temperature signal with the coastal current.

In contrast to the model results, observations (Jacobs et al. 2002) do not show potential temperature variations in the HSSW. In the model, water bearing the

potential temperature signal enters the continental shelf through a trough in the central Ross Sea near the bottom. Potential temperature observations show that Ice Shelf Water (ISW) emerging from the central Ross Ice Shelf cavit extends to the continental shelf break in this region (Jacobs et al. 1970). Mixing of the incoming water with the extremely cold ISW plume probably destroys its potential temperature signal. As mentioned previously, the model underestimates the central ISW outflow from the cavity. This explains the presence of the potential temperature signal in the HSSW as well as modelled HSSW temperatures generally being higher than observed.

Variations of salinity and potential temperature thus enter the continental shelf at different depths, even though both signals appear to originate to the east of the Ross Sea. The inflow signal can be identified clearly in the HSSW characteristics. The interannual variability of dense water characteristics can thus be attributed to a source external to the Ross Sea continental shelf, with local sea ice formation only leading to a salinity enhancement during the seasonal cycle. This seems to contradict the strong anticorrelation of temporal evolution of HSSW salinity and potential temperature (r = -0.71 for the standard run, r = -0.78 for NO_T_VAR and r = -0.90 for NO_UV_VAR), but suggests that both have either a common origin or the one is induced by the other, though the signals then propagate at different depths. Beckmann & Timmermann (2001) propose the existence of a westward travelling bottom potential temperature anomaly within the coastal current and comment on a warm anomaly in the Ross Sea in the 1990s in agreement with the results presented here. Rather than being confined to potential temperatures, there appears to be an equivalent in salinity, which, however propagates close to the surface.

6.4 Origin and propagation of the inflow signal in the Amundsen & Bellinghausen Seas

To get an idea of the propagation paths and the area of origin of the salinity and temperature anomalies that enter the Ross Sea continental shelf two core depths are chosen which were found to carry the characteristic signal responsible for the HSSW variability (cf. Sections 6.2 & 6.3). These are 150 m for the salinity anomaly and 400 m for the potential temperature anomaly. September 1997 was chosen for demonstration purposes, since this month represents winter conditions

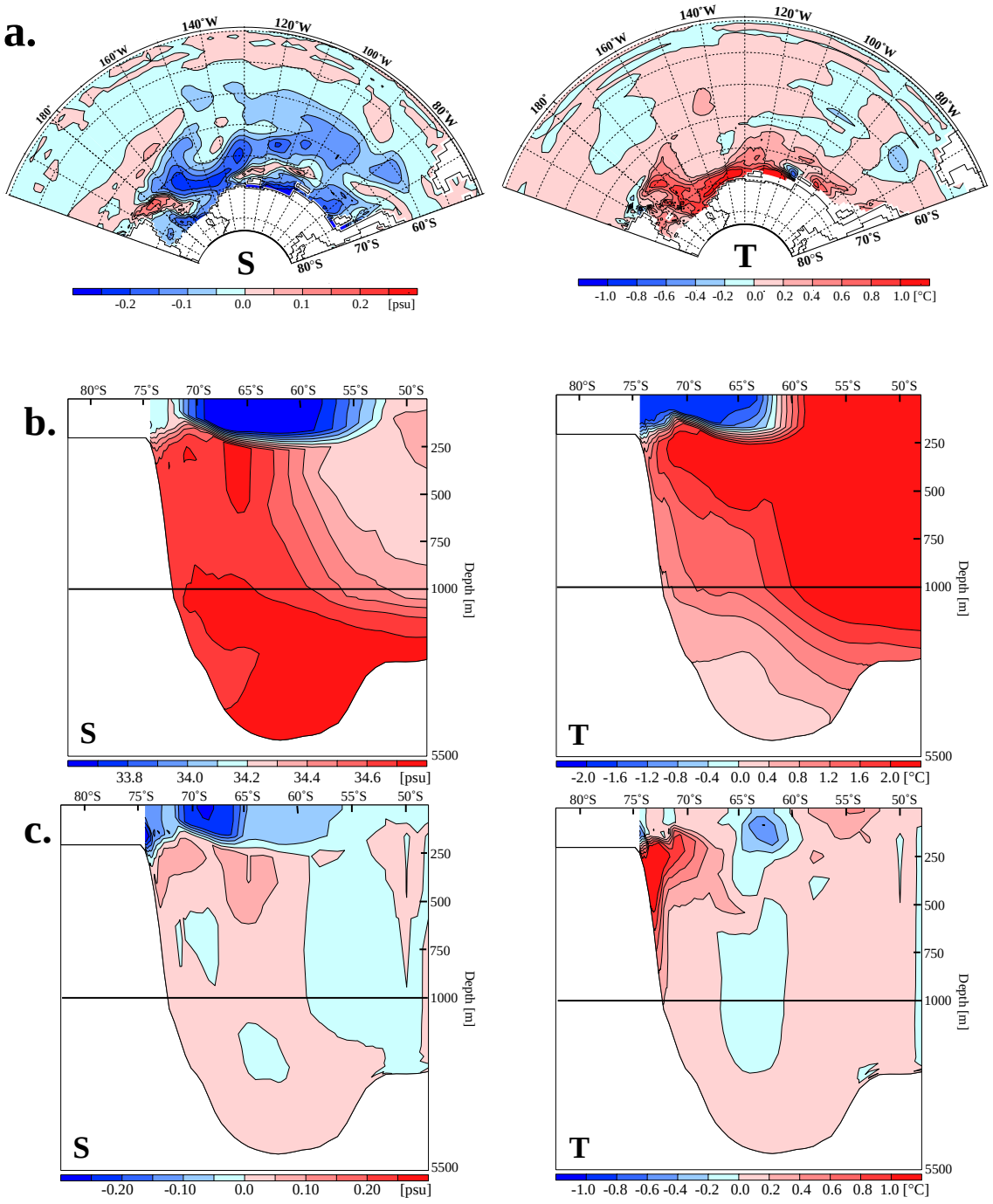

Figure 6.13: For the standard run, monthly mean for September 1997. **a.** Left: Salinity anomaly at 150 m. Right: Potential temperature anomaly at 400 m. **b.** Meridional salinity (left) and potential temperature (right) section along 115°W, i.e. in the central Amundsen Sea. **c.** Salinity (left) and potential temperature (right) anomalies for the same sections. The top 1000 m of the water column is stretched for better visibility in **b.** and **c.**.

at the end of the warm and fresh HSSW anomaly.

The salinity and potential temperature anomalies show the anticorrelation also present in the HSSW signals. Both signals are spread throughout the Amundsen and Bellingshausen Seas (Fig. 6.13 a & c). Their amplitude is largest in the Amundsen Sea close to the coast and is attenuated as they enter the Ross Sea continental shelf.

On a meridional section at 115°W, i.e in the centre of the Amundsen Sea, salinity anomalies with amplitudes ≥ 0.1 psu are confined to the top 200 m in agreement with results found in the previous section at the Ross continental shelf break (Fig. 6.13 c). This layer is subject to a large seasonal cycle and strongly feels the effect of sea ice formation and melting, suggesting that the salinity anomalies are connected to surface fresh water input due to sea ice.

The core of the potential temperature anomalies is located in the southern extension of the CDW which reaches and enters the continental shelf in the Amundsen Sea (Fig. 6.13 c). Amplitudes are large, up to 1.5°C, and reflect how close the warm CDW core approaches the shelf and how much it mixes with colder shelf waters. Fig. 6.13 c shows that the potential temperature anomaly is found close to the bottom on the continental slope between 200 and 1000 m depth, in agreement with the analysis of Beckmann and Timmermann (2001). A northward extension reaches 65°S between 200 and 500 m. CDW salinities are fairly constant just above 34.7 and the amplitude of anomalies at this depth is small (see also Fig. 6.12). Maps of cross-correlation coefficients of the HSSW salinity time series onto salinity at 150 m and of HSSW potential temperatures onto potential temperature at 400 m depth (Fig. 6.14 a & c) shed light on the origin and propagation paths of the HSSW interannual variability signals. Both salinity and potential temperature show a strong positive correlation for zero lag on the southwestern Ross Sea continental shelf where the HSSW formation region is located.

Outside the continental shelf area the salinity and potential temperature signals follow quite different paths (Fig. 6.14). Besides entering the Ross Sea continental shelf part of the salinity signal propagates along the continental shelf break (Fig. 6.14 a). With HSSW salinities lagging those at 150 m by 5 years a significant correlation is confined to the coast in Amundsen and Bellingshausen Seas and to a region between 65°S and 70°S in the Amundsen Sea where $r \geq 0.5$ (Fig. 6.14 b). This indicates that the salinity signal is induced in the Amundsen and Bellingshausen Seas and puts a timescale of around 5 years to the propagation of the

salinity signal from its origin to the Ross Sea in agreement with estimates from current speeds at this depth.

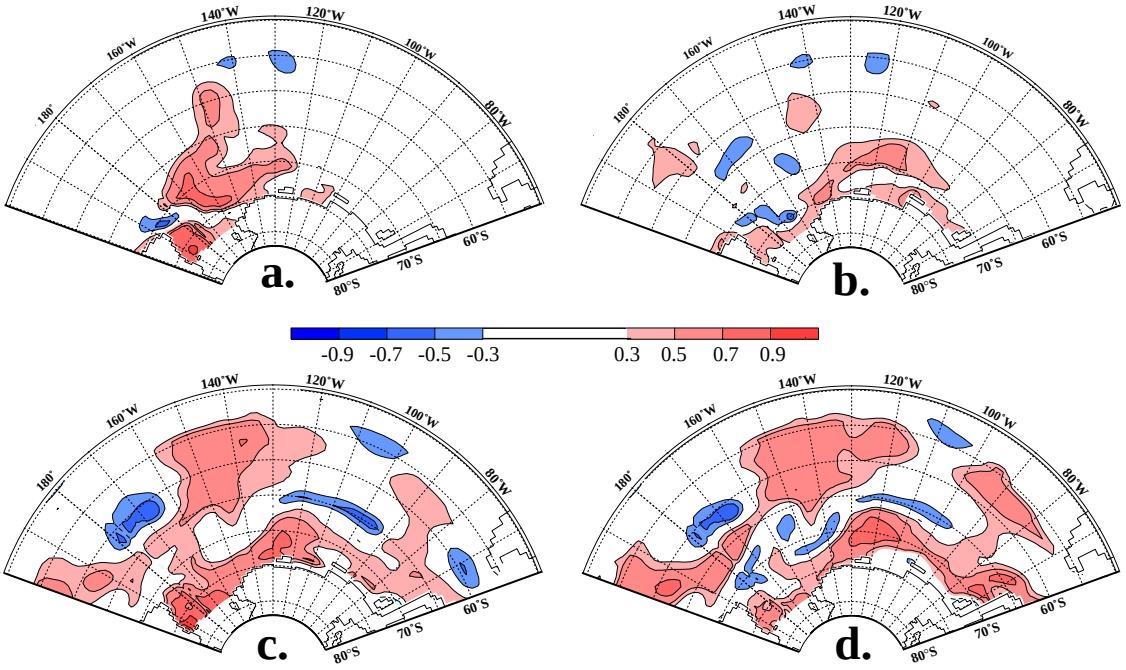

Figure 6.14: Cross-correlation maps for annual means of **a.** HSSW salinity onto salinity at 150 m depth, zero lag, **b.** HSSW salinity onto salinity at 150 m depth, 5-year lag, **c.** HSSW potential temperature onto potential temperature at 400 m depth, zero lag, **d.** HSSW potential temperature onto potential temperature at 400 m depth, 5-year lag. Correlation coefficients r $>$ $\pm$ 0.5 are significant at the 99 % significance level.

In contrast to the closely confined salinity signal, the temperature signal can be identified in large parts of the basin. For both zero and 5-year lags good correlations are found in the Amundsen Sea in the same region where correlation coefficients $>$ 0.5 were found for salinity and which corresponds to the centre of the Ross Gyre extension (Fig. 6.14 c & d). Noteworthy are also large areas of significant correlation around 60°S in the Bellingshausen and eastern Ross/western Amundsen Seas. Both indicate propagation paths of the signal apart from that onto the Ross Sea continental shelf. As with the salinity signal, the potential temperature signal follows the western branch of the Ross Gyre north. The signal also propagates eastward towards the Antarctic Peninsula and through Drake Passage. The current pattern at 400-m depth is still influenced by that at the surface (cf. Fig. 4.5 a) and velocities in the Bellingshausen Sea are directed north-

eastward carrying the potential temperature signal northward into the ACC and eastward around the Antarctic Peninsula. The amplitude of potential temperature anomalies are small, however, in both of these areas due to mixing processes acting in the fast-flowing ACC regime.

The cross-correlation maps in Fig. 6.14 also confirm the path salinity and potential temperature anomalies take onto the Ross Sea continental shelf postulated in Section 6.3. The salinity anomaly propagates close to the coast between 150°W and 170°W south of the eastward flowing Southern Ross Sea Counter Current to enter the continental shelf at its eastern end. At 400 m and hence well within the influence of the bottom-intensified westward flow of the coastal current the potential temperature signal is advected onto the shelf both in the eastern and central Ross Sea.

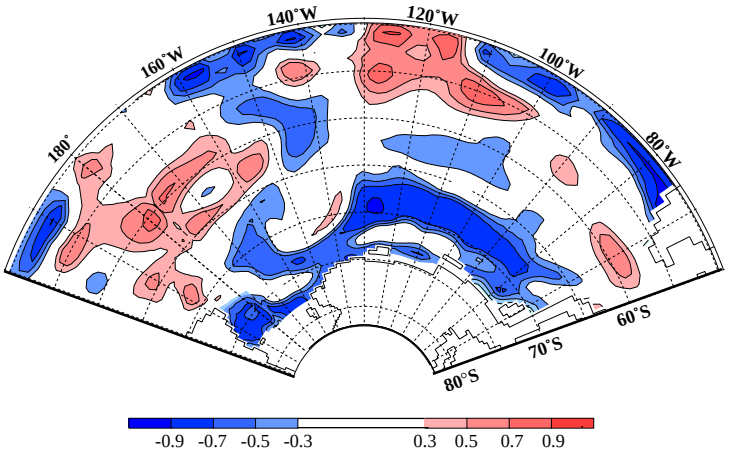

Figure 6.15: Crosscorrelation map of salinity at 150 m and potential temperature at 400 m for annual means, zero lag. Correlation coefficients r $>$ $\pm$ 0.5 are significant at the 99 % significance level.

The idea that salinity and potential temperature variability are connected despite their propagation at different depth and that the connection is established in the Amundsen Sea is confirmed by a crosscorrelation of salinity anomalies at 150 m and potential temperature anomalies at 400 m. Strong correlations (r $>$ 0.7) exist in the Amundsen Sea and extend into the Bellingshausen Sea between 65°S and 70°S (Fig. 6.15). They also trace the propagation path of the salinity signal onto the Ross Sea continental shelf close to the coast and show the northeastward advection of the signals with the western limb of the Ross gyre. The correlation breaks down in the region of the Southern Ross Sea Counter current where water

with a different salinity signature is advected southeastward.

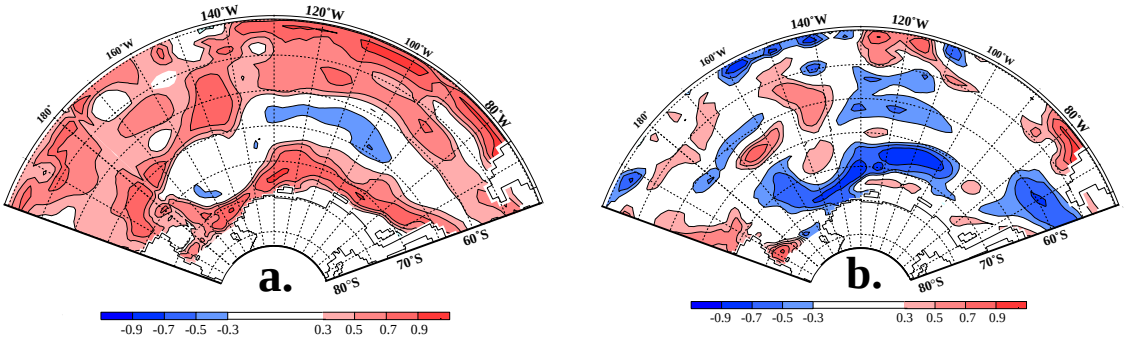

Figure 6.16: **a.** Crosscorrelation map of potential temperature at 150 m and at 400m for annual means, zero lag. **b.** Crosscorrelation map of salinity at 150 m and at 400m for annual means, zero lag. Correlation coefficients r $> \pm$ 0.5 are significant at the 99 % significance level.

The physical mechanism that establishes the connection between subsurface salinities and potential temperatures at 400 m and their causal connection is yet unclear. The region of interest, the Amundsen Sea between 65°S and 70°S and 110°W and 130°W, is located within the marginal sea ice zone, near the sea ice edge (Fig. 3.1 c) where strong anomalies of sea ice concentration and growth rate exist. Convection during the sea ice growth season would hence be a likely candidate for a vertical exchange mechanism between 150 m and 400 m. A negative anomaly in brine release would lead to lower salinities in 150 m depth, a more stable water column, and hence to higher temperatures in 400 m depth, or vice versa. While potential temperatures at 150 m and 400 m are positively correlated (Fig. 6.16 a), salinities at both depths show a negative correlation (Fig. 6.16 b). However, the model's parameterisation of vertical mixing is identical for salinity and potential temperature and so salinity and potential temperature should show a correlation of the same sign. Since salinities at 400 m are not affected by subsurface salinities, potential temperatures at 400 m cannot be determined by convective mixing of surface and subsurface signals to this depth.
The area of interest in the Amundsen Sea coincides with the centre of the Ross Gyre extension (Fig. 4.3). Upwelling of warm CDW in the gyre's center hence presents a mechanism for signals at 400 m depth to propagate upward towards the surface. The positive correlation of potential temperatures at both depths agrees with this hypothesis. The amplitude of salinity anomalies at 400 m depth

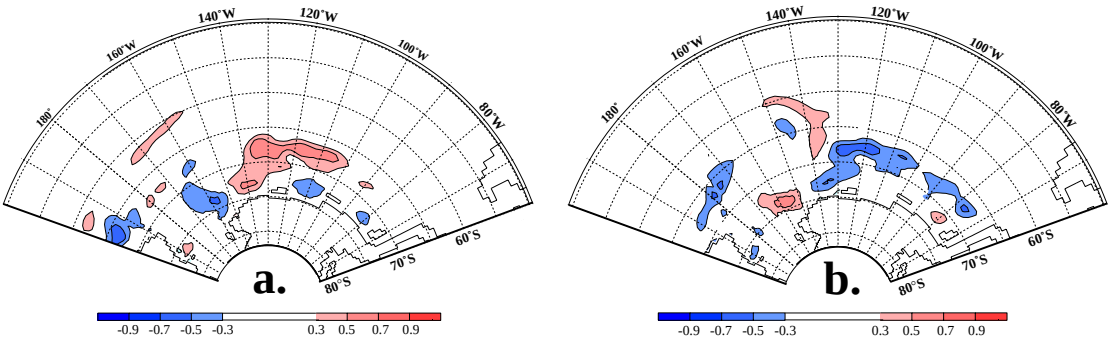

Figure 6.17: **a.** Crosscorrelation map between annual means of salinity at 150 m and September sea ice growth rates. **b.** Crosscorrelation map between annual means of potential temperature at 400 m and September sea ice growth rates.

is small (Fig. 6.13 c). Thus, larger amplitude salinity anomalies induced at the surface could cancel their effect. Surface and sub-surface salinity anomalies are induced by winter sea ice growth (or melting) anomalies at the sea ice edge. Fig. 6.17 a demonstrates that the northern Amundsen Sea between 65°S and 70°S is the only area where sea ice growth rate anomalies and sub-surface salinities at 150 m show a significant positive correlation. Fig. 6.17 b establishes a negative correlation between potential temperatures at 400 m depth and sea ice growth rate anomalies, i.e., higher temperatures are linked to lower sea ice growth or stronger melting. In both cases corrrelation coefficients are lower than those found between the two ocean depth layers, but reasonable, if advection of surface waters, attenuation of the sea ice fresh water signal near the surface, and large atmospheric variability are taken into account. The coastal easterlies lead to an onshore Ekman transport which results in downwelling at the continental shelf break, thus preventing upward heat flux from the core of the temperature anomaly (Fig. 6.13 c) from affecting the sea ice cover.

The physical mechanism linking the subsurface salinity anomalies and the potential temperature anomalies at 400 m depth, that determine HSSW salinity and potential temperature on the Ross Sea continental shelf, can thus be summarised as follows: Upwelling of CDW in the Ross Gyre extension's center causes an upward heat flux that reaches the surface at the sea ice edge in the Amundsen Sea. This induces anomalies of sea ice fresh-water flux which lead to sub-surface salinity anomalies of the opposite sign. Both anomalies are advected towards the Ross Sea continental shelf at the relevant depths.

Warm CDW is transported southward between 90°W and 115°W along the east-

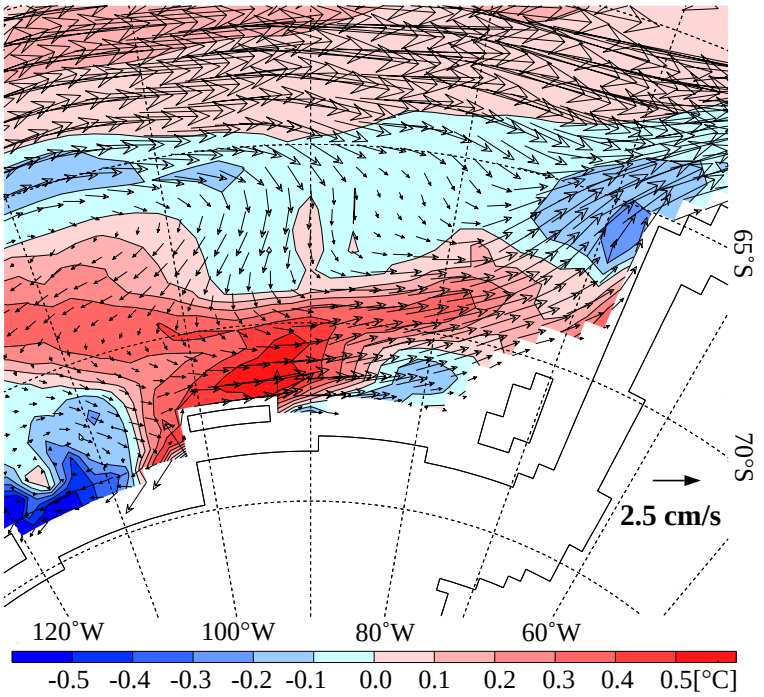

Figure 6.18: Potential temperature anomaly (colour coded) and current velocities (vectors) at 400 m for September 1984 at the start of a warm anomaly in the standard run.

ern end of the Ross Gyre extension at 300-2000 m depth (Fig. 4.3 and Fig. 6.18). Potential temperature anomalies of large amplitude are formed near the coast where warmer CDW and colder shelf waters interact. Potential temperatures at 400 m near the coast in this region are well correlated to the southward transport with r=0.78 for a lag of 1-2 years (Fig. 6.19). The lag reflects the low current velocities of 1-2 cm s^{-1} south of the ACC regime. The faster CDW is transported south towards the western Bellingshausen continental shelf, the less it is cooled and the further south it advects the temperature signal, leading to warm potential temperature anomalies along the continental shelf break. Observed profiles of potential temperature in Pine Island Bay ($\sim$ 100°W, 74°S), a location known for the exceptionally high melt rates of the bordering glacier, show interannual variability of the order of 1.5°C at depths of 200 - 400 m between 1992 and 1994 (Jacobs et al. 1996). These observations confirm the magnitude of the temperature anomalies seen in the model, along with the near constant salinities below 200 m (Fig. 6.13). While the anomalies travel westward towards the Ross Sea within the coastal current, above 600 m they also propagate eastward towards the

Antarctic Peninsula (Fig. 6.18) in agreement with the propagation pattern seen in Fig. 6.14 d. The westward branch forms what Beckmann & Timmermann (2001) describe as the ACCW. At the Antarctic Peninsula the eastward travelling signal might prevent the ACCW that after surrounding Antarctica anti-cyclonically has reached the Weddell Sea to reenter the Bellingshausen Sea. This would indicate an asymmetry in the interaction of the Weddell Sea and the South Pacific Sector of the Southern Ocean.

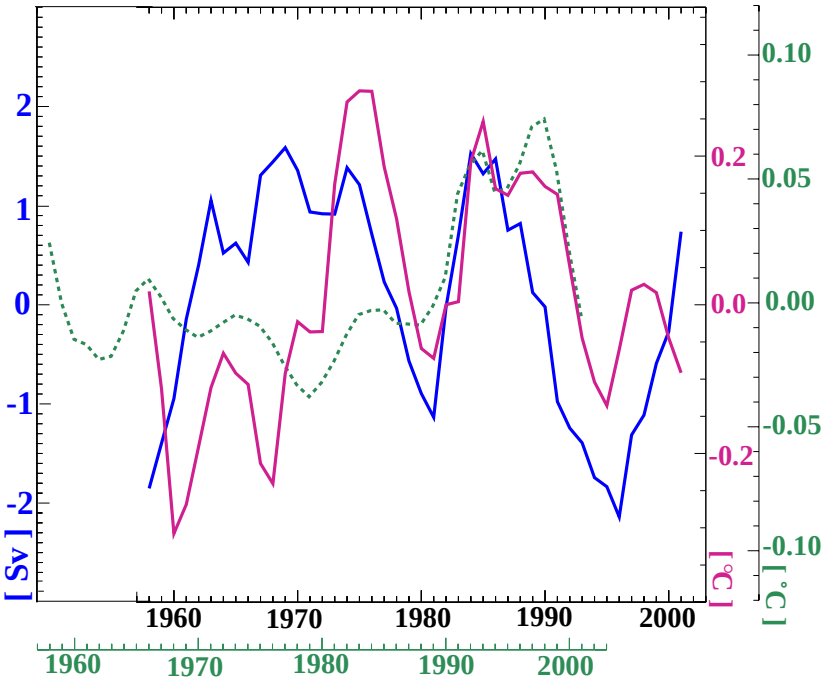

Figure 6.19: For the reference simulation: Time series of monthly means of the meridional transport anomaly between 90°W and 115°W (blue line), of the mean potential temperature at 400 m between 90°W and 115°W, south of 68°S (red line), and of the mean HSSW potential temperature on the Ross Sea continental shelf (green line), all detrended.

Features in the time series of Bellingshausen Sea potential temperature anomalies at 400 m can be identified in the time series of Ross Sea HSSW potential temperature (Fig. 6.19). They suggest a time period of 7-11 years for propagation of the signal from the western Bellingshausen Sea to the Ross Sea continental shelf with signs of possible frequency modulation during the time period analysed.
A comparison of the results from the reference simulation to those from the sensitivity experiments NO_T_VAR and NO_UV_VAR demonstrates that both air temperature and wind variability influence the meridional transport and hence the

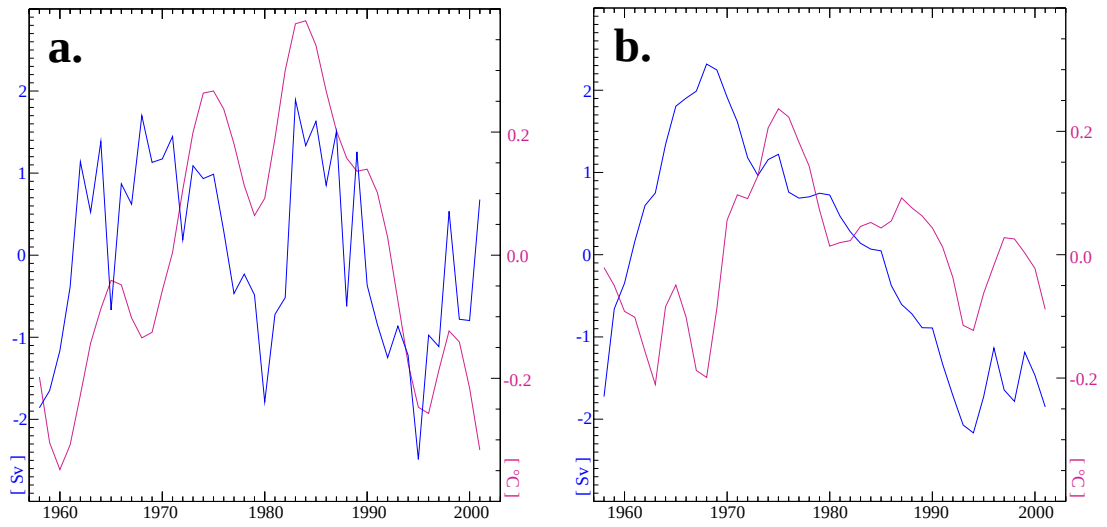

Figure 6.20: Time series of monthly means of the meridional transport anomaly between 90°W and 115°W (blue line) and of the mean potential temperature at 400 m between 90°W and 115°W, south of 68°S (red line), both detrended, for **a.** NO_T_VAR and **b.** NO_UV_VAR.

coastal potential temperature anomalies (Fig. 6.20). Again NO_UV_VAR shows a smoother behaviour than both the standard and NO_T_VAR experiments. The interaction of winds, air temperatures, and meridional CDW transport appears to be complex and are not obvious. However, analysis of the characteristic periods of variability allows some insight in the interaction between atmosphere and ocean. As on the Ross Sea continental shelf dominant periods of variability can be found at 5-6 years and 7-11 years. Also a longer period of 15 years is present in the zonal winds which affects the meridional transport along the eastern edge of the Ross Gyre extension and the associated potential temperatures. In Section 5.4 a similar period was identified in the zonal Amundsen sea ice transport and winds. A shorter period of 3-4 years as well as that at $\sim$ 6 years is present in both wind components and air temperatures and, hence, in the transport and potential temperature series of all three experiments. Venegas (2003) interprets the pattern of the Antarctic Circumpolar Wave (White & Peterson 1996) as a superposition of a wavenumber 3 signal at the shorter period and a wavenumber 2 pattern at the longer which appears to have a connection to the tropical ENSO-phenomenon. Variability at the lower end of the 7-11 year period band is carried by the meridional winds whose 7 year period can be found in the meridional transport time series of the standard run and NO_T_VAR. The 11-year period

is found in the NCEP air temperatures and again in meridional transport, 400 m potential temperatures, and Amundsen Sea 150 m-salinities in the standard and NO_UV_VAR runs. Frequency modulation during the advection towards the Ross Sea continental shelf and a dominant local period of 9 years in air temperature and winds result in the HSSW variability pattern found on the Ross Sea continental shelf.

6.5 Summary

Salinity, potential temperature and volume of the High Salinity Shelf Water (HSSW) formed in the western Ross Sea show oscillatory behaviour at periods of 5-6 and 9 years superimposed on long-term fluctuations. While the shorter oscillations are induced by wind variability, variability on the scale of decades appears to be related to air temperature variability. It was demonstarated that decrease of HSSW salinities deduced from observations (Jacobs et al. 2002) may be an aliasing artifact of an oscillatory pattern as found in the model results.
While consistently high sea ice growth rates in the Ross Sea polynya are quintessentially responsible for the high salinities of the HSSW, interannual variability of the local sea ice fresh water fluxes is not the origin of the variability signal found in HSSW salinities. Both, the salinity and potential temperature signals, were found to be introduced to the Ross Sea continental shelf with the inflowing water masses. The salinity signal propagates on the sub-surface between 100 and 300 m while the potential temperature signal appears below 200 m down to the bottom within the CDW carried with the coastal current.
The subsurface salinity signal forms in the Amundsen Sea along the winter sea ice edge between 65°S and 70°S. Upwelling of CDW that carries the potential temperature anomaly in the centre of the Ross Gyre extension influences the oceanic heat flux leading to anomalies in sea ice fresh-water flux which cause the sub-surface salinity anomalies. Thus salinity and potential temperature signals are clearly anticorrelated and displaced in depth.
The potential temperature anomalies arise from anomalies in the southward transport of CDW with the eastern end of the Ross Gyre extension in the western Bellingshausen Sea. While part of the anomaly is carried eastward towards the Antarctic Peninsula at depths of 300 - 800 m, the signal is also carried westward along the continental shelf break towards the Ross Sea and forms the beginning of the pattern decribed as the Antarctic Circumpolar Coastal Wave (Beckmann &

Timmermann 2001). Meridional transport variability along the eastern end of the Ross Gyre extension shows signs of both interannual wind and air temperature variability, but a clear correlation is not obvious.

Chapter 7

Conclusions & Outlook

This work presents a thorough investigation of the factors affecting dense water formation on the Ross Sea continental shelf and their variability. It establishes links between the Ross Sea continental shelf as the dense water formation site and the Amundsen and Bellingshausen Seas as source regions of both sea ice and water masses entering the Ross Sea continental shelf. Since previous investigations have concentrated on detailed investigations of processes and conditions on the Ross Sea continental shelf, this work presents the first attempt to locate the causes of interannual variability on the continental shelf in the upstream regions of the Amundsen and Bellingshausen Seas.

The research tool employed is the coupled sea ice-ice shelf-ocean model BRIOS2.2 which is a further development of the model presented by Timmermann et al. (2002 a & b) who applied it to the Weddell Sea. However, due to their research focus on the Weddell Sea, model resolution in the Pacific sector was very coarse and thus did not allow a detailed description of its sea ice and ocean regime. The isotropic model resolution which had proved to be sufficient for a reasonable representation of sea ice and ocean conditions in the Weddell Sea was extended to the entire circumpolar domain and the land mask adjusted carefully in the Pacific and Indian sectors. Inclusion of smaller ice shelves in the Amundsen and Bellingshausen Seas allows for a more realistic representation of water mass characteristics in this region and the use of NCEP instead of ECMWF reanalysis data as atmospheric forcing for the investigation of variability of the ice-ocean system in recent decades. Extensive validation with the available data base shows that the model BRIOS2.2 is able to provide a highly reasonable representation of ocean and ice conditions in the Pacific sector of the Southern Ocean. Deficien-

cies could largely be attributed to inadequacies in the NCEP forcing data or to insufficient horizontal resolution.

The model reproduces the recent sea ice retreat in the Bellingshausen Sea retrieved from satellite observations (e.g. Zwally et al. 2002). Causes for this retreat have been identified as an increase in air temperature, increasingly westerly zonal winds, and a shift from predominantly southerly to more northerly meridional winds. The Bellingshausen Sea ice is highly insensitive to even a strong increase in net precipitation because of its, for Southern Ocean standards, highly stable ocean stratification. The decrease in meridional winds over the last four decades is also found in the Amundsen Sea and leads there to sea ice thickening along the coast, but the sea ice retreat is confined to the Bellingshausen Sea East of 100°W. A combined analysis of model results and sea ice drift buoy data demonstrates that the westward sea ice drift along the coast in the Amundsen Sea is predominantly wind-driven while in general ocean influence is small. Daily to weekly variability of zonal and meridional ice velocities is dominated by the zonal winds, consistent with the predominantly zonal drift pattern and higher zonal wind velocity coherence. For the region south of 70°S, model results indicate that roughly half of the sea ice generated in the Amundsen Sea is exported into the eastern Ross Sea. Transport into the Ross Sea depends on the interplay between the strength of zonal winds, location of the transition between easterlies and westerlies, and variable northward transport by meridional winds.

Sea ice volume and growth rates in the eastern Ross Sea are strongly influenced by the amount of sea ice imported from the Amundsen Sea. In the western Ross Sea ice characteristics are determined predominantly by the local atmospheric and oceanic conditions. Thus, it appears that, regarding sea ice conditions, the western and eastern Ross Sea are decoupled from each other. However, the import of Amundsen Sea ice into the eastern Ross Sea and the eastern Ross Sea ice thicknesses both show a strong positive correlation to northward ice export from the western Ross Sea. It appears that in the Ross Sea removal of locally formed sea ice is necessary for the intrusion of Amundsen Sea ice to take place. The sea ice regime of the western Ross Sea with its mostly locally formed sea ice and fast northward drift thus seems to be highly independent of the influence of remote sources of variability. Its interannual variations are determined by the local atmospheric conditions.

Strong brine release in the Ross Sea polynya and comparatively low fresh water addtions due to ice shelf basal melting and net precipitation leave the Ross Sea

continental shelf with a negative fresh-water budget. It is closed by a relatively fresh sub-surface inflow ($\sim$ 34.3) from the Amundsen Sea. This shallow inflow of low salinity waters manipulates the characteristics of dense shelf waters as one of the two sources of High Salinity Shelf Water (HSSW) in the southwestern Ross Sea by damping the brine signal from sea ice growth towards greater depth. Here it densifies the second source of HSSW, the deep water upwelled onto the continental shelf as proposed by Killworth (1974) and Toggweiler & Samuels (1995).

The strong warming of summer surface water on the generally ice-free Ross Sea continental shelf results in strong melting of the ice shelf front. Representing $\sim$ 40 % of the entire fresh-water flux due to ice shelf basal melting this summer peak dominates the seasonal cycle of basal melting for the entire cavity and is still apparent in that of the inner cavity where a bimodal seasonal cycle exists with a second peak in melt rate due to increased cavity ventilation in winter. As the summer surface circulation outside the cavity, the basal melt rate of the entire cavity thus depends on the winds and their interannual variability. It was shown that the region around Ross Island and McMurdo Sound has a key role in controlling the exchange between the ice shelf cavity and the open ocean in the Ross Sea. Freshwater outflow from McMurdo Sound is responsible for the dome structure in the salinity distribution along the ice shelf edge in the western Ross Sea. Drainage of HSSW through McMurdo Sound into the cavity in winter prevents brine accumulation and thus lowers HSSW salinities to the range observed. Prohibition of HSSW drainage along the Victoria Land coast leads to a weakening of the central Ice Shelf Water (ISW) outflow. Since both HSSW and ISW are parent water masses for the formation of Antarctic Bottom Water (AABW), this possibly affects the balance of the two sources of AABW in the Ross Sea.

Two processes have previously been proposed as the governing factors for the formation of highly saline shelf waters and their interannual variability. The generally accepted hypothesis states that the salinity of these shelf waters is determined by the amount of brine release due to sea ice formation (e.g. Comiso & Gordon 1998). In a contrasting hypothesis Toggweiler & Samuels (1995) propose that the effect of sea ice fresh water fluxes is generally overestimated and that inflow salinities play a role at least as important in the formation of dense shelf waters. This investigation shows that sea ice fresh-water fluxes certainly play an important role in shaping circulation, and water mass characteristics and

distribution on the Ross Sea continental shelf. The characteristic sea ice pattern of fast northward drift and strong brine release in the western and more sluggish drift of sea ice partially imported from the Amundsen Sea and resulting lower growth rates in the eastern Ross Sea is remarkably steady during the 44-year period analysed. The zonal salinity gradient reflects the gradient in seasonal sea ice fresh-water flux with the density maximum consistently located on the western continental shelf where the Ross Sea polynya is a persistent feature. The shelf circulation is to a considerable part driven by this zonal salinity gradient. Its steepening of causes an increase of the transport of the anticyclonic circulation cell that occupies the western shelf and ice shelf cavity both on a seasonal and interannual time scale.

The existence of a similar thermohaline forcing mechanism of the shelf and cavity circulation was demonstrated by Timmermann et al. (2002 b) for the Weddell Sea. As well as identifying that changes in the circulation regime on the shelf and in the ice shelf cavity are caused by changes in the location of the density maximum on the continental shelf, Timmermann et al. (2002 b) link the interannual variability of Western Shelf Water salinities and the location of the density maximum to that of sea ice fresh-water fluxes. Since the Ross Sea wind regime and consequently its sea ice distribution and the associated fresh-water fluxes are more steady than those of the Weddell Sea, no changes in circulation pattern occur but only a modulation of its transport.

The interannual variability of sea ice fresh-water fluxes in the western Ross Sea is predominantly determined by that of the local atmospheric conditions, particularly by the winds. However, the interannual variability of the local fresh-water fluxes cannot be identified in that of HSSW characteristics. Fast advection of surface waters at the maximum brine release around April results in blurring the interannual variability of peak sea ice growth, and leads to a strong attenuation of the seasonal signal towards greater depth. The signal that predominantly controls the interannual variability of HSSW characteristics is carried onto the shelf by the inflowing waters. Signals in salinity and potential temperature are hereby found to enter at different depth. The salinity signal is located within subsurface waters around 150-m depth, while the potential temperature signal is found around 400-m depth within the core of the coastal current.

The cooling and salt input due to sea ice formation and subsequent deep convection during the seasonal cycle modifies the waters of the shelf inflow so that they reach a density that enables them to participate in Antarctic Bottom Wa-

ter formation. However, the interannual variability of shelf water characteristics is strongly determined by the variability of the shelf inflow induced upstream. Brine input increases the salinity of the relatively fresh sub-surface inflow, which carries the signal of salinity variability found in the HSSW, and leads to the signal's transmission to lower depth. There it interacts with deep water upwelled onto the continental shelf as the second source of HSSW. With a more constant and higher salinity this deep water carries the signal of temperature variability. The hypothesis of Toggweiler & Samuels (1995) hence seems to be applicable to the Ross Sea continental shelf, although this work has identified the inflowing sub-surface waters and their interannual variability as a second significant source for HSSW and its variability. In contrast, a more varying wind and sea ice regime in the Weddell Sea results in a stronger sea ice influence on the interannual variability of shelf water salinities due to associated changes in circulation regime (Timmermann et al. 2002b).

The origin of the inflow characteristics to the Ross Sea continental shelf can be traced into the Amundsen and Bellingshausen Seas. The potential temperature anomalies between 300 and 800 m depth are induced in the western Bellingshausen Sea where Circumpolar Deep Water (CDW) is carried south with the eastern end of the Ross Gyre extension. The transport strength is positively correlated to the potential temperature anomalies at the continental shelf break where warm CDW and cold shelf waters interact. This mechanism is the origin of the bottom-intensified potential temperature anomaly within the coastal current that was described as the Antarctic Circumpolar Coastal Wave (ACCW) by Beckmann & Timmermann (2001). As well as travelling westward towards the Ross Sea, part of the signal is also advected eastward towards Drake Passage.

Upwelling of water carrying the westward travelling potential temperature signal in the centre of the Ross Gyre extension causes anomalies of vertical heat flux and thus of the sea ice related fresh-water flux near the sea ice edge in the Amundsen Sea. These result in a sub-surface salinity anomaly that is advected onto the Ross Sea continental shelf and strongly affects Ross Sea HSSW salinities. The link of the potential temperature and salinity anomalies through upward oceanic heat flux provides an explanation for the strong link between the two signals despite their propagation at different depth. Meridional heat transport in the Amundsen and Bellingshausen Seas thus affects the interannual variability of Ross Sea High Salinity Shelf Water characteristics.

The potential temperature anomalies of the ACCW travel westward towards the

Weddell Sea (Beckmann & Timmermann 2001). Model results show that they are joined by salinity anomalies as they leave the Ross Sea. Signals of interannual variability induced in the Pacific sector thus appear to have an influence on the Weddell Sea in agreement with a study by Martinson & Iannuzzi (2003). The opposite, however, does not appear to be true. The eastward travelling component of the ACCW appears to block signals that propagate westward around the Antarctic Peninsula, but probably does not affect the Weddell Sea, as it is carried northeast with the ACC. Further model studies of this issue would require a more detailed representation of the passages between the Antarctic Peninsula and the offshore islands.

Naturally, this study still leaves a couple of questions unanswered:

The major contribution of the Southern Ocean to the global ocean circulation is the ventilation of deep and bottom waters. A conundrum has always been why the contribution of the Ross Sea appears to be much smaller than that of the Weddell Sea, even though its shelf waters are considerably denser than those of the Weddell Sea. Processes at the continental shelf break governing the downslope flow of dense shelf waters are not well understood. Recent observations at the Ross Sea continental slope show that small-scale high velocity plumes may contribute a large proportion of the volume of downslope transport and highlight the importance of tidal mixing and its modulation by spring and neap tides at the shelf break (AnSlope 1, 2003, A.L. Gordon & L. Padman, personal communication). In a model study, Beckmann & Pereira (2003) link the occurence of downslope flows to tidally induced mixing at the shelf break with the implication of strong mixing due to diurnal tides in the Ross Sea preventing shelf waters from reaching the abyss. BRIOS2.2 includes neither the effect of tides nor does it permit the formation of non-hydrostatic plumes, and hence is not the right tool to investigate downslope flows and their variability. Further studies will be necessary to shed light on the fundamental mechanisms governing Antarctic downslope flows.

Previous research has shown the Amundsen and Bellingshausen Seas to be the main entry for lower latitude variability to the Southern Ocean system. Ice shelves in the Amundsen and Bellingshausen Seas drain a large proportion of the West Antarctic Ice Sheet whose grounding line below sea level makes it particularly vulnerable to oceanic changes. Also, the driving mechanism of the variability in the southward heat transport associated with the CDW intrusion in the Amundsen and Bellingshausen Seas is still unclear. This study has shown, however,

that oceanic changes in this region strongly affect dense water formation on the Ross Sea continental shelf, and therefore likely the ventilation of the deep Pacific Ocean. Observations of the circulation in the Amundsen and Bellingshausen Seas remain sparse, but in view of the growing evidence of the importance of this region, the data base should be extented despite the logistical difficulties.

Acknowledgements

This thesis was written at Alfred-Wegener-Institute for Polar and Marine Research, Bremerhaven (AWI) under the supervision and with the support of Prof. D. Olbers who I would like to thank for giving me the opportunity to complete the work presented in this thesis and to take part in various conferences and the Nathaniel B. Palmer cruise. I would also like to thank Prof. P. Lemke for his willingness to mark this thesis.

Many people contributed to the successful completion of this work. The NCEP atmospheric forcing fields were received via the NOAA-CIRES Climate Diagnostics Centre, Boulder, Colorado (http://www.cdc.noaa.gov/). Tina Tin and Martin Jeffries provided sea ice thickness data, Lutz Sellmann the pre-processing of the buoy data, and Phil Mele the RVIB *N.B. Palmer* winds. Kyle Dedrick helped with the NIC iceberg data. Christoph Lichey provided the interpolation programme of NCEP reanalyses onto the BRIOS grid and Christian Schmaltz and Matthias Hullin the sea ice drift buoy programme. Wolfgang Cohrs, Chresten Wübber, and Herbert Liegmahl took good care of the computers used, and hence contributed vitally to the completion of this thesis. Thanks go to all of these. Thanks also go to my colleagues at AWI, especially those of the BRIOS and sea ice goups, for the good working atmosphere and their constant helpfulness.

Special thanks go to Hartmut H. Hellmer and Aike Beckmann who were my day-to-day supervisors. Hartmut supported me with his boundless enthusiasm for Antarctic research, establishing the contact to Lamont-Doherty-Earth Observatory of Columbia University and his useful and critical feedback to early versions of this thesis lead to a significant improvement. Aike Beckmann was always willing to discuss scientific and model questions within a productive critical dialogue.

Stanley S. Jacobs of Lamont-Doherty-Earth Observatory of Columbia University I would like to thank for the cooperation on the Amundsen sea ice work, for improving the manuscript with copious amounts of green ink and for being a constant source of scientific inspiration and constructive criticism. Further I would like to thank Prof. A.L. Gordon of Lamont-Doherty-Earth Observatory for giving me the opportunity to join a Nathaniel B. Palmer cruise to the Ross Sea as part of the AnSlope project, and Bruce Huber for teaching me the basics of observational physical oceanography as my watch leader on this cruise.

Finally, I would like to thank Ralph Timmermann. For use of the coupled sea ice-ocean model code developped by him and for spending countless hours with me patiently solving model problems. For being an inspirational, enthusiastic and critical research partner, who by reading early versions of this thesis helped me to improve it greatly. And for being a great friend.

Appendix A

Horizontal Grid Structure

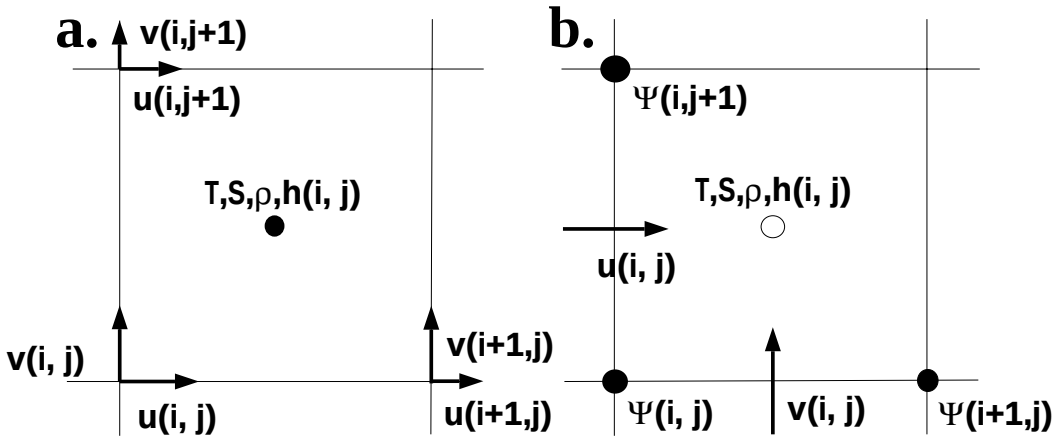

Figure A.1: Arrangement of variables on staggered horizontal grids: **a.** Sea ice grid - Arakawa B-grid. **b.** Ocean grid - Arakawa C-grid (Arakawa & Lamb 1977).

Shown above are the numerical grid types used in this study. The Arakawa B-grid is used for the sea ice model. Here, both velocity components and all scalar variables lie on one point each. The ocean model is discretized on an Arakawa C-grid. While the scalar grid points are still located in the centre of the grid box, the velocity components have been shifted by half a grid box width. Grid points for the transport stream function Ψ are placed on the grid box corners. In the vertical, a similar scheme is used to stagger the grid points. Scalar grid points are located halfway between vector ones and thus always in the middle of the gridbox.

The advantages of the C-grid structure are that no interpolation is necessary for the computation of advection, that there is less damping of waves, and that

narrower passages can be resolved. Its disadvantage is that interpolation becomes necessary for terms where the value of all velocity components is needed at one point, e.g. the tensor of deformation rates used in the sea ice rheology and for plotting.

Appendix B

Validation of NCEP winds for the Amundsen Sea

For validation of the NCEP data the winds for February and March 2000 were compared to wind data obtained throughout RVIB Nathaniel B. Palmer cruise NBP00-01, the cruise during which the sea ice drift buoys analysed in section 5.1 were deployed in the Amundsen and Bellingshausen Seas. To best make the two sets of data comparable to each other the mean wind speed and direction at the mean ship's position of each day and their standard deviations were calculated yielding mean values for 27 days between 20/02/2000 and 23/03/2000. These were then compared to the NCEP wind data at the model grid point closest to the mean position on the corresponding days. The mean distance between the ship position and the model grid point is 8.4 km which makes them reasonably comparable considering that the model resolution is about 50 km in this region and the ship movement was also more than 8 km per day.

60 % of the observed and NCEP wind directions and magnitudes agree within one standard deviation. Up to day 75, while the cruise track followed the Amundsen Sea coast eastward, the NCEP data reproduces the wind direction well, but quite consistently underestimates the wind speed (Fig. B.1), a deficiency of the NCEP data already mentioned by Smith et al. (2001). In Pine Island Bay, between days 75 and 83, the wind speeds are reproduced faithfully while the wind directions now diverge considerably from those measured on board. This might be due to smaller scale phenomena gaining importance, since there was less ship movement in this area and thus less spatial averaging of variations. Considering the very different nature of the data sets and the short period of comparison it can be

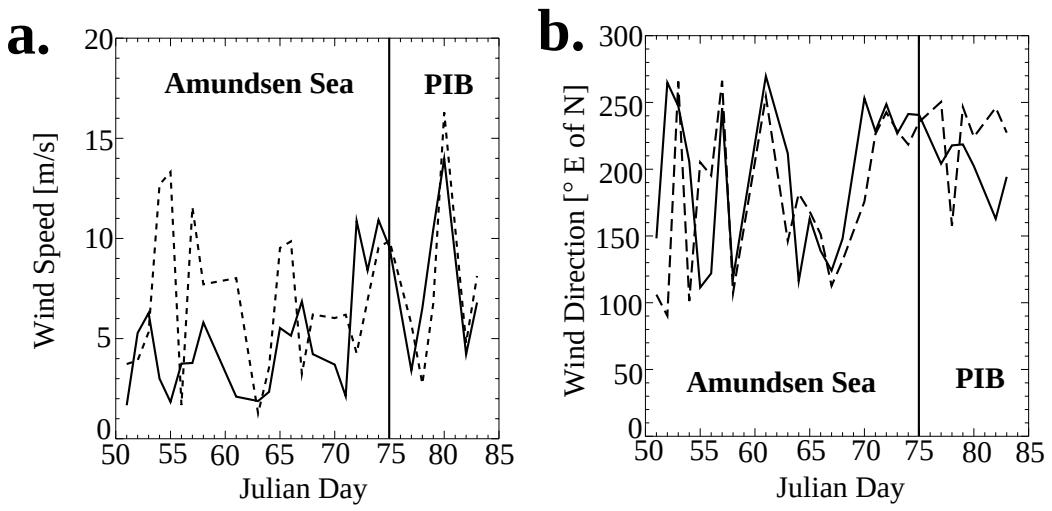

Figure B.1: Comparison of magnitude (**a**) and direction (**b**) of NCEP winds (solid lines) with observed winds on cruise NBP00-01 (dashed lines). Data considered lies between 75°S, 150°W (20/2/2000) and 71°S, 104°W (23/3/2000). PIB = Pine Island Bay.

concluded that the NCEP data appear to provide a reasonable representation of wind conditions in the Amundsen Sea. Even though this analysis only represents a random sample rather than conclusive evidence for the quality of the NCEP data, it gives some confidence that the winds at least are close to the real ones, always with the restriction of resolution and keeping in mind that wind speeds are under- rather than overestimated.

Bibliography

Adams, J.: MUDPACK: Multigrid Fortran software for the efficient solution of linear elliptic partial differential equations. *Appl. Math. Comput.*, **34**, 113-146, 1989.

Arakawa, A., and V.R. Lamb: Computational design of the basic dynamical processes of the UCLA general circulation model. *Methods of Computational Physics*, **17**, 174-265, Academic Press, 1977.

Assmann, K., H.H. Hellmer, and A. Beckmann: Seasonal variation in circulation and watermass distribution on the Ross Sea continental shelf. *Ant. Sci.*, **15(1)**, 3-11, DOI:10.1017/S0954102003001007, 2003.

Baines, P.G., and S. Condie: Observations and modelling of Antarctic downslope flows: A review. *Antarct. Res. Ser.*, **75**, 29-49, 1998.

Bamber, J., and C.R. Bentley: A comparison of satellite-altimetry and ice-thickness measurements of the Ross Ice Shelf, Antarctica. *J. Glaciol.*, **20**, 357-364, 1994.

Barry, J.P., and P.K. Dayton: Current patterns in McMurdo Sound, Antarctica and their relationship to local biotic communities. *Polar Biology*, **8**, 367-376, 1988.

Beckmann, A., and D.B. Haidvogel: A numerical simulation of flow at Fieberling Guyot. *J. Geophys. Res.*, **102(C3)**, 5595-5613, 1997.

Beckmann, A., H.H. Hellmer, and R. Timmermann: A numerical model of the Weddell Sea: large scale circulation and water mass distribution. *J. Geophys. Res.*, **104(C10)**, 23375-23391, 1999.

Beckmann, A., and R. Timmermann: Circumpolar influences on the Weddell Sea: Indication of an Antarctic Circumpolar Coastal Wave, *Journal of Climate*, **14**, 3785-3792, 2001.

Beckmann, A., and A.F. Pereira: Lateral tidal mixing in the Antarctic marginal seas. *Ocean Dynamics*, **53**, 21-26, 2003.

Bergamasco, A., S. Carniel, and L. Caldesi Valeri: Reconstructing the

general circulation of the Ross Sea (Antarctica) using a robust diagnostic model. In: *Oceanography of the Ross Sea.* Eds. G. Spezie and G.M.R. Manzella. Milano, Springer-Verlag, 119-134, 1999.

Botnikov,V.N., and I.V. Chuguy: The major features of water circulation and spatial distribution of the Ross Gyral, *Polar Geography and Geology*, **13(3)**, 212-224, 1989.

Broecker, W.S.: The great ocean conveyor. *Oceanography*, **4**, 79-89.

Cai, W., and P.G. Baines: Forcing of the Antarctic Circumpolar Wave by El Niño-Southern Oscillation teleconnections. *J. Geophys. Res.*, **106**, 9019-9039, 2001.

Carmack, E.C.: Water characteristics of the Southern Ocean south of the Polar Front. In: *A voyage of Discovery*, Pergamon, London, 15-41.

Cavalieri, D.J., C.L. Parkinson, P. Gloersen, and H.J. Zwally: Sea ice concentrations from Nimbus-7 SMMR and DMSP SSM/I Passive Microwave Data, Technical Report, National Snow and Ice Center, Boulder, CO, 1999, updated 2002.

Comiso, J.C., D.J. Cavalieri, C.L. Parkinson, and P. Gloersen: Passive microwave algorithms for sea ice concentration: A comparison of two techniques. *Remote Sens. Environ.*, **60(3)**, 357-384, 1997.

Comiso, J.C., and A.L. Gordon: Interannual variability in summer sea ice minimum, coastal polynyas and bottom water formation in the Weddell Sea. *Antarct. Res. Ser.*, **74**, 293-315, 1998.

Comiso, J.: Bootstrap sea ice concentrations for NIMBUS-7 SMMR and DMSP SSM/I. Boulder, CO, USA: National Snow and Ice Data Center, Digital media, 1999, updated 2002. [Available online at http://nsidc.org/data/nsidc-0079.html.]

Commodari, V., and S. Pierini: A wind and boundary driven circulation model of the Ross Sea. In: *Oceanography of the Ross Sea.* Eds. G. Spezie and G.M.R. Manzella. Milano, Springer-Verlag, 135-144, 1999.

Connolley, W.M.: Long-term variation of the Antarctic Circumpolar Wave. *J. Geophys. Res.*, **108(C4)**, DOI:10.1029/2000JC000380, 2003.

Deacon, G.E.R.: The Weddell Gyre. *Deep Sea Research*, **26 A**, 981-995, 1979.

Dinniman, M.S., J.M. Klinck, and W.O. Smith: Cross shelf exchange in a model of the Ross Sea circulation and biogeochemistry. *Deep Sea Research*, 2003. [in press]

Drinkwater, M.R., X. Liu, J. Maslanik, and C. Fowler: Optimal analysis

products combining buoy trajectories and satellite-derived ice-drift field. In *IPAB Biennial Meeting Report, May 11-13, 1998, Naples, Italy, WCRP Rep. 5/1999*, World Climate Research Program, Geneva, 1-11, 1999.

Eicken, H., M. Lange, H.W. Hubberten, and P. Wadhams: Characteristics and distribution patterns of snow and meteoric ice in the Weddell Sea and their contribution to the mass balance of sea ice. *Annales Geophysicae*, **12**, 80-93, 1994.

Eicken, H.: From the Microscopic, to the Macroscopic, to the Regional Scale: Growth, Microstructure and Properties of Sea Ice. In: *Sea Ice - An Introduction to its Physics, Chemistry, biology and Geology* Eds. D.N. Thomas and G.S. Dieckmann, Blackwell Publishing, 22-81, 2003.

Emery, W. J., and J. Meincke: Global water masses: summary and review. *Oceanol. Acta*, **9(4)**, 383-391, 1986.

Fichefet, T., and H. Goosse: A numerical investigation of the spring Ross Sea polynya. *Geophys. Res. Lett.*, **26(8)**, 1015-1018, 1999.

Fischer, H.: Vergleichende Untersuchungen eines optimierten dynamisch - thermodynamischen Meereismodells mit Beobachtungen im Weddellmeer [Comparison of an optimized dynamic - thermodynamic sea ice model with observations in the Weddell Sea.]. *Berichte zur Polarforschung*, **166**, Alfred-Wegener-Institute, Bremerhaven, 130 pp, 1995.

Foldvik, A., T. Gammelsrød, and T. Tørresen: Circulation and watermasses on the southern Weddell Sea shelf. *Antarct. Res. Ser.*, **43**, 5-20, 1985.

Foster, T.D., and E.C. Carmack: Frontal zone mixing and Antarctic Bottom Water formation in the southern Weddell Sea. *Deep Sea Research*, **23(4)** 301-317, 1976.

Fox, A.J., and A.P.R. Cooper: Measured properties of the Antarctic ice sheet derived from the SCAR Antarctic digital database. *Polar Record*, **30(174)**, 201-2016, 1994.

Gloersen, P., W.J. Campbell, D.J. Cavalieri, J.C. Comiso, C.L. Parkinson, and H.J. Zwally: Arctic and Antarctic sea ice : Satellite passive-microwave observations and analysis. National Aeronautics and Space Administration (NASA), Washington, DC, 290 pp, 1992.

Goosse, H., and T. Fichefet: Importance of ice-ocean interactions for the global ocean circulation: A model study. *J. Geophys. Res.*, **104(C10)**, 23337-23355, 1999.

Gordon, A.L.: Interocean exchange of thermocline waters. *J. Geophys. Res.*, **91**, 5037-5046, 1986.

Gouretski, V., K. Jancke, J. Reid, J. Swift, P. Rhines, R. Schlitzer, and I. Yashayaev: *WOCE Hydrographic Programme Special Analysis Centre*, Atlas of Ocean Sections CD-ROM, 1999. [Available at http://www.dkrz.de/~u241046/SACserver/SACHome.htm.]

Gouretski, V.V.: The large-scale thermohaline structure of the Ross Gyre. In: *Oceanography of the Ross Sea*. Eds. G.Spezie and G.M.R. Manzella. Milano: Springer-Verlag, 77-102, 1999.

Greischar, L.L., and C.R. Bentley: Isostatic Equilibrium grounding line between the West Antarctic inland ice sheet and the Ross Ice Shelf, *Nature*, **283**, 651-654, 1980.

Greischar, L.L., C.R. Bentley, and L.R. Whiting: An analysis of gravity measurements on the Ross Ice Shelf, Antarctica. *Ant. Res. Ser.*, **57**, 105-155, 1992.

Grosfeld, K., M. Schröder, E. Fahrbach, R. Gerdes, and A. Mackensen: How iceberg calving and grounding change the circulation and hydrography in the Filchner Ice Shelf-Ocean system, *J. Geophys. Res.*, **106(C5)**, 9039-9055, 2001.

Grotov, A.S., D.A. Nechaev, G.G. Panteleev, and M.I. Yaremchuk: Large scale circulation in the Bellingshausen and Amundsen Seas as a variational inverse of climatological data. *J. Geophys. Res.*, **103**, 13,011-13,022, 1998.

Gurney, A.: *Below the convergence: voyages toward Antarctica 1699-1839*. W. W. Norton & Company, New York, 315 pp., 1997.

Häkkinen, S.: Seasonal simulation of the Southern Ocean coupled ice-ocean system. *J. Geophys. Res.*, **100(C11)**, 22733-22748, 1995.

Haidvogel, D.B., J.L. Wilkin, and R.E. Young: A semi-spectral primitive equation ocean circulation model using vertical sigma and orthogonal curvilinear horizontal coordinates. *J. Comput. Phys.*, **94**, 151-185, 1991.

Haidvogel, D.B., and A. Beckmann: *Numerical Ocean Circulation Modelling*, Imperial College Press. 344 pp, 1999.

Harms, S., E. Fahrbach, and V.H. Strass: Sea ice transports in the Weddell Sea. *J. Geophys. Res.*, **106(C5)**, 9057-9073, 2001.

Harder, M.: Erweiterung eines dynamisch-thermodynamischen Meereismodells zur Erfassung deformierten Eises. *Berichte aus dem Fachbereich Physik*, **50**,

Alfred-Wegener-Institut (AWI), Bremerhaven, 1996.

Harder, M., and Fischer, H.: Sea ice dynamics in the Weddell Sea simulated with an optimized model. *J. Geophys. Res.*, **104(C5)**, 11,151-11,162, 1999.

Heap, J.A.: Pack ice *Antarctic Research.* edited by R. Priestley, R. Adie, and G. Robin, Butterworths, 308-317, 1964.

Hedström, K.: User's manual for a semi-primitive equation ocean circulation model. Institute of Marine and Coastal Sciences, Rutgers University, 131pp., 1994.

Hellmer, H.H., and D. Olbers: A two-dimensional model for the circulation under an ice shelf. *Ant. Sci.*, **1**, 325-336, 1989.

Hellmer, H.H., and S.S. Jacobs: Seasonal circulation under the eastern Ross Ice Shelf, Antarctica. *J. Geophys. Res.*, **100(C6)**, 10873-10885, 1995.

Hellmer, H.H., S.S. Jacobs, and A. Jenkins: Oceanic erosion of a floating Antarctic glacier in the Amundsen Sea. *Antarct. Res. Ser.*, **75**, 83-99, 1998.

Hibler, W.D., III: A dynamic-thermodynamic sea ice model. *J. Phys. Oceanogr.*, **9(4)**, 815-846, 1979.

Hibler, W.D., III: The role of sea ice dynamics in modelling CO_2 increases. In: *Climate processes and climate sensitivity*, Geophysical Monograph, **29**, Ed. J.E.Hansen and T.Takahashi, 238-253, AGU, Washington, D.C., 1984.

Høeg, P.: Miss Smilla's feeling for snow. The Harvill Press. London. 410 pp. 1996.

Hohmann, R., P. Schlosser, S. Jacobs, A. Ludin, and R. Weppernig: Excess Helium and Neon in the southeast Pacific: Tracers for glacial meltwater, *J. Geophys. Res.*, **104(C11)**, DOI:10.1029/2000JC000378, 2002.

Holland, D.M., S.S. Jacobs, and A. Jenkins: Modeling the ocean circulation beneath the Ross Ice Shelf. *Ant. Sci.*, **15(1)**, 13 - 23, 2003.

Hunkins, K.: The oceanic boundary layer and stress beneath a drifting ice floe. *J. Geophys. Res.*, **80(24)**, 3425-3432, 1975.

Jackett, D.R., and T.J. McDougall: Stabilization of hydrographic data. *J. Atmos. Oceanic Technol.*, **12**, 381-389, 1995.

Jacobs, S.S., A.F. Amos, and P.M. Bruchhausen: Ross sea oceanography and Antarctic Bottom Water formation. *Deep-Sea Research*, **17**, 935-962, 1970.

Jacobs, S.S., A.L. Gordon, and J.L. Ardai jr.: Circulation and melting beneath the Ross Ice Shelf. *Science*, **203**, 439-443, 1979.

Jacobs, S.S., R.G. Fairbanks, and Y. Horibe: Origin and Evolution of

water masses near the Antarctic continental margin: Evidence from $H_2^{18}O$ /$H_2^{16}O$ ratios in seawater. *Antarct. Res. Ser.*, **43**, 59-95, 1985.

Jacobs, S.S., and J.C. Comiso: Sea ice and oceanic processes on the Ross Sea continental shelf. *J. Geophys. Res.*, **94**, 18,195-18,211, 1989.

Jacobs, S.S., H.H. Hellmer, C.S.M. Doake, A. Jenkins, and R.M. Frolich: Melting of ice shelves and the mass balance of Antarctica. *J. Glac.*, **38(130)**, 375-387, 1992.

Jacobs, S.S., H.H. Hellmer, and A. Jenkins: Antarctic ice sheet melting in the Southeast Pacific. *Geophys. Res. Lett.*, **23**, 957-960, 1996.

Jacobs, S.S., and J.C. Comiso: Climate variability in the Amundsen and Bellingshausen Sea. *J. Clim.*, **10**, 697-709, 1997.

Jacobs, S.S., and C.F. Giulivi: Interannual ocean and sea ice variability in the Ross Sea. *Antarct. Res. Ser.*, **75**, 135-150, 1998.

Jacobs, S.S., C.F. Giulivi, and P.A. Mele: Freshening of the Ross Sea during the late 20th century, *Science*, **297**, 386-389, 2002.

Jeffries, M.O., S. Li, R.A. Jana, H.R. Krause, and B. Hurst-Cushing: Late winter first-year ice floe variability, seawater flooding and snow ice formation in the Amundsen and Ross Seas. *Ant. Res. Ser.*, **74**, 69-88, 1998.

Johnson, M.R., and A.M. Smith: Seabed topography under the southern and western Ronne Ice Shelf, derived from seismic surveys, *Ant. Sci.*, **9**, 201-208, 1997.

Keys, H.J.R., S.S. Jacobs, and D. Barnett: The calving and drift of iceberg B-9 in the Ross Sea, Antarctica. *Ant. Sci.*, **2(3)**, 243-257, 1990.

Killworth, P.D.: A baroclinic model of motions on Antarctic continental shelves. *Deep-Sea Research*, **21**, 815-837, 1974.

King, J.C., and J. Turner: Antarctic meteorology. Cambridge University Press. 409pp. 1997.

König-Langlo, G., and E. Augstein: Parameterization of the downward longwave radiation at the Earth's surface in polar regions. *Meteorol. Zeitschrift*, **3(6)**, 343-347, 1994.

Kohnen, H.: Glaciological investigations in the frontal zone of the Filchner and Ronne Ice Shelves, *Ann. Glaciol.*, **3**, 160-165, 1982.

Kreyscher, M., M. Harder, P. Lemke, and G.M. Flato: Results of the Sea Ice Model Intercomparison Project: Evaluation of sea-ice rheology schemes for use in climate simulations. *J. Geophys. Res.*, **105(C5)**, 11299-11320, 2000.

Laevastu, T.: Factors affecting the temperature of the surface layer of the sea. *Comment. Phys. Math.*, **25**, 1, 1960.

Ledley, T.S., and Z. Huang: A possible ENSO signal in the Ross Sea. *Geophys. Res. Lett.*, **24**, 3253-3256, 1997.

Lemke, P., W.D. Hibler, G. Flato, M. Harder, and M. Kreyscher: On the improvement of sea-ice models for climate simulations: the Sea Ice Model Intercomparison Project. *Ann. Glaciol.*, **25**, 183-187, 1997.

Leppäranta, M.: A growth model for black ice, snow ice, and snow thickness in subantarctic basins. *Nordic Hydrology*, **14**, 59-70, 1983.

Lewis, E.L., and R.G. Perkin: Ice pumps and their rates. *J. Geophys. Res.*, **91(C10)**, 11756-11762, 1986.

Lewis, E.L., and R.G. Perkin: The winter oceanography of McMurdo Sound, Antarctica. *Antarct. Res. Ser.*, **43**, 145-165, 1985.

Locarnini, R.A.: Water masses and circulation in the Ross Gyre and environs. PhD Thesis, Texas A & M University, 87 pp., 1994.

Marshall, G.J.: Trends in Antarctic geopotential height and temperature: a comparison between radiosonde and NCEP-NCAR reanalysis data. *Journal of Climate*, **15 (6)**, 659-674, 2002.

Marshall, G.J., V. Lagun, and T.A. Lachlan-Cope: Changes in Antarctic Peninsula tropospheric temperatures from 1956 to 1999: A synthesis of observations and reanalysis data. *International Journal of Climatology*, **22(3)**, 291-310, 2002.

Marsland, S.J., and J.-O. Wolff: On the sensitivity of Southern Ocean sea ice to the surface fresh water flux: A model study. *J. Geophys. Res.*, **106(C2)**, 2723-2741, 2001.

Martinson, D.G., and C. Wamser: Ice drift and momentum exchange in winter Antarctic pack ice. *J. Geophys. Res.*, **95(C2)**, 1741-1755, 1990.

Martinson, D.G., and R.A. Iannuzzi: Spatial/temporal patterns in Weddell gyre characteristics and their relationship to global climate. *J. Geophys. Res.*, **109(C4)**, 10.1029/2000JC000538, 2003.

Maykut, G.A.: Estimates of the regional heat and mass balance of the ice cover. In: *A Symposium on Sea Ice Processes and Models*, **I**, 65-74, University of Washington, Seattle, 1977.

Morison, J.H., M.G. McPhee, and G.A. Maykut: Boundary layer, upper ocean and ice observations in the Greenland Sea marginal ice zone. *J. Geophys. Res.*, **92(C7)**, 6987-7011, 1987.

Olbers, D., and C. Wübber: The role of wind and buoyancy forcing of the Antarctic Circumpolar Current. In: *Strategies for Future Climate Research*, Ed. M. Latif, 161-192, Max-Planck-Institut für Meteorologie, Hamburg, 1991.

Orsi, A.H., T. Whitworth III, and W.D. Nowlin: On the meridional extent and fronts of the Antarctic Circumpolar Current. *Deep-Sea Res.*, **42**, 641-673, 1995.

Orsi, A.H., G.C. Johnson, and J.L. Bullister: Circulation, mixing, and production of Antarctic Bottom Water. *Prog. Oceanogr.*, **43**, 55-109, 1999.

Owens, W.B. and P. Lemke: Sensitivity studies with a sea ice-mixed layer-pycnocline model in the Weddell Sea. *J. Geophys. Res.*, **95(C6)**, 9527-9538, 1990.

Pacanowski, R.C.: MOM2 Version 2.0 - Documentation, user's guide and reference manual. *GFDL Ocean Technical Report* **3.2**, 1996.

Pacanowski, R.C., and S.G.H. Philander: Parameterization of vertical mixing in numerical models of tropical oceans. *J. Phys. Oceanogr.*, **11**, 1443-1451, 1981.

Padman, L., and C. Kottmeier: High-frequency ice motion and divergence in the Weddell Sea. *J. Geophys. Res.*, **105**, 3379-3400, 2000.

Padman, L., S. Erofeeva, and I. Joughin: Tides of the Ross Sea and Ross Ice Shelf cavity. *Ant. Sci.*, **15(1)**, 31 - 40, 2003.

Parkinson, C.L., and W.M. Washington: A large-scale numerical model of sea ice. *J. Geophys. Res.*, **84(C1)**, 311-337, 1979.

Parkinson, C.L.: Trends in the length of the Southern Ocean sea-ice season, 1979-99. *Annals of Glaciology*, **34**, 435-440, 2002.

Pereira, A.F., A. Beckmann, and H.H. Hellmer: Tidal mixing in the southern Weddell Sea: results from a three-dimensional model, *J. Phys. Oceanogr.*, **32(7)**, 2151-2170, 2002.

Picco, P., L. Amici, R. Meloni, L. Langone, and M. Ravaioli: Temporal variability of currents in the Ross Sea (Antarctica). In: *Oceanography of the Ross Sea.*. Eds. G. Spezie and G.M.R. Manzella, Milano: Springer-Verlag, 103-118, 1999.

Pillsbury, R.D., and S.S. Jacobs: Preliminary observations from long-term current meter moorings near the Ross Ice Shelf, Antarctica. *Antarct. Res. Ser.*, **43**, 87-107, 1985.

Reid, J.L.: On the total geostrophic circulation of the South Pacific ocean:

Flow patterns, tracers and transports, *Progress in Oceanography*, **16**, 1-61, 1986.

Rignot, E.: Fast recession of a West Antarctic glacier *Science*, **281**, 549-551, 1998.

Rintoul, S.R.: On the origin and influence of Adélie Land Bottom Water. *Antarct. Res. Ser.*, **75**, 151-171, 1998.

Rintoul, S.R., C. Hughes, and D. Olbers: The Antarctic Circumpolar Current system. In: *Ocean ciculation and climate: observing and modeling the global ocean.* Eds. G. Siedler, J. Church, and J. Gould. *International Geophysics Series*, **77**, Academic Press, New York, 271-302.

Robertson, R., M. Visbeck, A.L. Gordon, and E. Fahrbach: Long-term temperature trends in the deep waters of the Weddell Sea, *Deep Sea Research II*, **49(21)**, 4791-4806, 2002.

Rock, S.R.: Circulation and heat transport across the Ross Ice Shelf edge, Antarctica. Master's Thesis, Lamont Doherty Earth Observatory of Columbia University, 37 pp, 1995. [Unpublished]

Ross, J.C.: *A voyage of discovery and research in the southern and antarctic regions during the years 1839-43.* Murray, London, 1847.

Schott, F., and K.D. Leaman: Observations with moored acoustic Doppler current profilers in the convectin regime in the Gulf of Lions. *J. Phys. Oceanogr.*, **21**, 556-572, 1991.

Schröder, M., H.H. Hellmer, and J.M. Absy: On the near-bottom variability in the northwestern Weddell Sea. *Deep Sea Research*, **49**, 4767-4790, 2002.

Semtner, A.J., Jr.: A model for the thermodynamic growth of sea ice in numerical investigations of climate. *J. Phys. Oceanogr.*, **6(3)**, 379-389, 1976.

Send, U., and R.H. Käse : Parameterization of processes in deep convection regimes. In: *Ocean Modeling and Parameterizations*, Ed. E.P.Chassignet and J.Verron, NATO Science Series, **516**, 191-214, 1998.

Smith, S.R., D.M. Legler, and K.V. Verzone: Quantifying uncertainties in NCEP Reanalyses using high-quality research vessel data, *J. Clim.*, **14(20)**, 4062-4072, 2001.

Smith, W.H.F., and D.T. Sandwell: Global Sea Floor Topography from Satellite Altimetry and Ship Depth Soundings. *Science*, **277**, 1956-1962, 1997.

Smolarkiewicz, P.K.: A simple positive definite advection scheme with small implicit diffusion. *Monthly Weather Review*, **111**, 479-486, 1983.

Timmermann, R.: Wechselwirkungen zwischen Eis und Ozean im Weddellmeer - Studien mit einem gekoppelten Eis - Ozean - Modell des Südpolarmeeres, Dissertation, elektronische Publikation http://elib.suub.uni-bremen.de/dissertations/physic/Timmermann_R2000/, Universität Bremen, 130pp, 2000.

Timmermann, R., A. Beckmann, and H.H. Hellmer: The role of sea ice in the fresh water budget of the Weddell Sea, *Annals of Glaciology*, **33**, 419-424, 2001.

Timmermann, R., A. Beckmann, and H.H. Hellmer: Simulation of ice-ocean dynamics in the Weddell Sea. Part I: Model configuration and validation. *J. Geophys. Res.*, **107(C3)**, 10.1029/2000JC000471, 2002 a.

Timmermann, R., H.H. Hellmer, and A. Beckmann: Simulation of ice-ocean dynamics in the Weddell Sea. Part II: Interannual variability 1985-1993. *J. Geophys. Res.*, **107(C3)**, 10.1029/2000JC000472, 2002 b.

Tin, T., R. Timmermann, and M.O. Jeffries: On the evolution of sea ice thickness in the Ross Sea 1998/1999, *J. Glaciology*, 2003, submitted.

Toggweiler, J.R., and B. Samuels: Effect of sea ice on the salinity of Antarctic Bottom Waters. J. Phys. Oceanogr., **25**, 1980-1997, 1995.

Tressler, W.L., and A.M. Ommundsen: Seasonal oceanographic studies in McMurdo Sound, Antarctica. Tech. Rep. 125, 125 pp, U. S. Navy Hydrographic Office, Washington DC, 1962.

Trumbore, S.E., S.S. Jacobs, and W.M. Smethie Jr.: Chlorofluorocarbon evidence for rapid ventilation of the Ross Sea, *Deep Sea Research*, **38(7)**, 845-870, 1991.

UNESCO: Eighth report of the joint panel on oceanographic tables and standards. *UNESCO Technical Papers in Marine Science*, **28**, UNESCO, Paris, 1978.

UNESCO: Tenth report of the joint panel on oceanographic tables and standards. *UNESCO Technical Papers in Marine Science*, **36**, UNESCO, Paris, 1981.

Van Loon, H.: The half-yearly oscillations in middle and high southern latitudes and the coreless winter. *J. Atmos. Sci.*, **24**, 472-486, 1967.

Vaughan, D.G., and C.S.M. Doake: Recent atmospheric warming and retreat of ice shelves on the Antarctic Peninsula. *Nature*, **379(6563)**, 328-331, 1996

Venegas, S.A., M.R. Drinkwater, and G. Shaffer: Coupled oscillations in Antarctic sea ice and atmosphere in the South Pacific sector, *Geophys. Res. Lett.*, **28(17)**, 3301-3304, 2001.

Venegas, S.A.: The Antarctic Circumpolar Wave: A combination of two signals ? *J. Clim.*, **16**, 2509-2525, 2003.

White, W.B., and R.G. Peterson: An Antarctic circumpolar wave in surface pressure, wind, temperature and sea ice extent. *Nature*, **380**, 699-702, 1996.

Whitworth, III, T., and R.G. Peterson: The volume transport of the Antarctic Circumpolar Current from three-year bottom pressure measurements. *J. Phys. Oceanogr.*, **15**, 810,816, 1985.

Whitworth III, T., A.H. Orsi, S.-J. Kim, W.D. Nowlin Jr., and R.A. Locarnini: Water masses and mixing near the Antarctic slope front. *Antarct. Res. Ser.*, **75**, 1-27, 1998.

Wilkin, J.L., J.V. Mansbridge, and K.S. Hedström: An application of the capacitance matrix method to accomodate masked land areas and island circulations in a primitive equation ocean model. *International Journal for Numerical Methods in Fluids*, **20**, 649-662, 1995.

Worby, A.P., M.O. Jeffries, W.F. Weeks, K. Morris, and R. Jana: The thickness distribution of sea ice and snow cover during late winter in the Bellingshausen and Amundsen Seas, Antarctica. *J. Geophys. Res.*, **101(C12)**, 28,441-28,455, 1996.

Worby, A.P. and I. Allison: A technique for making ship-based observations of Antarctic sea ice thickness and characteristics, Part 1: Observational Technique and Results. ASPeCt Report, **14**, Antarctic CRC, Hobart, 1999.

Yuan, X., and D.G. Martinson: Antarctic sea ice extent and its global connectivity, *J. Clim.*, **13**, 1697-1717, 2000.

Zillman, J.W.: A study of some aspects of the radiation and heat budgets of the southern hemisphere oceans. In: *Meteorological Study*, **26**, Bureau of Meteorology, Dept. of the Interior, Canberra, Australia, 526pp., 1972.

Zotikov, I.A., V.S. Zagorodnov, and J.V. Raikovsky: Core drilling through the Ross Ice Shelf (Antarctica) confirmed basal freezing. *Science*, **207**, 1463-1465, 1980.

Zotikov, I.A., and S.S. Jacobs: Oceanic inclusions in the J-9 sea-ice core. *Antarctic Journal of the US* , bf 20(5), 113-115, 1985.

Zwally, H.J., J.C. Comiso, and A.L. Gordon: Antarctic offshore leads and polynyas and oceanographic effects. *Antarct. Res. Ser.*, **43**, 203-226, 1985.

Zwally, H.J., J.C. Comiso, C.L. Parkinson, D.J. Cavalieri, and P. Gloersen: Variability of Antarctic sea ice 1979-1998, *J. Geophys. Res.*, **107(C5)**, DOI 10.1029/2000JC000733, 2002.